Winter 2010

Continental outflow of polluted air from the US to the North Atlantic and mercury chemical cycling in various atmospheric environments

Su Youn Kim
University of New Hampshire, Durham

CONTINENTAL OUTFLOW OF POLLUTED AIR FROM THE U.S. TO THE NORTH

ATLANTIC AND MERCURY CHEMICAL CYCLING IN VARIOUS

ATMOSPHERIC ENVIRONMENTS

BY

SU YOUN KIM

BS, Yonsei University, 2001

MS, Yonsei University, 2003

DISSERTATION

Submitted to the University of New Hampshire

In Partial Fulfillment of

The Requirements for the Degree of

Doctor of Philosophy

in

Earth and Environmental Science

December, 2010

UMI Number: 3442542
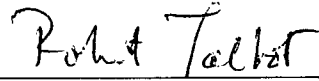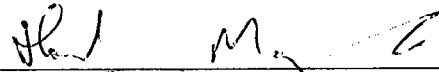
This dissertation has been examined and approved.

Robert Talbot

Dissertation Director, Robert W. Talbot, Research
Professor of Earth, Ocean, and, Space

Huiting Mao, Research Associate Professor of
Earth, Ocean, and Space

Howard R. Mayne, Professor of Chemistry

Barkley C. Sive, Research Associate Professor of
Earth, Ocean, and Space

Jennifer Hegarty, Research Scientist III of Earth,
Ocean, and Space

9-3-10

Date

ACKNOWLEDGEMENTS

TABLE OF CONTENTS

PREFACE

This dissertation consists of two parts which are focused on U.S. continental outflow and mercury chemical cycling in various environments. Continental outflow from the U.S. to the North Atlantic was investigated using a case study of NASA DC-8 flight 13 during the Intercontinental Chemical Transport Experiment – North America (INTEX-NA). The chemical transformations of gaseous elemental mercury (Hg°) to reactive gaseous mercury (RGM) and particulate mercury (PHg) were studied by simulations with a mercury chemical box model based on the data analysis of NASA DC-8 flights during the Arctic Research of the Composition of the Troposphere from Aircraft and Satellites (ARCTAS) field campaign. Secondly, the chmical cycling of mercury and the influence of 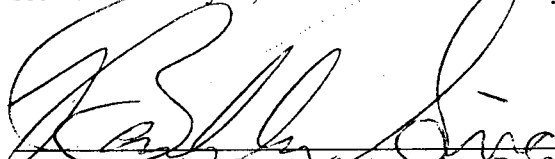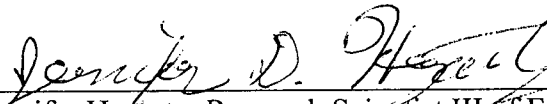water vapor on it were studied utilizing year-round measurements of atmospheric mercury in New England by the UNH-NOAA AIRMAP program.

Although not obvious, these two topics are related to each other. Hg° can be transported in the global and regional atmospheres due to its long life time, 6-24 months (Schroeder and Munthe, 1998). Thus, chemical transformations of mercury should be studied with consideration of its atmospheric transport regime. It is well known that transport of chemical species is an important factor to consider in estimating regional chemical budgets. Chemical transformation between Hg° and RGM is important for the atmospheric budget of mercury because RGM is readily removed from the atmosphere. Furthermore, links between mercury chemistry and other chemical transformations can give insight into atmospheric chemical processing.

The specific research topics were as follows. The first work was data analysis of chemical species measured over the North Atlantic during INTEX-NA to quantify the

effects of continental outflow to the atmosphere over the North Atlantic. This study found two interesting results. First, pollutants in the southeastern U.S. boundary layer were transported to the upper troposphere over the North Atlantic by vertical transport, which was facilitated by convection and warm conveyor belt (WCB) uplifting combined with fast southwesterly flow in the free troposphere. Secondly, the data suggest that the total tropospheric column over the North Atlantic was impacted by U.S. outflow in various stages of photochemical aging. This study was published in *Atmospheric Chemistry and Physics* in April, 2008.

The second facet of the work was studying chemical transformation of Hg° to RGM and PHg using a chemical box model based on the importance of RGM and PHg in the atmospheric budget of total gaseous mercury (TGM). The first part of the mercury study was the chemical transformation of Hg° in the Arctic springtime with box modeling based on data obtained by NASA DC-8 flights during the ARCTAS field campaign. A comprehensive gaseous chemical box model was developed including mercury, halogen, and ozone chemistries. The study indicated that high solar radiation, continuous high Br_2 emission, and a high NO_x regime accelerated Hg° depletion in the Arctic springtime. This study was published in *Atmospheric Chemistry and Physics Discussion* in April, 2010.

The second portion of the mercury study was the diurnal cycle of mercury at Thompson Farm, one of the UNH-NOAA AIRMAP measurement sites. The mass transport between gas-aqueous phases and aqueous reactions were added into the chemical box model. The box model simulations indicated that the loss amount of Hg° at nighttime could be influenced greatly by aerosol uptake with water solubility of Hg° and

the presence of higher liquid water content of aerosols compared to the loss amount of $Hg°$ by dry deposition. Moreover, sensitivity experiments suggested that the ambient level of PHg is controlled by dry deposition. This work is planned to be submited to *Geophysical Research Letters* in the near future.

Principal Objectives of my work were:

- Assess long-range transport of U.S. pollutant outflow to the Atlantic Ocean utilizing a large suite of trace gases and meteorological parameters measured on DC-8 flights during INTEX-NA.

- Investigate chemical transformation of mercury in various atmospheric environments using data analysis and chemical box modeling.

LIST OF TABLES

LIST OF FIGURES

ABSTRACT

CONTINENTAL OUTFLOW OF POLLUTED AIR FROM THE U.S. TO THE NORTH ATLANTIC AND MERCURY CHEMICAL CYCLING IN VARIOUS ATMOSPHERIC ENVIRONMENTS

by

Su Youn Kim

University of New Hampshire, December, 2010

The dissertation consists of two topics. The first was continental outflow from the U.S. to the North Atlantic with a case study of NASA DC-8 flight 13 during the Intercontinental Chemical Transport Experiment – North America. This study found two interesting results. First, pollutants in the southeastern U.S. boundary layer were transported to the upper troposphere over the North Atlantic by vertical transport, which was facilitated by convection and warm conveyor belt uplifting combined with fast southwesterly flow in the free troposphere. Secondly, the data suggest that the total tropospheric column over the North Atlantic was impacted by U.S. outflow in various stages of photochemical aging. The second topic was a study of Mercury Depletion Events (MDEs) in the Arctic springtime and mercury chemical transformation in the northeastern U.S. MDEs were studied by simulations using a chemical box model and data analysis of NASA DC-8 flights during the Arctic Research of the Composition of the Troposphere from Aircraft and Satellites field campaign. A chemical box model was developed considering only gaseous reactions of mercury, halogens, and ozone chemistries. Several idealized sensitivity experiments based on data analysis were

simulated to study what factors were most important to MDE formation. The box model captured similar patterns as the measurements which were high Br_2, O_3 depletion, and decline of ethyne and light weight alkanes inside the MDE areas. The simulations indicated that a continuous high Br_2 mixing ratio, high intensity of solar radiation, and a high NO_x regime caused faster $Hg°$ depletion. Furthermore, the mercury diurnal cycle in the northeastern U.S. was studied with the box model and data analysis of year-round continuous measurements at the AIRMAP Thompson Farm site. The mass transport between gaseous-aqueous phases and aqueous reactions were added into the box model. Diurnal cycles of $Hg°$ showed that it decreased ~40 ppqv on stable nights. Box model simulations indicated that the decreased amount of $Hg°$ was facilitated by water solubility of $Hg°$ and uptake into the liquid water content of aerosols. Moreover, the sensitivity experiments with dry deposition added indicated that the ambient PHg level was strongly influenced by this process.

I. Continental Outflow of Polluted Air from the U.S. to the Upper Troposphere over the North Atlantic during the NASA INTEX-NA Airborne Campaign

1. Introduction

Continental outflow plays an important role in influencing the chemical environment of the remote troposphere through long-range transport of natural and anthropogenic trace gases and aerosols. Extensive airborne measurements over the Pacific during NASA field campaigns such as PEM-WEST B and TRACE-P have characterized the chemical composition of Asian outflow (Talbot et al.; 1997, Blake et al., 2003; Bartlett et al., 2003). Moreover, Asian dust and anthropogenic pollutants via trans-Pacific transport can impact air quality in the U.S. (DeBell et al., 2004; Jaffe et al., 1999, 2003). Recently, long-range transport of Saharan dust over the Pacific route to western North America has been documented in the middle troposphere (McKendry et al., 2007).

One important component of the continental outflow over the north Pacific (Talbot et al., 1996a, 1997) and south Atlantic (Talbot et al., 1996b) basins is wet convective lifting of air masses over the continent with subsequent enhancement in mixing ratios of insoluble trace gases in downwind areas over the ocean at altitudes above 8 km. For example, over the north Pacific Crawford et al. (2003) reported enhanced mixing ratios of CO in the entire 1-11 km vertical column of a cloud impacted area during TRACE-P. A case of deep convective lofting was also obtained during TRACE-A, where a NASA DC-8 flight in the vicinity of a meso-scale complex moving across burning Brazilian savannah measured high levels of biomass combustion products in the middle-to-upper troposphere (Bartlett et al., 1996; Pickering et al., 1996). These

scenarios are highly conducive to long-range transport of pollutants due to faster zonal winds aloft and reduced photochemical reactivity.

The International Consortium for Atmospheric Research on Transport and Transformation (ICARTT) field campaign was designed and conducted to gain a better understanding of factors influencing large-scale air quality over North America, the North Atlantic, and western Europe (Fehsenfeld et al., 2006). ICARTT measurement platforms used for studying intercontinental transport included aircraft, ship, satellites, sondes, autonomous balloons, and ground sites that were all operational during July-August 2004. Five types of the North America outflow were classified, which were two types of low level transports, fire plumes, and upper and lower level export by fronts (Methven et al., 2006). Unlike Asian outflow which has been characterized extensively by combustion tracers, a large suite of nonmethane hydrocarbons (NMHCs), and aerosol composition, North America pollutant outflow over the Atlantic has focused largely on ozone (O_3) and CO (Dickerson et al., 1995; Mao et al., 2006; Millet et al., 2006; Parrish et al., 1993). North American outflow was characterized comprehensively for its chemical composition during the ICARTT field campaign. Specifically, the large variations in ratios between the pentyl and C_2-C_4 nitrates over the North Atlantic indicated the impact of different parent hydrocarbons emissions from the U.S. to the North Atlantic by photochemical production during transport from the source regions (Reeves et al., 2007). Canadian and Alaskan forest fires emissions caused elevated CO, PAN, organic compounds and aerosols. Moderately high levels of CO and longer-lived hydrocarbons were found in about 44% sampled data which originated from North America by low and upper level outflow (Lewis et al., 2007).

In the Northeastern U.S. a primary mechanism for continental outflow is a warm conveyor belt (WCB) transport where a mature cyclone lifts air masses from the boundary layer up into the westerly flow in the upper troposphere (Cooper et al., 2001). The U.S. plumes lofted to the free troposphere by the WCB can affect air quality in Europe within a few days (Stohl et al., 2003). An extensive field campaign linked elevated trace gases mixing ratios in the lower troposphere over Scandinavia including Alpine areas, to polluted air that was lifted into the free troposphere by the WCB over the eastern U.S. (Huntrieser et al., 2005). A recent modeling study suggested that in summer air masses in the central and southeastern U.S. may be lofted to the free troposphere by convection followed by export to the North Atlantic by the semi-permanent anticyclone (Li et al., 2005). They also pointed out that U.S. regions with the most frequent occurrence of deep convection were the Midwest, the Gulf Coast, and the East Coast. The Gulf Coast and off the East Coast of the United States were also found to be influenced by deep convection during SONEX field campaign over the Atlantic, which was conducted in October – November1997, by determining lightning activity (Fuelberg et al., 2000).

Here we present a case study of convective uplifting of polluted air to the free troposphere over the southeastern U.S. coupled with rapid transport to the North Atlantic. We utilized data obtained primarily on flight 13 of the NASA DC-8 during the Intercontinental Chemical Transport Experiment – North America (INTEX-NA) component of ICARTT (Singh et al., 2006).

2. Methods

2.1. Measurement data

INTEX-NA was performed over North America and the adjacent North Atlantic Ocean using the NASA DC-8 aircraft to examine the large-scale distribution of trace gases and aerosols associated with the North America continent (Singh et al., 2006). This study focused on flight 13 which was conducted on July 28, 2004 with one of the main objectives being sampling of U.S. continental outflow as described in Methven et al. (2006) and Arnold et al. (2007). The DC-8 took off at about 12 UTC from the Pease International Airport in New Hampshire and landed at around 22 UTC, yielding a flight duration of about 10 hours. The flight route, shown in Figure 1.1, was located over the North Atlantic near the most northerly position of a stationary front and near the southern end of a cold front (Figures 1.1 and 1.2).

A brief description of the overall measurement package on the DC-8 was provided previously in Singh et al. (2006). The principal trace gases of interest here were CO, CH$_4$, CO$_2$, COS, and a suite of NMHCs and halocarbons which are archived and available at
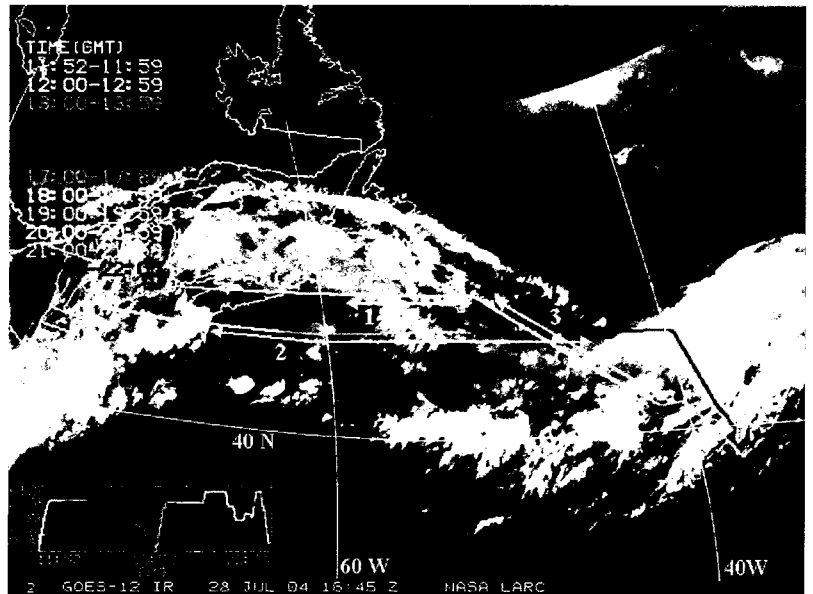
Figure 1.1. Flight 13 route and the three regions in upper troposphere.

http://www-air.larc.nasa.gov/cgi-bin/arcstat. The majority of the data, including CO and

CH_4, were obtained by the University of California – Irvine (UC-Irvine) (Blake et al., 2003; Colman et al., 2001). Carbon dioxide was measured as described by Vay et al. (1999). Only flight 13 data collected over the Atlantic east of 70°W was used in our analysis. We used relationships between CH_4, CO, CO_2, and COS in boundary layer air (<2 km) over the southeastern U.S., determined using all the INTEX-NA DC-8 flight data (flights 6, 7, 10, 12, 16, and 19) obtained over the continent at latitudes <35°N, to understand the vertical distribution of trace gases along the flight 13 track. These are all long-lived trace gases, with CO having the shortest lifetime of about 1 to 2 months in summer the range of OH concentration over 1.0×10^6 - 1.8×10^6 molecules cm^{-3} (Brasseur et al., 1999; Mak and Southon, 1998). Thus, these trace gases are photochemically stable so that dynamical process are the most important factors determining their distribution downwind from North America on the transport time scales important to this analysis. NMHCs and halocarbons used in this study were mainly the urban and industrial tracers, C_2Cl_4, i-C_5H_{12}, $CHCl_3$, and C_6H_6 (Wang et al., 1995; Chan et al., 2006; Aucott et al., 1999; Na et al., 2001), and a combustion tracer, C_2H_2.

We also utilized "Measurement of OZone, water vapor, carbon monoxide and nitrogen oxides by AIrbus in-service airCraft (MOZAIC)" to examine the vertical distribution of key trace gases over the east coast during the time period of flight 13. MOZAIC uses autonomous instruments loaded into five long-range passenger airliners, namely AIRBUS 340 - 300 aircraft. Of particular interest here was the four second data obtained on a flight from Vienna, Austria to Washington, D.C. (U.S.A.) on July 28, 2004. This dataset provided additional information on the vertical profiles of O_3 and CO over

the eastern U.S. between 60°W - 78°W and 38°N - 48°N obtained during descent into the Washington area.

Ground-level data from the AIRMAP measurement network (http://airmap.unh.edu) in the northeastern U.S. for two days in July (27 and 28) 2004 were also utilized in this study. The NMHCs and CO data from Thompson Farm (TF) in Durham, New Hampshire (23 m elevation, 43.11°N and 70.95°W) were 40 minute averages and those from the second location on Appledore Island (AI), ME (sea level, 42.97°N and 70.62°W) were 1 hour averages (Sive et al., 2005; Zhou et al., 2005). Methane and CO in ambient air were surveyed for selected U.S. cities by the UC-Irvine group using canisters (Baker et al., 2008). Specifically, we used monthly average values for August collected in the southeastern U.S. cities of Birmingham, Alabama and Baton Rouge, Louisiana during 2001, and Charlotte, North Carolina and Knoxville, Tennessee in 2002, and El Paso, Texas in 2003.

2.2. Backward trajectories and photochemical ages

Backward trajectories in combination with an analysis of synoptic conditions and photochemical ages can be an effective method to understand air mass transport. Kinematic backward trajectories were calculated at one minute time steps throughout the INTEX-NA flight series by Florida State University (http://fuelberg.met.fsu.edu/research/intexa/realtime/). The ratio of C_3H_8/C_2H_6 was used for comparing the relative photochemical age of air masses (McKeen and Liu, 1993; Parrish et al, 2004). To assess the relative transport time from the boundary layer in the southeastern U.S. to the flight legs over the North Atlantic, we utilized the chemical

clock provided by the reactivity of C_3H_8 and C_2H_6 with OH. Equation (1.1) was used to estimate the transport time:

$$\Delta t = \frac{\ln \dfrac{(r(C_3H_8)/r(C_2H_6))_0}{(r(C_3H_8)/r(C_2H_6))_t}}{(k_{C_3H_8} - k_{C_2H_6})[OH]} \qquad \text{(Equation 1.1)}$$

Here, $(r(C_3H_8)/r(C_2H_6))_0$ is the ratio of the mixing ratios of the two compounds in the boundary layer, $(r(C_3H_8)/r(C_2H_6))_t$ is the same ratio at a later time t for each of the flight leg regions of interest, k is the OH reaction rate constant, and [OH] is OH concentration. The DC-8 flight data showed that $(r(C_3H_8)/r(C_2H_6))_0$ had a mean value of 0.36 ± 0.15 (n = 66) for the boundary layer over the southeastern U.S. (hereinafter SBL).

As input for the estimates we used the measured OH mixing ratios, ambient pressures, and air temperatures measured on the DC-8 flights in the SBL. Mean values were 0.18 pptv for OH, 0.92 atm for pressure, and 294 K for temperature, which resulted in a concentration of 4.1×10^6 OH molecules cm^{-3} in the SBL. We used rate constants for C_3H_8 and C_2H_6 of 1.1×10^{-12} cm^3 molecule^{-1} s^{-1} and 2.3×10^{-13} cm^3 molecule^{-1} s^{-1} respectively at 294 K (Sander et al., 2003).

3. Synoptic meteorology

Shown in Figure 1.2. a-f are maps of sea level pressure (SLP) for 12 UTC on July 25 and 12UTC on July 28, 500 and 300 hPa geopotential heights for 00 UTC on July 26 and 12 UTC on July 28. Together these define the surface, middle and upper tropospheric circulation patterns across the U.S. on the flight day and a few days prior to it. The circulation system that facilitated the transport pattern of Flight 13 evolved from a Canadian Low with cold and warm fronts situated north of Quebec, Canada at 12 UTC on July 21, as shown in the 6 hourly analyzed SLP. This low pressure system was moving
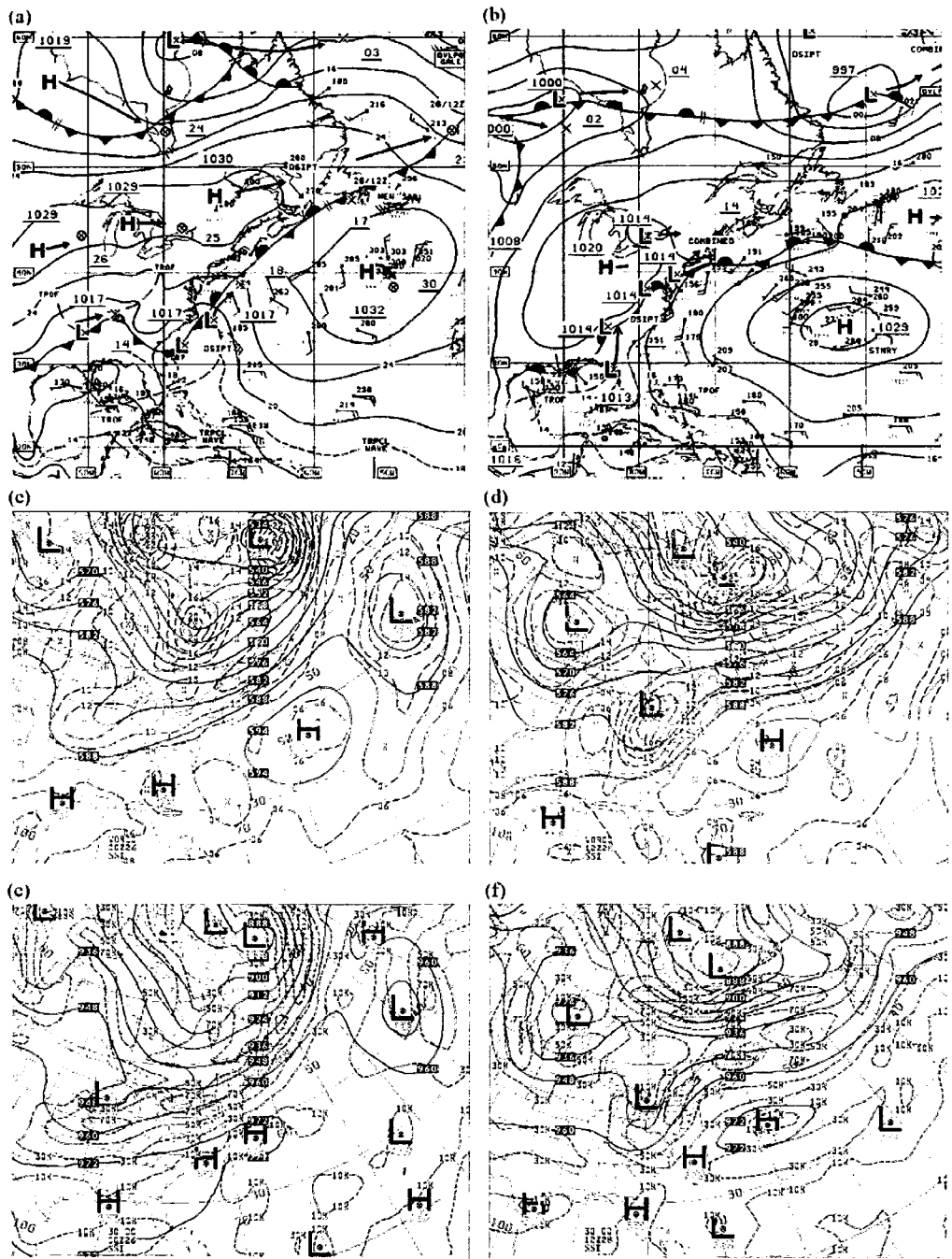
Figure 1.2. Analyzed sea level pressure (a and b) for 12UTC July 25, 2004 and 12UTC July 28, 2004, 500hPa geopotential height (c and d), 300hPa geopotential height (e and f) for 00UTC July 26, 2004 and 12UTC July 28, 2004.

eastward with the warm front evolving into an occluded front over the North Atlantic at

12 UTC on July 23, and the cold front remaining largely over the eastern U.S. through

00UTC on July 24.

The cold front became a stationary front that was located over the eastern U.S. and the western Atlantic starting at 12 UTC on July 24 (Figures 1.2 a and b) and it persisted throughout the duration of flight 13. It should be noted that several small short-lived cyclones were generated in association with the stationary front. In particular, one of these small disturbances was generated over the southeastern U.S. at 06 UTC on July 26 and matured into a cyclone which propagated to the Virginia area over the following 24 hours. Accompanying the cold front associated with this small cyclone was a WCB over the Southeast. These disturbances and associated WCB are conducive to lifting of boundary layer air masses to the free troposphere.

The 500 hPa geopotential heights at 12 UTC on July 23 showed that a trough associated with the Canadian Low was situated over the northern Great Plains. This trough traveled across the Midwest (Figure 1.2 c) and reached southern Canada in the vicinity of the Great Lakes at 12 UTC on July 28 (Figure 1.2 d). It subsequently moved northeastward relatively fast and weakened over the North Atlantic Ocean. While the influence of this trough existed over the U.S. until 00 UTC on July 30, another trough formed over southern Canada at 12 UTC on July 28 (Figure 1.2 d).

The flow patterns at the 300 hPa geopotential height and isotachs resembled those at the 500 hPa level (Figures 1.2 e and f). Zonal wind speeds on the 300 hPa level were generally 5 - 25 m/s over the U.S., and increased to >35 m/s in the jet stream over the northeastern U.S. In general, the jet stream on downwind side of trough is associated with upward motion (Holton, 1995), which facilitates air mass movement from lower altitudes to the upper troposphere with subsequent transport over long distances. Overall, the maps of geopotential height at 500 hPa and 300 hPa together suggested a dynamic

westerly flow regime in the mid-to-upper troposphere.
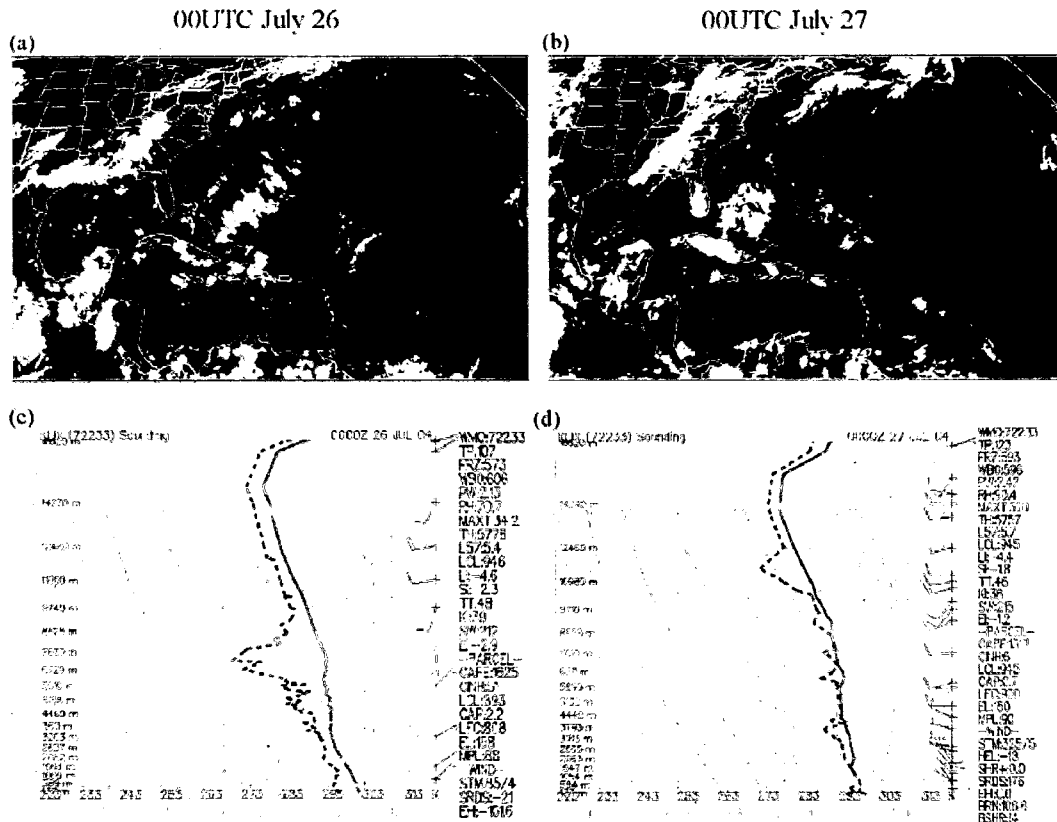
Figure 1.3. GOES infrared images (a and b), and skew T and log P diagram (c and d) at the Slidell, Louisiana (30.33 °N and 89.82 °W) for 00 UTC July 26, 2004 and 00 UTC July 27, 2004.

GOES infrared imagery and skew T and log P diagrams at 00 UTC on July 26 and 27 suggested a strong possibility of upward transport of air masses from the surface during that time period (Figure 1.3 a-d). GOES infrared imagery (Figures 1.3 a and b) revealed the presence of high clouds over the eastern U.S. except in coastal regions, extending from Texas eastward to western South Carolina and northeastward to New England. These images indicated cloud top temperatures of 200K (~14 km altitude), providing the possibility of strong deep convection. Manually digitized radar (MDR) is the best indicator of convection, and Figures 1.4 a-f showed very large convection

(a) 18 UTC July 25

(b) 00 UTC July 26

(c) 18 UTC July 26

(d) 00 UTC July 27

(e) 20 UTC July 27

(f) 00 UTC July 28

Intensities (Dbz): 20■ 30▨ 40■ 45 50■ 55■
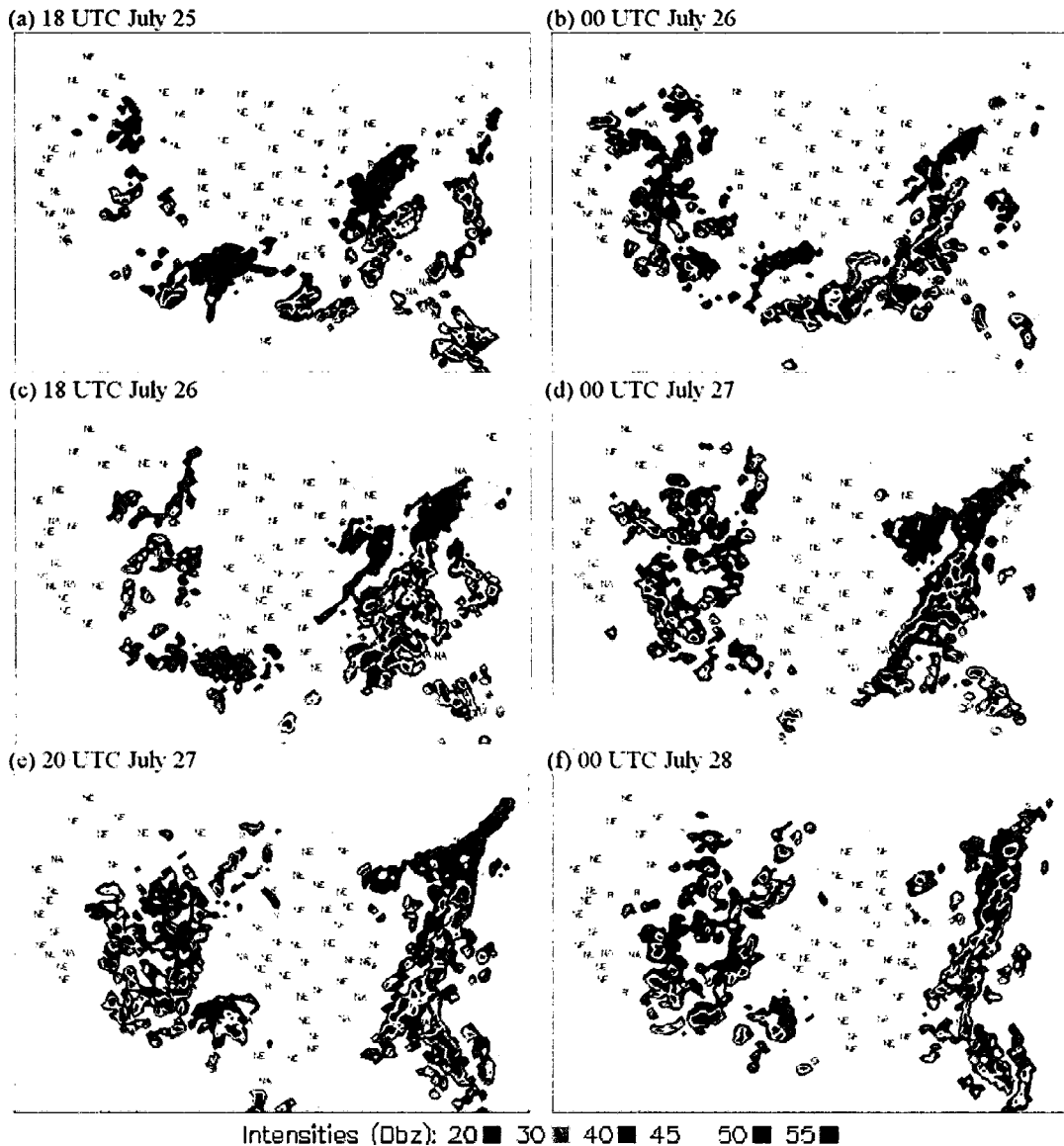
Figure 1.4. Manually Digitized Radar images for 18 UTC and 00UTC July 25 – 28, 2004. The image of 18 UTC July 27 is not available, so 20 UTC was in this

occurred over the southeastern and eastern U.S. in the afternoon to the evening for about 3 days between July 25 – 27. Moreover, the area of high clouds coincided with heavy precipitation indicated by the MDR (Figures 1.3 a-b and 1.4 a-f). Images of other times through 00 UTC on July 28 were also examined, and they uniformly suggested similar conditions conducive to convection in this same region.

Furthermore, Skew *T* diagrams at individual locations from the eastern U.S. verified the likelihood of convection. The convective available potential energy (CAPE) and Lifted Index (LI) on the Skew *T* diagrams (Figures 1.3 c and d) from the Slidell, Louisiana (30.33 °N and 89.82 °W), during July 25 to 27 were used to diagnose the presence of local convection. The CAPE values within the range of 1000 – 2500 J/kg and LI less than -4, all falling into the criteria for unstable and convective atmospheric conditions (http://www.theweatherprediction.com/ severe/indices/).

In summary, our synoptic analysis suggested that a stationary front associated with a Canadian cyclone over the eastern U.S. continuously induced convection several days before July 28, which facilitated fast transport of air masses from the boundary layer to the free troposphere. The WCB over the southeastern U.S. also contributed to the vertical transport as indicated by the spawning of small cyclones in association with the stationary front. The mixed effects of widespread convection and the WCB over the southeastern U.S. overlapped in their occurrence during July 25 – 28, 2004, and were also described in Kiley et al. (2006) and Cooper et al. (2006). All meteorological evidence consistently pointed to combined vertical transport via convection and WCB uplifting combined with fast eastward transport in the free troposphere over the eastern U.S. during the two days prior to flight 13. In the following sections of this paper we examined the chemical signatures measured at high altitude over the Atlantic to provide support for the meteorological analysis conducted for flight 13.

4.   Notable chemical characteristics of flight 13

The vertical distribution of mixing ratios of CO, CH_4, CO_2, and COS is displayed for the flight data east of 70°W in Figure 1.5. Note that data at altitudes <5 km was

obtained near 40°W, not directly underneath of flight legs at altitudes >5 km (Figures 1.1 and 1.5). Mixing ratios of CO near the surface were 70 to 80 ppbv followed by a decrease to the lowest values of ~60 ppbv at 2 km. At altitudes between 2 and 5 km, CO increased to 80 ppbv, and then continued to rise quickly above 5 km varying over a range of 78 − 134 ppbv at altitudes >8 km. The vertical profile of CH_4 tracked CO closely, which exhibited levels of 1760 to 1770 ppbv near the surface followed by a slight decrease at 2 km. Between 2 and 5 km CH_4 again hovered around 1770 ppbv. An increasing trend with altitude was accelerated above 5 km, where CH_4 was enhanced up to 1843 ppbv at 8 − 11 km.

The vertical profiles of CO_2 and COS showed trends opposite those of CO and CH_4. Mixing ratios of CO_2 were ~376 ppmv near the surface, and then increased to 377 ppmv at 2 km followed by a decrease to ~375.5 ppmv between 2 and 5 km and further decrease above 5 km. The minimum value of 372.4 ppmv was observed in the 8 − 11 km region. COS tracked CO_2 closely with mixing ratios varying over 455 - 475 pptv near the surface, increasing to 480 pptv at 2 km, and then decreasing gradually to 455 pptv between 2 and 5 km. The lowest COS mixing ratios near 410 pptv were found at 8 - 11 km.

To understand the causes for the high mixing ratios of CO and CH_4 that occurred in the 8 − 11 km altitude region, we identified three time periods with the most enhanced levels (Figure 1.1). These occurred on constant altitude flight legs, with the first region at 10.4 km over the time period of 19 - 20 UTC, the second at 8.9 km during 12:20 - 14:40 UTC, and the third at 8.5 km over 17:30 - 19:00 UTC. All other segments of the flight

are referred to as "Outside" (i.e., outside of the three regions), and they are discussed in Section 5.
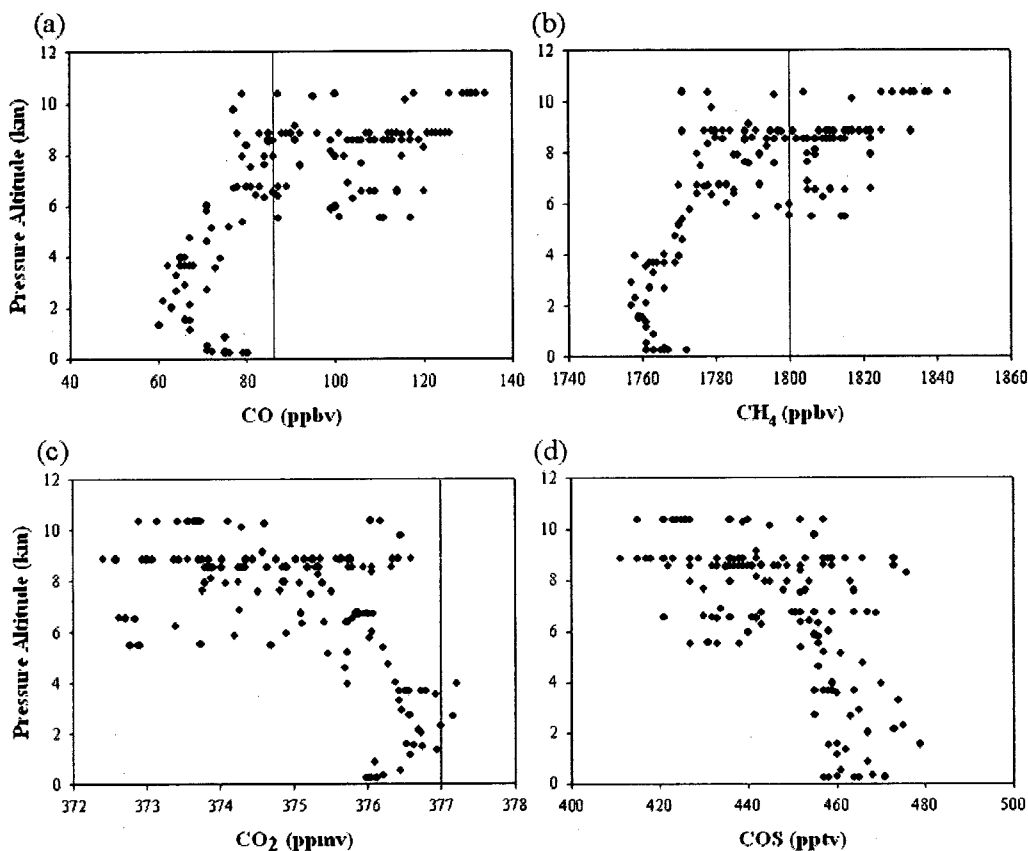
Figure 1.5. Vertical distribution of (a) CO, (b) CH_4, (c) CO_2, and (d) COS. Lines in the graphs are for monthly average mixing ratios in July, 2004 in Bermuda.

First, we used trace gas data from the NOAA Global Monitoring Division (GMD) monitoring site on Bermuda (http://www.esrl.noaa.gov/gmd/dv/ftpdata.html) and from Mace Head, Ireland (Simmonds et al., 2006) to determine representative background mixing ratios over the North Atlantic. The monthly average surface mixing ratio at Bermuda in July 2004 was 1800 ppbv for CH_4, 86 ppbv for CO, and 377 ppmv for CO_2. The mean mixing ratio of C_2Cl_4 at Mace Head, Ireland was 4.94 ± 0.06 pptv from

- 14 -

measurements over the period of 2000 to 2004 (Simmonds et al., 2006). In two rural areas of the U.S., annual mean surface mixing ratios of COS from February 2002 to February 2005 were 444 ± 8 pptv in Wisconsin and 441 ± 8 pptv at Harvard Forest, Massachusetts (Montzka et al., 2007).

Statistics are provided in Table 1.1 to describe the chemical environment of the three regions of enhanced mixing ratios. CO, C_2H_2 and C_2Cl_4 exhibited mean mixing ratios of 127 ppbv, 117 pptv and 10.2 pptv, respectively, in region 1, 106 ppbv, 93 pptv and 5.1 pptv in region 2, and 109 ppbv, 94 pptv and 5.5 pptv in region 3. Correspondingly, in regions 1, 2, and 3 the mean value of CH_4 was 1831 ppbv, 1805 ppbv, and 1808 ppbv respectively. Compared to the background levels over the North Atlantic, the mean levels of CH_4, CO, and C_2Cl_4 in regions 1, 2, and 3 were higher by 0 – 1.7%, 23 – 48%, and 3.3 – 106% respectively. Mixing ratios of CS_2, whose primary source is chemical industrial processing (Chin and Davis, 1993), were mainly less than 4 pptv in each region with occasional levels up to 14 pptv. Overall, the three regions showed a clear influence of urban combustion emissions.

The air mass transport time to the free troposphere can be estimated by combining hydrocarbon lifetimes and trajectories whether the transport was by the WCB on the synoptic scale or mesoscale convection (Purvis et al., 2003). This transport was investigated here using backward trajectories combined with photochemical age estimates of air masses in regions 1-3. Kinematic 5-day backward trajectories arriving in each of the three regions are presented in Figure 1.6. Since many of the air masses appeared to meander over the southeastern U.S. for several days, 10-day backward trajectories (not shown) were used to examine the long-range transport of these air

masses to the U.S. In the case of region 1, these trajectories showed mainly two origins, with one from over the eastern Pacific/U.S. west coast and the other from the Gulf of the Mexico. These air masses arrived over the southeastern U.S. in the mid-to-upper troposphere, and then spent ~4 days over the southeastern U.S. in the altitude region of 550 to 300 hPa. Eventually they were transported in <20 hours from over the Virginia area at 00 UTC on July 28 to region 1 in the upper troposphere (>350 hPa). The mean value of C_3H_8/C_2H_6 was 0.23 ± 0.02 in region 1, and photochemical aging of an SBL air mass arriving in region 1 was 1.5 days based on equation (1.1).

(a) region 1   (b) region 2

(c) region 3   (d) Outside
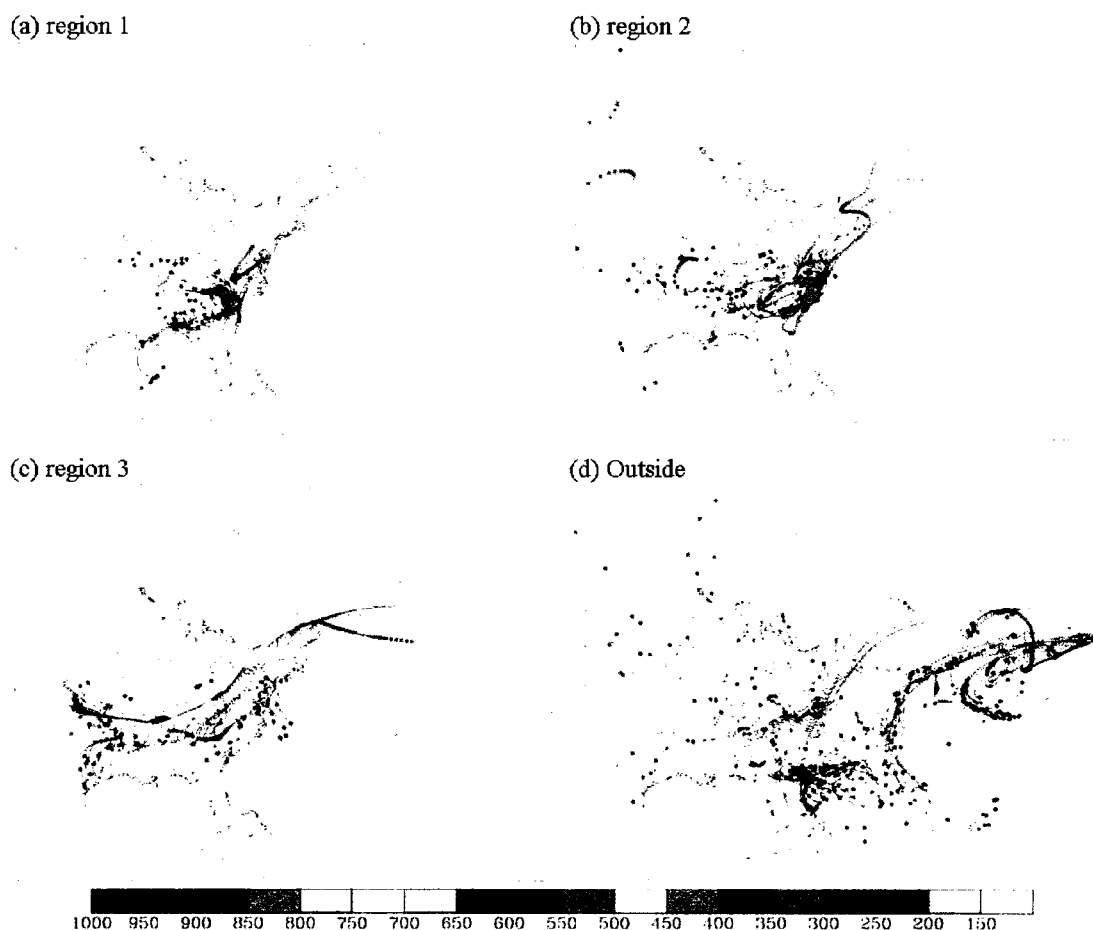
Figure 1.6. Kinematic 5-day backward trajectories for each region. Big dots are at 00 UTC on each day and the small ones are other hours. Unit of color bar is hPa.

Table 1.1. Chemical characteristics of flight regions and boundary layer in southeastern U.S. $\bar{x}$ (σ) is mean(standard deviation) and $q_{0.5}$ means median. The n right below the regions is the data number in each region. The units of the compounds are as follows; ppmv for CO_2, ppbv for CH_4, CO and O_3, particles/cm³ for UCN (ultra fine aerosol), and pptv for the other compounds.

	Region 1 (n=12)			Region 2 (n=28)			Region 3 (n=24)			Outside(n=94)			Southeastern Boundary (n=66)		
	$\bar{x}$ (σ)	$q_{0.5}$	range	$\bar{x}$ (σ)	$q_{0.5}$	range	$\bar{x}$ (σ)	$q_{0.5}$	Range	$\bar{x}$ (σ)	$q_{0.5}$	range	$\bar{x}$ (σ)	$q_{0.5}$	Range
CH_4	1831 (10)	1833	1804-1843	1805 (17)	1812	1771-1833	1808 (8)	1810	1782-1822	1781 (18)	1778	1757-1822	1823 (35)	1820	1764-1890
CO	127 (9)	130	100-134	106 (16)	113	78-126	109 (8)	110	86-119	84 (16)	80	60-120	122 (35)	117	76-212
CO_2	373.6 (0.3)	373.6	372.8-374.2	374.5 (1.2)	374.4	372.4-376.6	374.8 (0.8)	374.6	373.7-376.4	375.4 (1.2)	375.9	372.6-377.3	370.2 (6.8)	373.0	356.4-379.1
COS	426 (7)	425	415-440	437 (18)	433	411-473	440 (11)	438	422-473	453 (13)	456	421-479	420 (40)	429	344-485
O_3	85 (6)	86	71-92	75 (16)	73	48-103	64 (7)	63	50-76	53 (21)	55	14-101	48 (11)	48	27-79
C_2H_2	117 (16)	122	79-130	93 (28)	101	38-136	94 (14)	97	55-118	45 (29)	41	11-178	140 (96)	120	32-428
C_2Cl_4	10.2 (2.0)	10.4	5.3-12.4	5.1 (1.6)	5.5	2.6-7.6	5.5 (1.1)	5.5	3.4-6.9	3.4 (1.9)	2.6	1.5-9.3	5.8 (4.2)	4.2	1.7-19.6
C_2H_6	928 (96)	937	659-1089	875 (143)	892	529-1036	974 (161)	918	727-1311	571 (228)	614	258-1031	1172 (597)	1013	370-3458
$i\text{-}C_5H_{12}$	9 (3)	9	3-13	12 (5)	14	4-19	12 (4)	13	3-17	7 (3)	7	3-16	109 (84)	93	15-506
C_6H_6	10 (3)	11	5-13	16 (6)	18	5-24	17 (3)	17	10-22	10 (6)	9	3-43	45 (30)	38	6-160
$CHCl_3$	10.5 (0.8)	10.7	8.9-11.2	9.4 (1.0)	9.7	7.9-10.8	9.6 (0.8)	9.5	8.3-11.4	7.8 (1.0)	7.5	6.2-9.6	10.6 (2.9)	10.2	6.5-16.8
CF_2ClBr	4.67 (0.12)	4.66	4.47-4.84	4.29 (0.05)	4.30	4.19-4.36	4.32 (0.09)	4.32	4.18-4.61	4.23 (0.11)	4.19	4.09-4.59	4.33 (0.08)	4.33	4.13-4.49
UCN	10172 (2436)	10833	2476-11340	1482 (975)	1400	146-3574	1998 (1168)	1548	720-5517	1542 (2348)	694	129-10427	3988 (3852)	2611	334-15327
CS_2	3.2 (3.6)	1.5	1.1-14.0	4.0 (2.5)	3.2	1.2-11.2	2.7 (1.8)	2.1	1.2-9.3	3.2 (2.9)	2.4	1.1-21.0	9.3 (7.9)	6.8	1.7-39.2

The backward trajectories for region 2 illustrated a complex dynamical situation. In this case there were a large number of trajectories indicating that the air spent 3-4 days over the southeast U.S. at altitudes ranging from near the surface to 500 hPa. In addition, approximately 13% of the trajectories followed zonal westerly flow at 300 hPa which intercepted the air masses residing over the southeast U.S. for several days. Ten-day backward trajectories indicated that the inflowing air had arrived from over the northwestern U.S., the North Pacific, and the Gulf of the Mexico. On July 27 this mixture of air masses was quickly advected over the Northeast, and arrived at the flight altitude on July 28. The value of C_3H_8/C_2H_6 was 0.20 ± 0.04 in this region, and the photochemical aging of an SBL air mass arriving in region 2 was 2 days.

Air masses transported to region 3 had their origin over mainly the south central and southeastern U.S. It appears that boundary layer air over eastern Texas was advected at low level to the southeastern states and mixed with SBL air during vertical lifting on July 27 and mid-tropospheric air masses that originated over the Oklahoma/Colorado area. On the 28th the air passed over the Northeast in the mid-troposphere and arrived at the flight altitude of 8.5 km nearly coincident in time with the region 1 air masses. It appears that it took about 1.7 days to reach the air masses to the flight region 3. The value of C_3H_8/C_2H_6 was 0.22 ± 0.03 in region 3, and photochemical aging of an SBL air mass arriving in this region was 1.7 days.

We also estimated the chemical clock transport times in these three regions using ratios of ethyne/CO and trichloroethylene/tetrachloroethylene (C_2HCl_3/C_2Cl_4). In general, these produced variable transport times that varied by up to a factor of two from C_3H_8/C_2H_6. Using a lower OH concentration suggested by Arnold et al. (2007) also

produced transport times that were about two times longer. We believe that for flight 13 the trajectory estimated transport times are more reliable that those estimated by the chemical clock method. This likely due to the air masses lingering over the U.S. for several days and entraining multiple inputs of boundary layer air by convection over the SBL. This likely produced a very mixed air mass of various ages and is responsible for the inconsistent chemical clock transport times.

Backward trajectories and the synoptic weather patterns indicated that the SBL air masses were sampled in regions 1-3 due to their fast transport through convection and the WCB that developed in association with the stationary front. Ultrafine aerosol showed distinct mean differences of 10,172 particles/cm^3 in region 1, 1,482 particles/cm^3 in region 2, and 1,998 particles/cm^3 in region 3. A high degree of correlation between enhanced condensation nuclei number densities and mixing ratios of CO, CH_4, NO, and OH has been observed in air masses influenced by deep convection over the central U.S. (Twohy et al., 2002). However, we did not find such correlation in the three regions in spite of the very high concentrations of ultrafine aerosols and increased mixing ratios of CO. Wang et al. (2000) observed high concentration of condensation nuclei (>10,000 cm^{-3}) in the upper troposphere associated with convection using the NO/NOy ratio as a chemical clock. They also pointed out that high CN concentration from aircraft emissions in the upper troposphere was not sampled frequently because of faster dilution than the transport of the boundary layer air aloft via convection. Although our results do not parallel those of Twohy et al. (2002), our analysis implies an impact of convective outflow in region 1 similar to the analysis of Wang et al. (2000). In addition, a diagnostic indicator of wet convection is the ratio of CH_3OOH/H_2O_2, since H_2O_2 is removed

preferentially by wet scavenging compared to CH_3OOH resulting in ratio values >1 (Talbot et al., 1996b). Snow et al. (2007) found that ratios of <1 for H_2O_2/CH_3OOH and <100 ppbv for O_3 indicated convection during the ICARTT study. The flight 13 measurements showed lower mean values of H_2O_2/CH_3OOH which were 1.3, 2.6, and 2.2 in regions 1-3, respectively, than a value of 3.1 from the SBL. The ratio ranges were 0.77 – 2.15 for region 1, 0.25 – 5.34 for region 2, and 1.16 – 3.72 for region 3, suggesting that convection impacted regions 1 and 2. Overall, our analysis suggests that region 1 was mostly influenced by deep convective vertical transport, whereas regions 2 and 3 appear to be dominated by lofting of air by the WCB.

The photochemical ages estimated from C_3H_8/C_2H_6 in regions 1, 2, and 3 are reasonably similar to the transport times deduced from the backward trajectories which corroborates fast transport with minimal apparent dilution of SBL air by aged background air. Evidence for minimal mixing is provided by similar mixing ratios of $CHCl_3$ between regions 1-3 (9.4 – 10.5 pptv) and SBL (10.6 pptv). Additional evidence is the preserved low mixing ratios of CO_2 and COS, which are typical of boundary layer air influenced by biospheric activity during the growing season. The mean mixing ratios of CO_2 in regions 1-3 were between 373.5 and 375 ppmv, and these were lower by 0.6 – 1% than the background mixing ratio from surface measurements at Bermuda. In comparison, mean mixing ratios of COS in regions 1, 2, and 3 (426 – 440 pptv) were closer to values found in the SBL over the U.S. The low mixing ratios of COS found in the upper troposphere during flight 13 is indicative of efficient terrestrial COS uptake in the SBL (Sandoval-Soto et al., 2005).

The backward trajectories suggested that the air masses arriving in the three study regions spent 1-4 days over the southeastern U.S. and were then transported to the Northeast and upward by fast zonal flow in the middle and upper troposphere on July 27-28. If the transport from the SBL to the flight regions was indeed rapid, then the effect of dilution and in situ chemical processing can be small, and subsequently the mixing ratios of trace gases in the source and flight regions should be similar. Mixing ratios of tracers in the SBL were thus compared with upper tropospheric values (Table 1.1). In general, industrial or urban tracers in the SBL exhibited higher levels than those in each flight region except for C_2Cl_4. This result is reasonable since some dilution would be expected during transport of SBL air to the upper troposphere. Enhanced mixing ratios of other urban tracers (e.g., C_2Cl_4 and $CHCl_3$) and high concentrations of ultrafine aerosol were also observed as evidence of urban impacted air masses in the upper troposphere. In the apparent SBL source region there are significant urban and industrial sources based on the emissions map of $CHCl_3$ (Aucott et al., 1999). The region is also widely covered with abundant vegetation as evidenced by isoprene emissions (Fiore et al., 2005), which accounts for uptake of COS and CO_2 and consequently their reduced mixing ratios.

MOZAIC measurements were used as an independent source of data on air mass composition over the Atlantic and eastern U.S. One of the instrumented flights into Washington, D.C. from Europe on July 28 was essentially routed through the region of interest here. MOZAIC data collected at 16:20 - 19:00 UTC on July 28 sampled the upper troposphere where the rapid transport of SBL air masses seemingly occurred from 00 UTC on July 27 to 16 UTC on July 28. The MOZAIC CO and O_3 spatial distributions are shown in Figure 1.7. According to the backward trajectories, region 1 of flight 13

and the MOZAIC sampling route overlapped geographically over New Brunswick, Nova Scotia, and the adjacent Oceanic area. The MOZAIC data showed mixing ratios of CO as large as 140 ppbv in the upper troposphere (~12 km). Ozone was between 74 and 110 ppbv for the data in the area with CO>100 ppbv, and a negative slope of -0.6 was identified for the O_3-CO correlation. Coincident high levels of CO and O_3 generally indicate polluted air masses, while high O_3 (O_3>100 ppbv) alone suggests a weak stratospheric influence. These data together with the flight 13 measurements support a broad influence of U.S. outflow to the upper troposphere over the Atlantic Ocean by the deep trough system. Upon descent into a polluted layer over Washington D.C., CO mixing

(a)
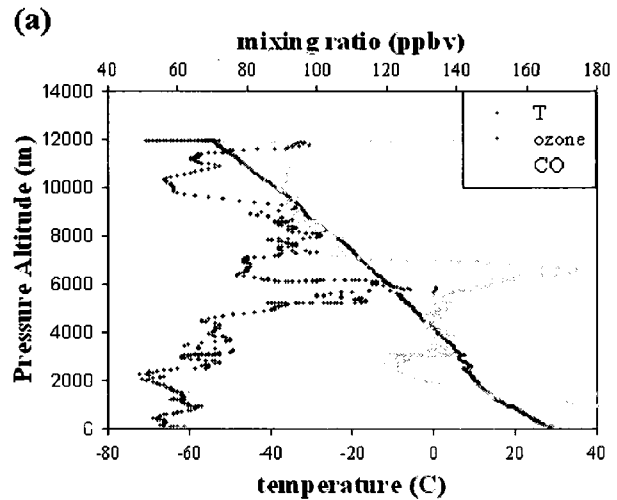
(b) O_3

(C) CO

Figure 1.7. The vertical profiles of temperature, O_3, and CO (a) obtained from the MOZAIC flights landing in Washington, D.C. on July 28, 2004, and the horizontal distributions of O_3 (b) and CO (c) during the flights. The unit of color bar is ppbv.

ratios up to 175 ppbv were identified between 5 and 7 km (39.9 - 40.5°N, and 75.6 – 76.6°W). This polluted layer likely originated in the boundary layer over the U.S. but did not get entrained in the flow pathway of the flight 13 upper tropospheric air masses. However, the HYSPLIT backward trajectories were not able to resolve this because of the inadequate vertical resolution.

We explored the possibility of an Asian impact on the flight 13 upper tropospheric study area as found on flights 3, 8, 10, 15 and 20 by Liang et al., (2007). Halon-1211 ($CBrClF_2$), an important tracer of Asian polluted outflow (Blake et al., 2003), averaged 4.3 pptv over the flight 13 route, similar to background levels in boundary layer air over the western Pacific during TRACE-P, 4.3 ± 0.04 pptv of $CBrClF_2$ (Barletta et al., 2006). Our backward trajectories analysis presented earlier and the key tracers indicated that Asian emissions did not affect directly the flight 13 region, and suggests that the outflow from the U.S. dominated the pollution in the study area.

5. Outside air mass chemical composition

As mentioned in section 4, the Outside air included all segments except measurements from regions 1-3. Hence different altitudes and geographical locations were mixed for the Outside data. The average chemical composition of the Outside air can be summarized to have an average composition of 84 ppbv CO, 375.4 ppmv CO_2, 1781 ppbv CH_4, 453 pptv COS, 45 pptv C_2H_2, 3.4 pptv C_2Cl_4, and 53 ppbv O_3. To find out whether the Outside chemical composition was similar to the North Atlantic background air, we again compared the airborne measurements with those from the NOAA GMD monitoring site on Bermuda and Mace Head (Simmonds et al., 2006). The results of this comparison showed that CH_4, CO, C_2Cl_4 and CO_2 were lower than at

Bermuda and Mace Head by 1.1%, 2.4%, 30.6%, and 0.4% respectively. Comparison of the mean values indicated that the Outside air was not affected by fresh urban and industrial source emissions. However, the mixing ratios of trace gases in the Outside air varied over wider ranges than those in regions 1, 2, and 3. In fact, maximum mixing ratios of CS_2, C_6H_6, and C_2H_2 were even larger than those in the three regions.

Backward trajectories for the Outside region indicated the possibility of air masses with diverse origins (Figure 1.6), which were categorized qualitatively into four source regions. The fractional contribution for each source region was estimated by comparison of the number of trajectories from each area to the total for the Outside. It was found that ~44% of air masses in the Outside area were from U.S. outflow, ~28% originated from the western Atlantic, ~20% from the remote Central Atlantic, and ~8% from over the North Pacific.

Chemical environments corresponding to the four source regions were summarized in Table 1.2. The average mixing ratio of CO, C_2H_2 and C_2Cl_4 were highest at 98 ppbv, 68 pptv and 5.4 pptv respectively in U.S. outflow, and lowest at 69 ppbv, 18 pptv and 1.8 pptv in air from the remote Central Atlantic. The average levels of O_3, CH_4, selected anthropogenic NMHCs, and ultrafine aerosol followed the same source distribution. For example, the average mixing ratio of O_3 showed the highest level of 70 ppbv in the U.S. outflow, and the lowest of 28 ppbv in air masses from the remote Central Atlantic. However, CO_2 and COS exhibited opposite variation, with higher mixing ratios from source regions far away from the North American continent. Specifically, the average mixing ratios of CO_2 and COS were 374.2 ppmv and 442 pptv respectively in the U.S. outflow, 376.0 ppmv and 457 pptv in air from the western

Table 1.2. Chemical Characteristics of "Outside" Air of the flight 13. Denotations and units are same as Table 1.1.

The outside	U.S. outflow (n=34)			The western Atlantic (n=29)			The remote Central Atlantic (n=26)			Pacific (n=5)		
	$\bar{x}$ (σ)	$q_{0.5}$	range	$\bar{x}$ (σ)	$Q_{0.5}$	Range	$\bar{x}$ (σ)	$Q_{0.5}$	range	$\bar{x}$ (σ)	$q_{0.5}$	range
CH_4	1798 (14)	1799	1771-1822	1775 (11)	1775	1757-1805	1764 (3)	1763	1759-1772	1789 (12)	1792	1775-1805
CO	98 (13)	100	77-120	77 (10)	78	61-106	69 (5)	68	60-80	98 (15)	100	84-120
CO_2	374.2 (1.1)	374.3	372.6-376.5	376.0 (0.6)	375.9	373.7-377.3	376.4 (0.3)	376.5	375.9-377.2	374.9 (0.4)	374.9	374.2-375.4
COS	442 (10)	442	421-464	457 (9)	457	430-475	463 (6)	461	455-479	459 (12)	457	445-476
O_3	70 (10)	71	44-92	54 (15)	55	23-83	28 (12)	25	14-47	63 (23)	57	43-101
C_2H_2	68 (18)	70	40-102	37 (15)	35	14-84	18 (3)	17	11-26	87 (55)	79	41-178
C_2Cl_4	5.4 (1.7)	5.2	2.6-9.3	2.4 (0.5)	2.4	1.6-4.3	1.8 (0.1)	1.7	1.5-2.2	3.9 (0.7)	4.1	2.9-4.5
C_2H_6	757 (112)	758	606-1002	561 (205)	577	258-1031	306 (24)	303	260-343	739 (142)	769	596-934
$i\text{-}C_5H_{12}$	8 (4)	8	3-16	6 (4)	6	3-8	NA	NA	NA	7 (2)	6	5-9
C_6H_6	12 (5)	11	3-23	7 (3)	6	3-12	NA	NA	NA	18 (15)	16	6-43
$CHCl_3$	8.7 (0.7)	8.9	7.3-9.6	7.3 (0.6)	7.3	6.3-9.3	7.0 (0.4)	7.1	6.2-7.6	8.8 (0.8)	9.1	7.7-9.6
CF_2ClBr	4.37 (0.1)	4.36	4.18-4.59	4.19 (0.06)	4.19	4.11-4.31	4.15 (0.03)	4.15	4.09-4.23	4.24 (0.05)	4.24	4.20-4.29
UCN	3390 (3387)	1840	355-10427	885 (557)	766	357-2666	328 (78)	340	180-447	343 (317)	218	129-809

Atlantic, 376.4 ppmv and 463 pptv from over the remote Central Atlantic, and 374.9 ppmv and 459 pptv from the Pacific. These results clearly show the role of the terrestrial biosphere in modulating CO_2 and COS in the troposphere downwind of a continental area.

6. Chemical characterization using correlation analysis

The slope of the standard linear regression between correlated chemical compounds can be a useful source identifier (Xiao et al., 2004). Based on the similar vertical distributions recognizable from Figure 1.5, correlation of the pairs CH_4-CO and COS-CO_2 was examined using all data from flight 13 (Figure 1.8). Carbon monoxide and CH_4 were correlated remarkably well at $r^2 = 0.92$. This implies that anthropogenic sources had a major impact on CH_4 mixing ratios at all altitudes sampled on flight 13 over the North Atlantic. The correlation between COS and CO_2 exhibited an $r^2 = 0.61$, likely driven to a large extent by their close association with vegetative uptake.
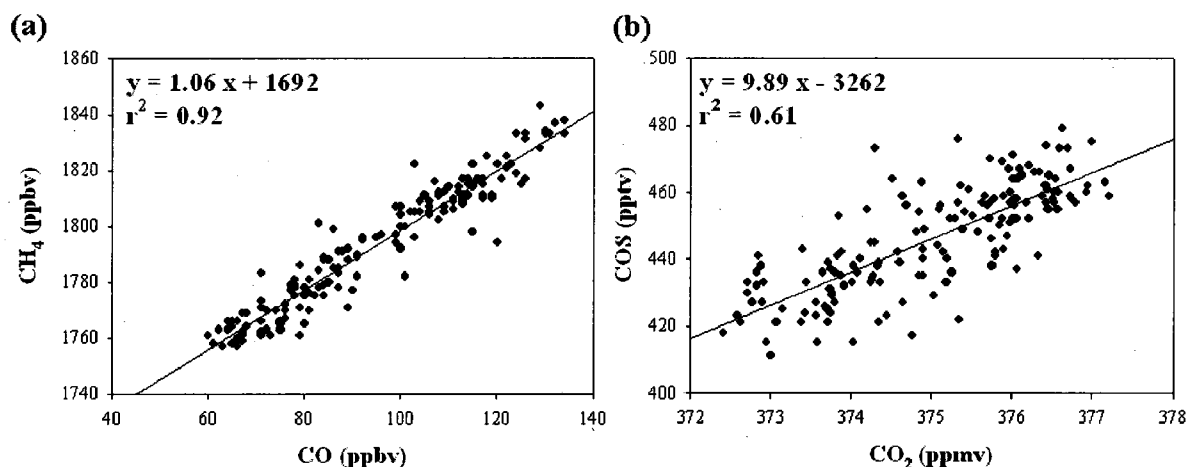
Figure 1.8. Correlations (a) between CO and CH_4, and (b) between CO_2 and COS on flight 13.

Correlations between source indicators and CO/CO_2 were examined further for each region and the results are presented in Table 1.3. The slope of CH_4-CO had a value

of 0.94 in region 1 ($r^2 = 0.84$), 0.97 in region 2 ($r^2 = 0.79$), and 0.68 in region 3 ($r^2 = 0.46$). These values are reasonably close to the slope of 0.84 that was obtained for urban and industrial emissions by Harriss et al. (1994). To corroborate the urban and industrial influence, relationships between CO and a number of anthropogenic tracers were also examined. Compounds that correlated with CO at $r^2 > 0.5$, were $CHCl_3$ and C_2H_2 in region 1, $CHCl_3$, C_2Cl_4, i-C_5H_{12}, C_6H_6, and C_2H_2 in region 2, and $CHCl_3$, C_2Cl_4, i-C_5H_{12}, C_6H_6 and C_2H_2 in region 3. This evidence clearly points to a significant influence of urban, industrial, and combustion sources in all three regions.

Table 1.3. Correlation coefficients, slopes, and standard errors of the slopes for each compound at each region. Regions denoted as reg1, reg2, and reg3 are shown in Figure 1, and outside is the segment of the flight route outside the three regions sampled by flight 13. SBL stands for the boundary layer over the southeastern U.S. observed by flights 6, 7, 10, 12, 16, and 19. Ratios of O_3-CO and CH_4-CO are in unit of ppbv/ppbv, CO-CO_2 in ppbv/ppmv, CH_4-CO_2 in ppmv/ppmv, COS-CO_2 in pptv/ppmv, and all others in pptv/ppbv.

	r^2					Slope					Standard error of the slope				
	Reg1	reg2	reg3	outside	SBL	Reg1	reg2	reg3	outside	SBL	reg1	reg2	reg3	outside	SBL
O_3-CO	0.37	0.03	0.16	0.29	0.59	0.34	0.17	-0.35	0.98	0.26	2.4	0.84	1.6	0.35	0.03
CH_4-CO	0.84	0.79	0.46	0.89	0.65	0.94	0.97	0.68	1.0	0.71	58	22	45	11	0.17
COS-CO	0.42	0.45	0.42	0.59	0.41	-0.45	-0.77	-0.83	-0.59	-0.73	14	5.4	11	2.8	0.07
$CHCl_3$-CO	0.81	0.85	0.60	0.90	0.77	0.07	0.06	0.07	0.06	0.08	0.30	0.11	0.23	0.06	0.01
C_2Cl_4-CO	0.36	0.76	0.64	0.67	0.74	0.15	0.09	0.10	0.08	0.09	0.27	0.06	0.15	0.02	0.01
i-C_5H_{12}-CO	0.38	0.53	0.79	0.40	0.17	0.19	0.23	0.36	0.14	0.82	0.19	0.13	0.16	0.09	0.04
C_6H_6-CO	0.22	0.66	0.73	0.55	0.57	0.13	0.31	0.29	0.25	0.64	0.24	0.15	0.34	0.03	0.03
C_2H_2-CO	0.89	0.77	0.76	0.84	0.87	1.5	1.7	1.5	1.5	2.6	2.8	0.93	1.9	0.04	0.05
CH_4-CO_2	0.08	0.71	0.002	0.86	0.46	-0.01	-0.01	-0.0004	-0.01	-0.005	1.8	0.28	0.48	0.11	0.04
COS-CO_2	0.09	0.63	0.01	0.64	0.83	6.7	12	1.3	8.1	5.3	421	69	117	1.8	0.37
CO-CO_2	0.09	0.65	0.01	0.85	0.36	-6.0	-11	-1.4	-12	-2.7	112	17	30	0.81	0.2

To verify the SBL origin of the polluted air on flight 13, relationships between source indicators and CO in the SBL were calculated and the values of r^2 and correlation

slopes are shown in Table 1.3. The slopes of $CHCl_3$-CO and C_2Cl_4-CO in the SBL were similar to those in the three flight regions, providing support for the SBL as the source region of the air masses encountered on the flight route. Note that slopes of i-C_5H_{10}-CO, C_6H_6-CO and C_2H_2-CO in the SBL were much higher than those observed on flight 13. For example, the slope of i-C_5H_{10}-CO in each region of flight 13 was between 0.19 and 0.36 compared to 0.82 in the SBL. The lifetimes of C_2H_2, C_6H_6, i-C_5H_{12}, C_2Cl_4, and $CHCl_3$ in the SBL were estimated to be 3.5, 2.4, 0.72, 17, and 29 days respectively. Therefore, maximum mixing ratios of short-lived i-C_5H_{10}, C_6H_6, and C_2H_2 in the SBL were much higher than on flight 13 (Table 1.1), which resulted in higher slope values in the SBL.

It is curious that, contrary to the tight CH_4-CO correlation observed on flight 13, CH_4 and CO data from city surveys in the Southeast exhibited a poor correlation ($r^2 = 0.16$), although the slope of CH_4-CO was 0.94, nearly identical to values observed in regions 1 and 2. The slope of CH_4-CO in the SBL sampled by the DC-8 was 0.70, similar to region 3, but with much better correlation ($r^2 = 0.73$) than the city surveys. The difference may be related to the multi-years of data collection for the city survey versus the flight 13 snapshot.

The slope of COS-CO_2 was compared between the SBL and over the North Atlantic. In the SBL CO_2 was correlated with COS at $r^2 = 0.83$, compared to $r^2 = 0.61$ in the flight region. This difference is attributed to mixing of SBL air with ambient air while it meandered over the Southeast for several days and then during transit to the upper troposphere. The COS-CO_2 slope value was 5.3 pptv/ppmv in the SBL, which was almost a factor of two lower than the 9.9 pptv/ppmv value obtained from the flight 13

regions. Mixing ratios of CO_2 in the SBL varied over the range 356 ppmv - 380 ppmv, which was a factor of 5 wider than the range in the flight 13 region of 372 ppmv - 377 ppmv. Similarly, the COS data showed the SBL had a factor of 2 greater variation in mixing ratios than the flight 13 data; 344 pptv - 485 pptv in SBL and 411 pptv - 479 pptv for the flight regions. Wider ranges of CO_2 and COS in the SBL are due to much lower minimum values of two compounds compared to the flight route. The higher minimum values along the flight path is indicative of mixing process with the air mass types identified by our trajectory analysis. However, COS and CO_2 were not well correlated in regions 1 and 3, compared to region 2 and all the flight 13 data together.

A contribution of emissions from the Northeast to the flight regions was checked by utilizing UNH AIRMAP network data in New England. The r^2 values and slopes of the correlations between selected trace gases and CO from ground-based measurements on July 27 - 28 (UTC) at TF (Thompson Farm) and AI (Appledore Island) were very different than those shown here for flight 13 (e.g., the slope of CH_4-CO = 0.28 (r^2 = 0.06) at AI). Therefore, we concluded that emissions from the Northeast were not an important contributor to the elevated trace gas mixing ratios in the upper troposphere over the North Atlantic. This is consistent with our meteorological analysis which showed that the SBL was the likely primary source of pollutants in the upper troposphere

An important feature of the flight 13 dataset was the high degree of correlation between trace gases in the Outside region. In fact, the correlations were close to, or better than, those in regions 1, 2, and 3 (e.g., r^2 = 0.89 for CH_4-CO). This is a surprising result considering the diverse source regions indicated by our trajectory analysis. Typically, there is little or no correlation between most trace gases in air masses not

directly impacted by relatively fresh continental emissions. In this case, it appears that the entire tropospheric column over the North Atlantic during the time period surrounding flight 13 was impacted by North American anthropogenic emissions. This region is in the direct outflow from the eastern U.S. (Parrish et al., 1993), but our analysis seems to suggest that the troposphere over the mid-latitude North Atlantic basin was fumigated with U.S. pollutants in various stages of aging. This is supported by the trajectory-based partitioning of the Outside air source regions, where 44% pointed to an influence of U.S. continental outflow. Apparently, to retain their source relationships, these air masses were not mixed effectively with background marine air. The flight data demonstrate the pervasive impact of U.S. anthropogenic emissions on the mid-latitude troposphere over the North Atlantic.

7. Conclusions

INTEX-NA, one of the components of ICARTT, was conducted over North America and the adjacent North Atlantic to investigate the distribution of trace gases and aerosols associated with emission sources in North America. The vertical distribution of trace gases from DC-8 flight 13 during the campaign had mixing ratios of CH_4 and CO of up to 1843 ppbv and 134 ppbv respectively, and low mixing ratios of CO_2 and COS, reduced to 372.4 ppmv and 411 pptv respectively, in upper troposphere at $8 - 11$ km altitude over the North Atlantic.

The meteorology over the U.S. was identified as an ideal situation for strong outflow for several days prior to flight 13. A stationary front, which evolved from a cold front associated with a Canadian low, existed in the eastern U.S. over the several days before the airborne measurements were conducted. As a result, it induced continuous

convective activities and WCB uplifting of polluted air. In addition, a deep trough over the Midwest facilitated fast southwesterly transport that was sustained for several days prior to flight 13.

The chemical features in the upper troposphere over the North Atlantic were as follows. Urban and industrial tracers such as CH_4 and CO were elevated in the upper troposphere (e.g. 78 ppbv < CO < 135 ppbv) and good linear relationships between the tracers (e.g. r^2 for CH_4 – CO at region 1 = 0.84) showed the impact of urban/industrial emissions to the flight regions. Low mixing ratios of COS and CO_2 (e.g. 372.4 ppmv < CO_2 < 376.6 ppmv) indicated biogenic uptake at the surface in the SBL with subsequent minimal dilution during the transport to the upper troposphere. Backward trajectories and photochemical aging indicated that the SBL was a potential source region for the chemical features. Agreement of the slopes for linear correlations of selected trace gases with a long atmospheric lifetime compared to the transport between SBL and flight regions support the SBL as the primary source region. Overall, meteorological and chemical analyses suggest rapid outflow from the SBL to the upper troposphere over the North Atlantic. In addition, the good linear correlation between urban and industrial tracers in whole flight regions (r^2 for CH_4 – CO = 0.92) and Outside (r^2 for CH_4 – CO = 0.89) suggest that the troposphere over the mid-latitude North Atlantic was influenced significantly with U.S. pollutants in various stages of air mass processing.

II. Chemical transformations of Hg° during Arctic mercury depletion events sampled from the NASA DC-8

1. Introduction

Atmospheric mercury exists in three forms, gaseous elemental mercury (Hg°), reactive gaseous mercury (RGM), and particulate mercury (PHg). Hg° comprises ~95% of total gaseous mercury (TGM = Hg° + RGM) in the atmosphere (Lin and Pehkonen, 1999; Malcolm et al., 2003; Poissant et al., 2005). Atmospheric mercury that enters terrestrial and aquatic ecosystems (Branfireun et al., 2005; Magarelli and Fostier; 2005; Strode et al., 2007) can be subsequently transformed to organic mercury (e.g., methyl mercury) (Branfireun et al., 2005). Organic and inorganic mercury are harmful to humans through food chain uptake; they are thus categorized as toxic compounds by the U.S. Environmental Protection Agency.

Atmospheric mercury depletion events (MDEs) have been observed near the surface in the Arctic springtime. Schroeder et al. (1998) were the first to observe that TGM values, which were 1-2 ng m^{-3} in winter, dropped off to <1 ng m^{-3} after mid-March at a Canadian Arctic site. Strong positive correlation between Hg° and O$_3$ was found in springtime air masses originating from the Arctic (Eneroth et al., 2007; Lu et al., 2001). In addition, MDEs in interstitial air of snowfall, where Hg° concentration was decreased from 5 to 0.4 ng m^{-3}, was found at about 1 m depth in the snowpack at the Kongsvegen Glacier, 10 km south-east from Ny Ålesund, Svalbard (Fain et al., 2006).

Atmospheric mercury depletion in the Arctic has been attributed to meteorological and chemical processes. The strong near-surface inversion layer during winter and early spring creates a vertically isolated thin boundary layer over the Arctic,

and it plays an important role in the occurrence of MDEs by blocking re-supply of atmospheric chemical species such as O_3 and $Hg°$ from the free troposphere (Lehrer et al., 2004). Chemically, the occurrence of MDEs could be closely related with the transformation of $Hg°$ to RGM and PHg as a result of its oxidation by reactive halogen radicals which are likely abundant after polar sunrise (e.g., Cobbett et al., 2007; Lindberg et al., 2002). RGM easily deposits to the surface of aerosols due to its high water solubility (Lin and Pehkonen, 1999) to form PHg. Both RGM and PHg can be removed from the atmosphere relatively quickly due to their high dry deposition velocities (Schroeder and Munthe, 1998).

Box model studies suggest that reactive bromine compounds (e.g., Br and BrO) are much more important for the occurrence of MDEs than chlorine and sulfur compounds (Ariya et al., 2004; Calvert and Lindberg, 2003; Goodsite et al., 2004; Xie et al., 2008). It was speculated that highly reactive bromines are derived mainly from the surface sea ice and less reactive bromines, such as HBr, are from sea salt aerosols (Lehrer et al., 2004). As a result of mercury oxidation, a few studies suggested that the most abundant RGM chemical compounds would be HgO, $HgBr_2$, and BrHgOBr formed by reaction of $Hg°$ with bromine radical (Calvert and Lindberg, 2003; Xie et al., 2008).

The Arctic Research of the Composition of the Troposphere from Aircraft and Satellites (ARCTAS) field campaign, carried out by the National Aeronautics and Space Administration Tropospheric Chemistry Program, was conducted over 3 weeks each in April and July 2008 with focus on impacts on Arctic atmospheric composition from long-range transport of pollution, boreal forest fires, aerosol radiative forcing, and chemical processing (Jacob et al., 2010). Here, we aimed to understand the chemical mechanisms

driving the occurrence of MDEs in the Arctic spring using box model results based on extensive measurements of mercury and other chemical compounds from the NASA DC-8 aircraft during the 2008 April deployment.

2. Methods

2.1 ARCTAS Measurement Data

Hg° was measured with a time resolution of ~2 minutes by the University of New Hampshire cold vapor atomic fluorescence spectrometer during the ARCTAS field campaign. We utilized a modified Tekran 24537A as described by Talbot et al. (2008). The limit of detection (LOD) of the instrument was ~0.2 ng m^{-3} (~22 ppqv). The internal pressure of the instrument was maintained during the analysis stage at 1100 hPa. In-flight zeroing and standard additions were conducted on all flights.

Ozone was measured at 1 Hz using the chemiluminescence technique as described in Ridley et al. (1992). The University of California at Irvine sampled using stainless steel passivated canisters to determine more than 75 gases including nonmethane hydrocarbons, halocarbons, alkyl nitrates and sulfur compounds. A comprehensive description of the sampling and analytical techniques can be found in Colman et al. (2001). The Georgia Institute of Technology chemical ionization mass spectrometer was used to measure BrO and Br_2 every 30 seconds using the reagent SF_6^-. A detailed explanation of the technique is given in Neuman et al. (2010). The University of New Hampshire group collected aerosols on Teflon filters with subsequent analysis for soluble ions by ion chromatography (Dibb et al., 2003). This group also sampled water-soluble gases using the mist chamber technique (Scheuer et al., 2003).
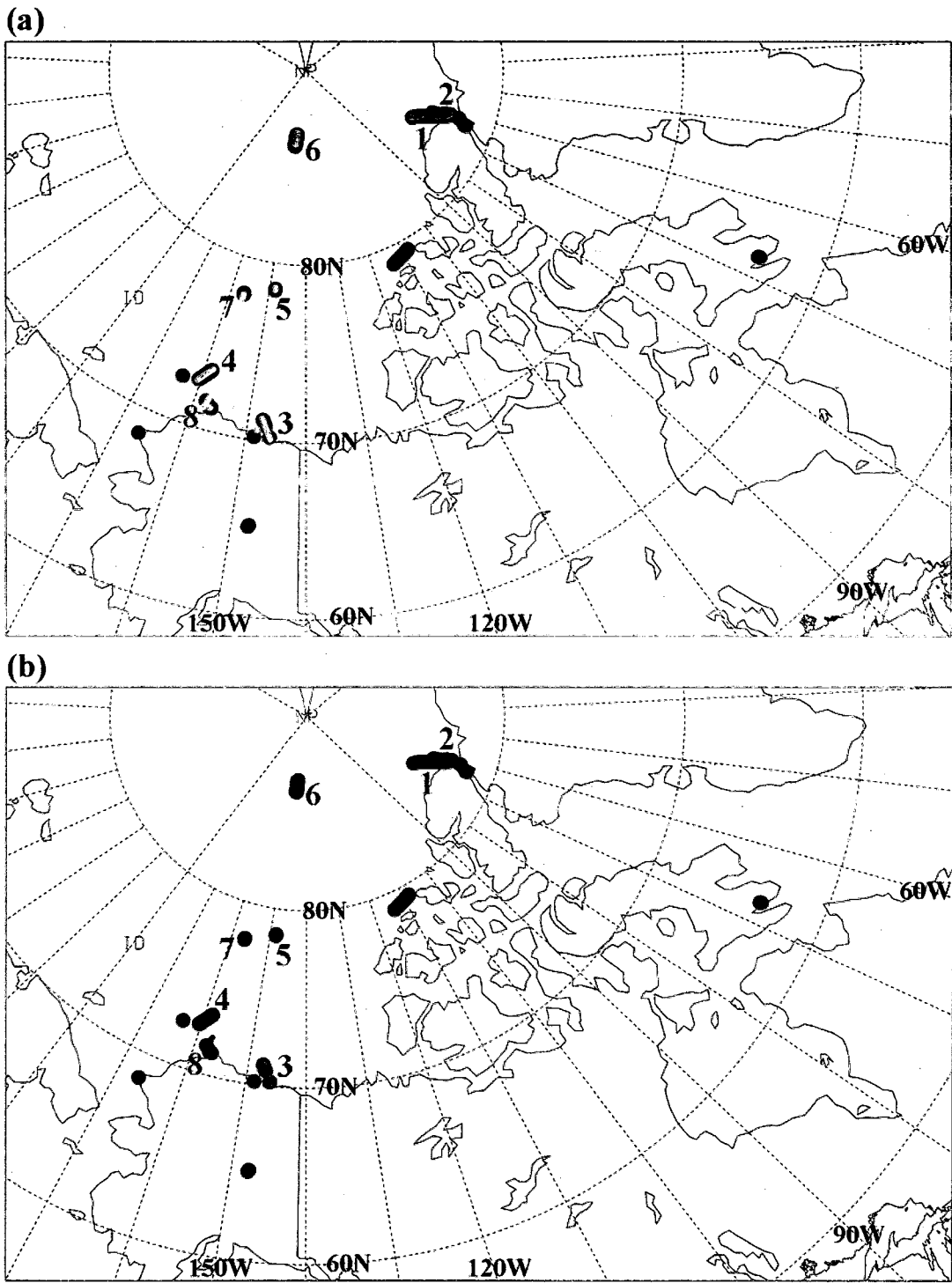
Figure 2.1. Spatial distribution of Hg° < 50 ppqv (yellow dots) and high Br₂ > 2pptv (blue dots) (a) and O₃ <10 ppbv (pink dots) and high Br₂ > 2pptv (light blue dots) (b) below 5 km altitude

There were 14 MDE cases below 5 km altitude in which the Hg° mixing ratio was depleted to <50 ppqv (1ng m^{-3} = 112 ppqv). The spatial distribution of mixing ratios of Hg° <50 ppqv, O_3 <10 ppbv and Br_2 > 2 pptv as observed during ARCTAS is displayed in Figure 2.1. Eight cases exhibited generally distinct features of MDEs, i.e., the concurrence of high Br_2, low O_3, and low Hg° mixing ratios (Table 2.1), and these will be the focus of this study. It should be noted though that the mixing ratios of O_3 right at the onset and ending of the MDEs were mostly >10 ppbv. Case 6 showed O_3 values during the MDE that were close to 10 ppbv. Six cases did not show a concurrence of high Br_2, low O_3, and low Hg°. The comparison between these two types of cases should be interesting, but unfortunately we could not study the six non-concurrence cases due to a lack of sufficient measurement data. Perhaps these cases reflected the later stages of a MDE with the mixing of MDE air with other air masses.

Table 2.1. MDE cases selected for study.

case	day	altitude (km)	O_3 (ppbv)	Hg° (ppqv) (below LOD except several points mentioned below)	Br_2 (pptv)	state of sea ice
1	4/8/2008	0.1 – 0.21	0.38 – 5.6	one - 22	3.25 - 5.8	Very fractured surface no open water
2	4/9/2008	0.11	5.0 – 13.5	two - 21	1.3 - 2.7	Very fractured surface no open water
3	4/16/2008	0.08 – 0.8	1.8 – 34.5	one - 39	0.2 - 3.2	Irregular small patches of open water
4	4/16/2008	0.09 – 0.65	3.3 – 43	25, 34, and 37	0.45 - 5.4	Irregular small patches of open water
5	4/17/2008	0.1	0.8 – 30		1.5 - 6.15	Fine cracks no open water
6	4/17/2008	0.1 – 0.8	10.7 – 34.5	18, 24, and 62	1.05 - 6.85	No record
7	4/17/2008	0.09	9.0 - 26.5		0.75 - 2.75	No record
8	4/17/2008	0.07 – 0.22	0.9 – 42	28 - 61	0.35 - 1.75	No record

(a) Case 1   (b) Case 2

(c) Case 3   (d) Case 4

(e) Case 5   (f) Case 6

(g) Case 7   (h) Case 8
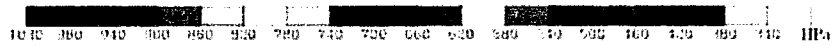
Figure 2.2. Five-day backward trajectories for each MDE case. The color bar is pressure level and the unit is hPa.

2.2 Trajectories

Kinematic backward trajectories were provided at one minute time steps throughout ARCTAS by Florida State University (http://www-air.larc.nasa.gov/cgi-bin/arcstat-c). The three-dimensional wind components were utilized from the Weather Research and Forecasting (WRF) Model hourly output at 45 km resolution to calculate the backward trajectories (Fuelberg et al., 1996, 2000; Martin et al., 2003). For each MDE case, the corresponding five-day backward trajectories are shown in Figure 2.2. The trajectories allowed comparison of air mass origins both outside and inside the MDE areas.

2.3 Box Model Description

Mercury gas phase reactions occur mainly with O_3, H_2O_2, halides such as Br_2, Cl_2, and radicals OH, Br, Cl, and I (Table 2.2). The multitude of mercury chemical reactions and their rates are not clearly established yet. Differing results have been published on the products of some mercury chemical reactions. For example, the reaction between $Hg°$ and OH apparently has two different products - HgOH and HgO (Goodsite et al., 2004; Sommar et al., 2001; Pal and Ariya, 2004a). Furthermore, values of the rate constant for many $Hg°$ reactions vary considerably. There is large uncertainty in the rate constant of the reaction between $Hg°$ and O_3, ranging from 3.0×10^{-20} cm^3 molecule^{-1} s^{-1} at 293 K (Hall, 1995) to 7.5×10^{-19} cm^3 molecule^{-1} s^{-1} at 298 K (Pal and Ariya, 2004b). This study utilized the rate constant from Pal and Ariya (2004) because it was only temperature dependent rate constant. Note that this rate constant is still under discussion (Castro et al., 2009). Rate constants for $Hg°$ reactions with halogen radicals that have

Table 2.2. Hg° gaseous reactions in the model.

	reactant	Reactions	Rate constant/ equilibrium constant	Reference
Mercury Gaseous reaction	$Hg^0 + O_3$	$Hg^0_{(g)} + O_3 \rightarrow HgO_{(s,g)} + O_{2(g)}$ (~ 1atm N_2)	8.43×10^{-17} exp (-1407/T) cm³ molecule⁻¹ s⁻¹	Pal and Ariya (2004(b))
	$Hg^0 + OH$	$Hg^0_{(g)} + OH \leftrightarrow HgOH_{(g)}$ (1atm N_2)	→ $3.2\times10^{-13}(T/298)^{-3.06}$ cm³ molecule⁻¹ s⁻¹ ← 2.7×10^9 exp (-4061/T) s⁻¹	Goodsite et al. (2004)
		$Hg^0_{(g)} + OH\cdot \rightarrow HgOH\cdot + O_2 \rightarrow HgO + HO_2\cdot$	3.55×10^{-14} exp (294/T) cm³ molecule⁻¹ s⁻¹	Pal and Ariya (2004(a))
	$Hg^0 + H_2O_2$	$Hg^0_{(g)} + H_2O_2 \rightarrow Hg(OH)_{2(g,s)}$	8.5×10^{-19} molecule⁻¹ s⁻¹	Tokos et al. (1998)
	$Hg^0 + Br$	$Hg^0_{(g)} + Br_{(g)} \leftrightarrow HgBr_{(g)} \rightarrow HgBr_{2(g)}$ (1atm N_2)	→ $1.1\times10^{-12}(T/298)^{-2.37}$ cm³ molecule⁻¹ s⁻¹ → $2.5\times10^{-10}(T/298)^{-0.57}$ cm³ molecule⁻¹ s⁻¹ ← 1.2×10^{10} exp (-8357/T) s⁻¹	Goodsite et al. (2004)
		$Hg^0_{(g)} + Br_{(g)} \rightarrow HgBr_{(g)}$ (1atm (0.8N_2+0.2O_2))	1.01×10^{-12} exp (209.03/T) cm³ molecule⁻¹ s⁻¹	Khalizov et al, (2003)
		$Hg^0_{(g)} + Br_{(g)} + M \rightarrow HgBr_{(g)} + M$	$1.46\times10^{-32}\times(T/298)^{-1.86}$ cm⁶ molecule⁻² s⁻¹ (1atm N_2 = 2.9×10^{19} molecule cm³)	Donohoue et al. (2006)
	$Hg^0 + Br_2$	$Hg^0_{(g)} + Br_{2(g)} \rightarrow HgBr_{2(g)}$ (750 Torr air or N_2)	$(0.9\pm0.2)\times10^{-16}$ cm³ molecule⁻¹ s⁻¹ (at 298K) $(2.74)\times10^{-31}$ cm³ molecule⁻¹ s⁻¹ (at 298K)	Balabanov et al. (2005)
	$HgBr + Br$	$HgBr_{(g)} + Br_{(g)} \rightarrow Hg_{(g)} + Br_{2(g)}$	3.89×10^{-11} cm³ molecule⁻¹ s⁻¹ (at 298K)	Balabanov et al. (2005)
		$HgBr_{(g)} + Br_{(g)} \rightarrow HgBr_{(g)} + Br_{(g)}$	3.97×10^{-11} cm³ molecule⁻¹ s⁻¹ (at 298K)	Balabanov et al. (2005)
	$Hg^0 + I$	$Hg^0_{(g)} + I_{(g)} \leftrightarrow HgI_{(g)}$ (1atm N_2)	→ $4.0\times10^{-13}(T/298)^{-2.38}$ cm³ molecule⁻¹ s⁻¹ ← 3.0×10^9 exp (-3742/T) s⁻¹	Goodsite et al. (2004)
	$Hg^0 + Cl_2$	$Hg^0_{(g)} + Cl_{2(g)} \rightarrow HgCl_{2(g)}$ (750 Torr air or N_2)	$(2.6\pm0.2)\times10^{-18}$ cm³ molecule⁻¹ s⁻¹ (at 298K)	Ariya et al. (2002)
	$Hg^0 + Cl$	$Hg^0_{(g)} + Cl_{(g)} \rightarrow HgCl_{(g)}$ (1atm (0.8N_2+0.2O_2))	1.38×10^{-12} exp (208.02/T) cm³ molecule⁻¹ s⁻¹	Khalizov et al. (2003)
		$Hg^0_{(g)} + Cl_{(g)} + M \rightarrow HgCl_{(g)} + M$	2.2×10^{-32}exp(680*(1/T-1/298))cm⁶molecule⁻²s⁻¹ (1atm N_2 = 2.9×10^{19} molecule cm³)	Donohoue et al. (2005)

Table 2.3. Gaseous halogen chemistry in the model.

	Reactions	Rate constant/ equilibrium constant	Reference
Bromine chemistry	$Br_2 \rightarrow Br + Br$		ARCTAS measurement
	$Br + O_3 \rightarrow BrO + O_2$	$1.7 \times 10^{-11} \exp(-800/T)$ cm³ molecule⁻¹ s⁻¹	Sander et al.(2006)
	$BrO \rightarrow Br + O$		ARCTAS measurement
	$2BrO \rightarrow 2Br + O_2$	$2.4 \times 10^{-12} \exp(40/T)$ cm³ molecule⁻¹ s⁻¹	Sander et al.(2006)
	$2BrO \rightarrow Br_2 + O_2$	$2.8 \times 10^{-14} \exp(860/T)$ cm³ molecule⁻¹ s⁻¹	Sander et al.(2006)
	$BrO + ClO \rightarrow Br + OClO$	$9.5 \times 10^{-13} \exp(550/T)$ cm³ molecule⁻¹ s⁻¹	Sander et al.(2006)
	$BrO + ClO \rightarrow Br + ClOO$	$2.3 \times 10^{-12} \exp(260/T)$ cm³ molecule⁻¹ s⁻¹	Sander et al.(2006)
	$BrO + ClO \rightarrow BrCl + O_2$	$4.1 \times 10^{-13} \exp(290/T)$ cm³ molecule⁻¹ s⁻¹	Sander et al.(2006)
	$BrO + HO_2 \rightarrow HOBr + O_2$	$4.5 \times 10^{-12} \exp(500/T)$ cm³ molecule⁻¹ s⁻¹	Atkinson et al. (2007)
	$BrO + NO \rightarrow NO_2 + Br$	$8.8 \times 10^{-12} \exp(260/T)$ cm³ molecule⁻¹ s⁻¹	Sander et al.(2006)
	$HOBr \rightarrow Br + OH$		ARCTAS measurement
	$Br + HO_2 \rightarrow HBr + O_2$	$4.8 \times 10^{-12} \exp(-310/T)$ cm³ molecule⁻¹ s⁻¹	Sander et al.(2006)
	$Br + H_2CO \rightarrow HBr + HCO$	$1.7 \times 10^{-11} \exp(-800/T)$ cm³ molecule⁻¹ s⁻¹	Sander et al.(2006)
	$HBr + OH \rightarrow Br + H_2O$	$5.5 \times 10^{-12} \exp(200/T)$ cm³ molecule⁻¹ s⁻¹	Sander et al.(2006)
	$CH_3Br + OH \rightarrow CH_2Br + H_2O$	$2.35 \times 10^{-12} \exp(-1300/T)$ cm³ molecule⁻¹ s⁻¹	Sander et al. (2006)
	$Br_2 + OH \rightarrow HOBr + Br$	$2.1 \times 10^{-11} \exp(240/T)$ cm³ molecule⁻¹ s⁻¹	Sander et al. (2006)
	$Br + C_2H_2 (+M) \rightarrow BrC_2H_2 (+M)$	$6.35 \times 10^{-15} \exp(440/T)$ cm³ molecule⁻¹ s⁻¹	Atkinson et al. (2006)
	$Br + NO_2 + M \rightarrow BrNO_2 + M$	$k_0=4.2 \times 10^{-31}$, $k_\infty=2.7 \times 10^{-11}$, n=2.4, m=0	Sander et al.(2006)
	$BrO + NO_2 + M \rightarrow BrONO_2 + M$	$k_0=5.2 \times 10^{-31}$, $k_\infty=6.9 \times 10^{-12}$, n=3.2, m=2.9	Sander et al. (2006)
	$BrONO_2 \rightarrow BrO + NO_2$		ARCTAS measurement
	$BrONO_2 \rightarrow Br + NO_3$		ARCTAS measurement
	$BrCl \rightarrow Br + Cl$		ARCTAS measurement
	$Br + CH_3CHO \rightarrow HBr + CH_3CO$	$1.8 \times 10^{-11} \exp(-460/T)$ cm³ molecule⁻¹ s⁻¹	Atkinson et al. (2006)
	$BrO + O \rightarrow Br + O_2$	$1.9 \times 10^{-11} \exp(230/T)$ cm³ molecule⁻¹ s⁻¹	Sander et al. (2006)
	$HBr + O \rightarrow OH + Br$	$5.8 \times 10^{-12} \exp(-1500/T)$ cm³ molecule⁻¹ s⁻¹	Sander et al. (2006)
	$HOBr + O \rightarrow OH + BrO$	$1.2 \times 10^{-10} \exp(-430/T)$ cm³ molecule⁻¹ s⁻¹	Sander et al. (2006)
	$BrONO_2 + O \rightarrow NO_3 + BrO$	$1.9 \times 10^{-11} \exp(215/T)$ cm³ molecule⁻¹ s⁻¹	Sander et al. (2006)
	$BrNO_2 \rightarrow 0.5(BrO+NO+NO2+Br)$	7.128×10^{-3} s⁻¹	TUV model based on Sander et al. (2006)

	Reactions	Rate constant/ equilibrium constant	Reference
Chlorine chemistry	$Cl_2 \rightarrow Cl + Cl$		ARCTAS measurement
	$Cl + O_3 \rightarrow ClO + O_2$	$2.3 \times 10^{-11} \exp(-200/T)$ cm^3 molecule^{-1} s^{-1}	Sander et al.(2006)
	$ClO \rightarrow Cl + O$	3×10^{-5} s^{-1}	Simpson et al. (2007)
	$2ClO \rightarrow Cl_2 + O_2$	$1 \times 10^{-12} \exp(-1590/T)$ cm^3 molecule^{-1} s^{-1}	Sander et al.(2006)/Atkinson et al.(2007)
	$2ClO \rightarrow ClOO + Cl$	$3 \times 10^{-11} \exp(-2450/T)$ cm^3 molecule^{-1} s^{-1}	Sander et al.(2006)/Atkinson et al.(2007)
	$2ClO \rightarrow OClO + Cl$	$3.5 \times 10^{-13} \exp(-1370/T)$ cm^3 molecule^{-1} s^{-1}	Sander et al.(2006)/Atkinson et al.(2007)
	$ClO + HO_2 \rightarrow HOCl + O_2$	$2.7 \times 10^{-12} \exp(220/T)$ cm^3 molecule^{-1} s^{-1}	Sander et al.(2006)
	$ClO + NO \rightarrow Cl + NO_2$	$6.4 \times 10^{-12} \exp(290/T)$ cm^3 molecule^{-1} s^{-1}	Sander et al.(2006)
	$HOCl \rightarrow Cl + OH$	0.0001118 s^{-1}	TUV model based on Sander et al. (2006)
	$Cl + HO_2 \rightarrow HCl + O_2$	$1.8 \times 10^{-11} \exp(170/T)$ cm^3 molecule^{-1} s^{-1}	Sander et al.(2006)
	$Cl + HO_2 \rightarrow OH + ClO$	$4.1 \times 10^{-11} \exp(-450/T)$ cm^3 molecule^{-1} s^{-1}	Sander et al.(2006)
	$Cl + H_2CO \rightarrow HCl + CHO$	$8.1 \times 10^{-11} \exp(-30/T)$ cm^3 molecule^{-1} s^{-1}	Sander et al.(2006)
	$HCl + OH \rightarrow Cl + H_2O$	$2.6 \times 10^{-12} \exp(-350/T)$ cm^3 molecule^{-1} s^{-1}	Sander et al.(2006)
	$OH + ClO \rightarrow HCl + O_2$	$6 \times 10^{-13} \exp(230/T)$ cm^3 molecule^{-1} s^{-1}	Sander et al. (2006)
	$OH + ClO \rightarrow Cl + HO_2$	$7.4 \times 10^{-12} \exp(270/T)$ cm^3 molecule^{-1} s^{-1}	Sander et al. (2006)
	$Cl + CH_4 \rightarrow HCl + CH_3$	$7.3 \times 10^{-12} \exp(-1280/T)$ cm^3 molecule^{-1} s^{-1}	Sander et al. (2006)
	$Cl + H_2 \rightarrow HCl + H$	$3.05 \times 10^{-11} \exp(-2270/T)$ cm^3 molecule^{-1} s^{-1}	Sander et al. (2006)
	$Cl + C_2H_6 \rightarrow HCl + C_2H_5$	$7.2 \times 10^{-11} \exp(-70/T)$ cm^3 molecule^{-1} s^{-1}	Sander et al. (2006)
	$Cl + C_3H_8 \rightarrow HCl + C_3H_7$	$7.85 \times 10^{-11} \exp(-80/T)$ cm^3 molecule^{-1} s^{-1}	Sander et al. (2006)
	$Cl + H_2O_2 \rightarrow HCl + HO_2$	$1.1 \times 10^{-11} \exp(-980/T)$ cm^3 molecule^{-1} s^{-1}	Sander et al. (2006)
	$Cl + ClOO \rightarrow Cl_2 + O_2$	2.3×10^{-10} cm^3 molecule^{-1} s^{-1}	Sander et al. (2006)
	$Cl + ClOO \rightarrow 2ClO$	1.2×10^{-11} cm^3 molecule^{-1} s^{-1}	Sander et al. (2006)
	$HOCl + OH \rightarrow ClO + H2O$	$3 \times 10^{-12} \exp(-500/T)$ cm^3 molecule^{-1} s^{-1}	Sander et al. (2006)
	$Cl + O_2 + M \rightarrow ClOO + M$	$k_0 = 2.2 \times 10^{-33}$, $k_\infty = 1.8 \times 10^{-10}$, n=3.1, m=0	Sander et al. (2006)
	$Cl + NO_2 + M \rightarrow ClONO + M$	$k_0 = 1.3 \times 10^{-30}$, $k_\infty = 1. \times 10^{-10}$, n=2, m=1	Sander et al. (2006)
	$ClO + NO_2 + M \rightarrow ClONO_2 + M$	$k_0 = 1.8 \times 10^{-31}$, $k_\infty = 1.5 \times 10^{-11}$, n=3.4, m=1.9	Sander et al. (2006)
	$ClONO \rightarrow Cl + NO_2$	1.601×10^{-3} s^{-1}	TUV model based on Sander et al. (2006)
	$ClONO_2 \rightarrow Cl + NO_3$		ARCTAS measurement
	$ClONO_2 \rightarrow ClO + NO_2$		ARCTAS measurement
	$OClO \rightarrow ClO + O$	0.1035 s^{-1}	TUV model based on Sander et al. (2006)
	$Cl + C_2H_2 + M \rightarrow C_2H_2Cl + M$	$k_0 = 6.1 \times 10^{-30}$, $k_\infty = 2. \times 10^{-10}$, n=3, m=0	Atkinson et al. (2006)
	$Cl + n\text{-}C_4H_{10} \rightarrow HCl + C_4H_9$	2.05×10^{-10} cm^3 molecule^{-1} s^{-1}	Atkinson et al. (2006)
	$Cl + CH_3CHO \rightarrow HCl + CH_3CO$	8×10^{-11} cm^3 molecule^{-1} s^{-1}	Atkinson et al. (2006)

Reactions	Rate constant	Reference
$Cl + CH_3OH \rightarrow HCl + CH_2OH$	5.5×10^{-11} cm^3 molecule^{-1} s^{-1}	Atkinson et al. (2006)
$Cl + C_2H_5OH \rightarrow$ product	8.6×10^{-11} exp (45/T) cm^3 molecule^{-1} s^{-1}	Atkinson et al. (2006)
$O + ClO \rightarrow Cl + O_2$	2.8×10^{-11} exp (85/T) cm^3 molecule^{-1} s^{-1}	Sander et al. (2006)
$O + OClO \rightarrow ClO + O_2$	2.4×10^{-12} exp (-960/T) cm^3 molecule^{-1} s^{-1}	Sander et al. (2006)
$O + OClO + M \rightarrow ClO_3 + M$	$k_0=2.9 \times 10^{-31}$, $k_\infty=8.3 \times 10^{-12}$, n=3.1, m=0	Sander et al. (2006)
$O + HCl \rightarrow OH + Cl$	1.0×10^{-11} exp (-3300/T) cm^3 molecule^{-1} s^{-1}	Sander et al. (2006)
$O + HOCl \rightarrow OH + ClO$	1.7×10^{-13} cm^3 molecule^{-1} s^{-1}	Sander et al. (2006)
$O + ClONO_2 \rightarrow$ products	2.9×10^{-12} exp (-800/T) cm^3 molecule^{-1} s^{-1}	Sander et al. (2006)
$O_3 + OClO \rightarrow$ products	2.1×10^{-12} exp (-4700/T) cm^3 molecule^{-1} s^{-1}	Sander et al. (2006)
$ClOO + M \rightarrow Cl + O_2 + M$	2.8×10^{-10}/exp(1820/T) × [N$_2$]	Atkinson et al. (2007)

	Reactions	Rate constant/ equilibrium constant	Reference
Iodine chemistry	$I + O_3 \rightarrow IO + O_2$	2.3×10^{-11} exp (-870/T) cm^3 molecule^{-1} s^{-1}	Sander et al.(2006)
	$IO \rightarrow I + O$	0.2 s^{-1}	Simpson et al. (2007)
	$2IO \rightarrow$ product	1.5×10^{-11} exp (500/T) cm^3 molecule^{-1} s^{-1}	Sander et al.(2006)
	$IO + ClO \rightarrow$ product	5.1×10^{-12} exp (280/T) cm^3 molecule^{-1} s^{-1}	Sander et al.(2006)
	$IO + BrO \rightarrow$ product	1.5×10^{-11} exp (510/T) cm^3 molecule^{-1} s^{-1}	Atkinson et al. (2007)
	$IO + HO_2 \rightarrow HOI + O_2$	1.4×10^{-11} exp (540/T) cm^3 molecule^{-1} s^{-1}	Atkinson et al. (2007)
	$IO + NO \rightarrow I + NO_2$	9.1×10^{-12} exp (240/T) cm^3 molecule^{-1} s^{-1}	Sander et al.(2006)
	$I_2 \rightarrow I + I$	0.12 s^{-1}	Saiz-Lopez et al. (2004)
	$I + HO_2 \rightarrow HI + O_2$	1.5×10^{-11} exp (-1090/T) cm^3 molecule^{-1} s^{-1}	Sander et al.(2006)/Atkinson et al.(2007)
	$HI + OH \rightarrow I + H_2O$	1.6×10^{-11} exp (440/T) cm^3 molecule^{-1} s^{-1}	Atkinson et al. (2007)

Table 2.4. Ozone chemistry in the model.

	Reactions	Rate constant/ equilibrium constant	Reference
Ozone Chemistry	$O_3 \rightarrow O(D^1) + O_2$		ARCTAS measurement
	$NO_2 \rightarrow O(^3P) + NO$		ARCTAS measurement
	$CH_3CHO \rightarrow CH_3 + HCO$		ARCTAS measurement
	$HCHO \rightarrow H + HCO$		ARCTAS measurement
	$HCHO \rightarrow H_2 + CO$		ARCTAS measurement
	$CH_3OOH \rightarrow CH_3O + OH$		ARCTAS measurement
	$N_2O_5 \rightarrow NO_2 + NO_3$		ARCTAS measurement
	$H_2O_2 \rightarrow 2OH$		ARCTAS measurement
	$NO_3 + NO_2 \rightarrow N_2O_5$	$k_0 = 2.0 \times 10^{-30}$, $k_\infty = 1.4 \times 10^{-12}$, $n = 4.4$, $m = 0.7$	Sander et al. (2006)
	$O_3 + NO \rightarrow NO_2 + O_2$	$1.4 \times 10^{-12}/\exp(1310/T)$ cm^3 molecule^{-1} s^{-1}	Atkinson et al. (2004)
	$NO_2 + O_3 \rightarrow NO_3 + O_2$	$1.4 \times 10^{-13}/\exp(2470/T)$ cm^3 molecule^{-1} s^{-1}	Atkinson et al. (2004)
	$NO_3 + NO \rightarrow 2NO_2$	$1.5 \times 10^{-11} \exp(170/T)$ cm^3 molecule^{-1} s^{-1}	Sander et al. (2006)
	$O(1D) + H_2O \rightarrow 2OH$	$1.63 \times 10^{-10} \exp(60/T)$ cm^3 molecule^{-1} s^{-1}	Sander et al. (2006)
	$O(1D) + N_2 \rightarrow O(^3P) + N_2$	$2.15 \times 10^{-11} \exp(110/T)$ cm^3 molecule^{-1} s^{-1}	Sander et al. (2006)
	$HO_2 + NO \rightarrow OH + NO_2$	$3.5 \times 10^{-12} \exp(250/T)$ cm^3 molecule^{-1} s^{-1}	Sander et al. (2006)
	$OH + CH_4 \rightarrow H_2O + CH_3$	$1.85 \times 10^{-12}/\exp(1690/T)$ cm^3 molecule^{-1} s^{-1}	Atkinson et al. (2006)
	$CH_3 + O_2 \rightarrow CH_3O_2$	$k_0 = 1.0 \times 10^{-30}$, $k_\infty = 1.8 \times 10^{-12}$, $n = 3.3$, $m = -1.1$	Atkinson et al. (2006)
	$OH + HCHO \rightarrow H_2O + HCO$	$5.4 \times 10^{-12} \exp(135/T)$ cm^3 molecule^{-1} s^{-1}	Atkinson et al. (2006)
	$OH + CH_3OOH \rightarrow CH_3O_2 + H_2O$	$3.8 \times 10^{-12} \exp(200/T)$ cm^3 molecule^{-1} s^{-1}	Sander et al. (2006)
	$OH + CO \rightarrow H + CO_2$	$k_0 = 1.5 \times 10^{-13}$, $k_\infty = 2.1 \times 10^{9}$, $n = -0.6$, $m = -6.1$	Sander et al. (2006)
	$OH + NO \rightarrow HONO$	$k_0 = 7.0 \times 10^{-31}$, $k_\infty = 3.6 \times 10^{-11}$, $n = 2.6$, $m = -0.1$	Sander et al. (2006)
	$OH + NO_2 \rightarrow HONO_2$	$k_0 = 1.8 \times 10^{-30}$, $k_\infty = 2.8 \times 10^{-11}$, $n = 3.0$, $m = 0.$	Sander et al. (2006)
	$OH + HO_2 \rightarrow H_2O + O_2$	$4.8 \times 10^{-11} \exp(250/T)$ cm^3 molecule^{-1} s^{-1}	Atkinson et al. (2004)
	$OH + O_3 \rightarrow HO_2 + O_2$	$1.7 \times 10^{-12}/\exp(940/T)$ cm^3 molecule^{-1} s^{-1}	Atkinson et al. (2004)
	$2HO_2 + N_2 \rightarrow H_2O_2 + O_2 + N_2$	$1.9 \times 10^{-33} \exp(980/T)$ cm^6 molecule^{-2} s^{-1}	Atkinson et al. (2004)
	$HO_2 + O_3 \rightarrow OH + 2O_2$	$2.03 \times 10^{-16} \exp(693/T) \times (T/300)^{4.57}$ cm^3 molecule^{-1} s^{-1}	Atkinson et al. (2004)
	$HO_2 + CH_3O_2 \rightarrow CH_3OOH + O_2$	$3.8 \times 10^{-13} \exp(780/T)$ cm^3 molecule^{-1} s^{-1}	Atkinson et al. (2006)
	$CH_3O_2 + NO \rightarrow CH_3O + NO_2$	$2.3 \times 10^{-12} \exp(360/T)$ cm^3 molecule^{-1} s^{-1}	Atkinson et al. (2006)
	$O(^1D) + O_2 \rightarrow O(^3P) + O_2$	$3.3 \times 10^{-11} \exp(55/T)$ cm^3 molecule^{-1} s^{-1}	Sander et al. (2006)
	$O(^1D) + O_3 \rightarrow 2O(^3P) + O_2$	1.2×10^{-10} cm^3 molecule^{-1} s^{-1}	Sander et al. (2006)
	$O(^3P) + O_2 + N_2 \rightarrow O_3 + N_2$	$5.6 \times 10^{-34} /(T/300)^{2.6}$ cm^6 molecule^{-2} s^{-1}	Atkinson et al. (2004)
	$OH + C_2H_2 \rightarrow C_2H_2OH$	$k_0 = 5.5 \times 10^{-30}$, $k_\infty = 8.3 \times 10^{-13}$, $n = 0$, $m = -2$	Sander et al. (2006)
	$OH + C_2H_6 \rightarrow H_2O + C_2H_5$	$8.7 \times 10^{-12}/\exp(1070/T)$ cm^3 molecule^{-1} s^{-1}	Sander et al. (2006)

$OH + C_3H_8 \rightarrow$ product	$8.7 \times 10^{-12}/\exp(615/T)$ cm^3 molecule^{-1} s^{-1}	Sander et al. (2006)
$O_3 + C_2H_2 \rightarrow$ product	$1 \times 10^{-14}/\exp(4100/T)$ cm^3 molecule^{-1} s^{-1}	Sander et al. (2006)

been reported in literature also vary greatly. The rate constant of Hg° with Cl radical at 298 K ranges from 6.38×10^{-13} cm^3 molecule^{-1} s^{-1} (Donohoue et al., 2005) to 1.0×10^{-11} cm^3 molecule^{-1} s^{-1} (Ariya et al., 2002). Rate constants of Hg° reaction with Br vary from 4.23×10^{-13} cm^3 molecule^{-1} s^{-1} (Donohoue et al., 2006) to 3.2×10^{-12} cm^3 molecule^{-1} s^{-1} (Ariya et al., 2002). Finally, BrO is recognized as an important oxidant in Arctic mercury chemistry (Goodsite et al., 2004), but the rate constant values vary from 10^{-13} to 10^{-15} cm^3 molecule^{-1} s^{-1} for its reaction with Hg° at a temperature of 298 K (Raofie and Ariya, 2003). We did not include this reaction in most cases except in section 4.2 where the possible role of this reaction in the occurrence of MDEs was studied. Overall, our box model includes 28, 43, and 10 reactions for bromine, chlorine, and iodine chemistry respectively. In addition, there are 10 mercury gas phase reactions and 35 for O$_3$ chemistry (Tables 2.2 – 2.4).

The Kinetic PreProcessor (KPP) version 2.1 is the basic model framework (Sandu and Sander, 2006), and it has been utilized to study mercury chemistry previously (Hedgecock et al., 2005; Pan and Carmichael, 2005). The structure solves ordinary differential equations, and we used a second order Rosenbrock method (Verwer et al., 1999). Ideal (i.e., theoretical) experiments were used to clearly identify how environmental factors (e.g., photolysis) influenced Hg° or O$_3$ depletion. As shown in Section 3, backward trajectories for each case indicated that air masses were principally transported over short distances in the 24 hours prior to airborne measurements. During the MDEs, cold CN concentrations were mainly <500 cm^{-3}, which indicated low aerosol concentrations in the atmosphere, and air temperature averaged 255±5 K which was cold enough to freeze the ocean surface. Moreover, the water vapor mixing ratios were <1700

ppmv during MDEs period, which were low values, for example, compared to 4500-11700 ppmv in marine boundary layer of northeastern Pacific near Anchorage, Alaska

Table 2.5. Initial conditions used in model runs.

Chemical compounds	Mixing ratios / concentrations
NO	10 pptv
NO_2	0 pptv
H_2O_2	152 pptv
HCHO	122 pptv
OH	$360000 \ cm^{-3}$
CH_3OH	608 pptv
CH_3CHO	121 pptv
C_2H_6	1873 pptv
C_2H_2	364 pptv
C_3H_8	542 pptv
$n\text{-}C_4H_{10}$	111 pptv
CH_4	1880 ppbv
C_2H_5OH	63 pptv
HO_2	2.72pptv
CH_3Br	9.2 pptv
O_3	35 ppbv
$Hg°$	122 ppqv
I_2	1 pptv
Br_2	1 pptv
Cl_2	2 pptv
CO	159 ppbv
H_2O	1203 ppmv

(<1 km altitude) in the spring Intercontinental Chemical Transport Experiment - B field campaign. We examined the possibility of heterogeneous chemistry on the ice surface or in the aerosol. In the simplified mechanism of heterogeneous chemistry, there are three steps which are adsorption onto the aerosol or ice surface, diffusion into the bulk, and Henry's law equilibrium. Although temperature does not affect the transport velocity of a gas to the interface, diffusion into the bulk following the Einstein relation and Henry's coefficient are influenced considerably by temperature. This possibility of heterogeneous chemistry indicated that the environment in the springtime over the Arctic Ocean was too

dry and cold with very little sea salt. In the meteorologically stable Arctic at 255 K it is reasonable to ignore horizontal and vertical transport, deposition, uptake by sea-salt aerosol, and aqueous phase reactions in the simulations. We only considered I_2, Br_2, and Cl_2 emissions from the ocean, and the mixing ratios for these species were set to constant values at each time step to simulate continuous emissions. We also did not consider daily and diel variation in photolysis rates.

Table 2.6. Photolysis rate constants for model simulation. (unit:s^{-1}).

	middle	high	low
$Br_2 \rightarrow Br+Br$	0.029	0.048	0.016
$BrO \rightarrow Br+O$	0.020	0.045	0.014
$HOBr \rightarrow HO+Br$	0.0015	0.003	0.001
$BrCl \rightarrow Br+Cl$	0.0084	0.015	0.005
$BrONO_2 \rightarrow Br+NO_3$	0.00014	0.00027	9.16×10^{-5}
$BrONO_2 \rightarrow BrO+NO_2$	0.00077	0.0015	0.00052
$Cl_2 \rightarrow Cl+Cl$	0.0013	0.0028	0.00097
$ClONO_2 \rightarrow Cl+NO_3$	1.91×10^{-5}	4.1×10^{-5}	1.37×10^{-5}
$ClONO_2 \rightarrow ClO+NO_2$	2.1×10^{-6}	5.57×10^{-6}	1.52×10^{-6}
$O_3 \rightarrow O_2+O(^1D)$	1.82×10^{-6}	6.9×10^{-6}	1.18×10^{-6}
$NO_2 \rightarrow NO_2 + O$	0.0056	0.01	0.0039
$CH_3CHO \rightarrow CH_3 +CHO$	6.4×10^{-7}	2.2×10^{-6}	4.1×10^{-7}
$HCHO \rightarrow H + HCO$	9.1×10^{-6}	2.5×10^{-5}	6.3×10^{-6}
$HCHO \rightarrow H_2 + CO$	2.02×10^{-5}	4.86×10^{-5}	1.5×10^{-5}
$CH_3OOH \rightarrow CH_3O + OH$	2.01×10^{-6}	4.97×10^{-6}	1.5×10^{-6}
$N_2O_5 \rightarrow NO_2 + NO_3$	9.23×10^{-6}	2.5×10^{-5}	7.3×10^{-6}
$H_2O_2 \rightarrow 2OH$	2.14×10^{-6}	5.49×10^{-6}	1.6×10^{-6}

Initial values in the simulations were taken from the ARCTAS measurements (Table 2.5). The data for several minutes were selected from outside the MDE regions for the eight cases and averaged to set the initial values. 75, 50, and 25 percentiles of photolysis rate constants from the MDE regions were categorized into three groups which were high, middle, and low values. The high values were a factor of 2 greater than

Table 2.7. Summary of principal sensitivity experiments.

| | Different rate constants | | | | | | | | | Different halogen conc. | | | | | Different photolysis | | | Different NOx regime | | |
| | Br radical | | | Br2 | | Cl racical | | OH radical | | Br2 (pptv) | | | Cl2 (pptv) | | | | | | | |
	G	K	D2	A	B	K	D1	G	P	1	3	5	1	5	high	mid	low	high	mid	low
S1	X			X		X			X	X			X			X			X	
S2	X			X		X		X		X			X			X			X	
S3		X		X		X			X	X			X			X			X	
S4			X	X		X			X	X			X			X			X	
S5	X				X	X			X	X			X			X			X	
S6	X			X			X		X	X			X			X			X	
S7	X			X		X			X		X		X			X			X	
S8	X			X		X			X			X	X			X			X	
S9	X			X		X			X	X				X		X			X	
S10	X			X		X			X	X			X		X				X	
S11	X			X		X			X	X			X				X		X	
S12	X			X		X			X	X			X			X		X		
S13	X			X		X			X	X			X			X				X
S14	X			X		X			X	X			X			X			X	

* The capital letter indicates different rate constants as described by G for Goodsite et al. (2004), K for Khalizov et al. (2003), D1 for Donohoue et al. (2005), D2 for Donohoue et al. (2005), A for Ariya et al. (2002), B for Balabanov et al. (2005), and P for Pal and Ariya (2004).
* S14 is the case of only considering initial conditions of halogen concentration

middle values and the same pattern existed between the middle and low values (Table 2.6).

We conducted 14 ideal case sensitivity experiments using ARCTAS measurements (Table 2.7). The base case (S1) used average initial concentrations and the middle value of the photolysis rate constants (Table 2.5 and 2.6). In this base case run we utilized the rate constant from Pal and Ariya (2004a) for reaction of $Hg°$ with OH, the rate constant from Goodsite et al. (2004) for reaction of $Hg°$ with Br, the rate constant from Khalizov et al. (2003) for the $Hg° + Cl$ reaction, and the rate constant from Ariya et al. (2002) for the $Hg° + Br_2$ reaction (Table 2.2). In four control runs, we utilized high and low photolysis rate constant values (S10 and S11) (Table 2.6), and high NO_x (5000 pptv NO and 900 pptv NO_2) and low NO_x (0.32 pptv NO and 0 pptv NO_2) regimes (S12 and S13) based on ARCTAS measurements. In five sensitivity runs different rate constants were used for mercury chemistry: (1) Goodsite et al. (2004) for the $Hg°$ with OH reaction (S2), (2) Khlaizov et al. (2003) and Donohoue et al. (2006) for the $Hg°$ with Br reactions (S3 and S4), (3) Balabanov et al. (2005) for the $Hg°$ with Br_2 reaction (S5), and (4) Donohoue et al. (2005) for the $Hg°$ with Cl reaction (S6) (Table 2.2). In three control runs the sensitivity of mercury chemistry to varying mixing ratios of Br_2 and Cl_2 were studied using 3 and 5 pptv Br_2 and 5 pptv Cl_2 mixing ratios (S7-9). One last control run was conducted without re-setting I_2, Cl_2, and Br_2 mixing ratios at each time step to their initial conditions to simulate no emission flux from the surface (S14).

3. Characteristics of MDEs

The general physical and chemical characteristics of the MDEs have been described by Mao et al. (2010a). Briefly, the vertical extent varied from 0.1 to 1 km and

showed concurrent decreases in O_3, Hg°, and selected light hydrocarbons which were consistent with oxidation by halogen species. Our work here is focused on identifying the most important chemical oxidation reactions, determining the depletion rates of O_3 and Hg°, and the effects of varying chemical environments. The chemistry near the surface was fairly consistent between MDE and non-MDE locations. It appears that the main difference was the continuous presence or absence of reactive halogens. In this regard, we examined the MDE and non-MDE cases and did not find any difference in the surface of the sea ice/snow based on views from the nadir camera on the DC-8. In fact, there did not appear to be any open leads that the DC-8 flew over. Important chemical compounds in this study included Hg°, O_3, and Br_2, and the mixing ratios for each case are summarized in Table 2.1, Figures 2.1 and 2.3.

MDEs were sampled over horizontal distances of ~225 km (case 1), and it appeared to be a typical MDE case with distinct demarcations in the spatial series of chemical compounds. We selected 3-10 points before and after the MDE time window to compare the geographical locations and the vertical extent of all MDEs, and we defined these data as outside the MDE. Mixing ratios of Hg° decreased suddenly from >125 ppqv to the LOD except for one point of 22 ppqv. Ozone mixing ratios dropped quickly from ~50 ppbv to 0 - 6 ppbv during the same period. Mixing ratios of Br_2 varied between 3.2 pptv and 5.8 pptv, which are considerably higher than the values outside the MDE (0.05 -1.8 pptv). Moreover, mist chamber collected water-soluble bromide also increased by ~20 pptv and bromide (Br^-) in aerosol phase by at least 3 pptv compared to values outside the MDE. However, 4 samples inside the MDE showed that chloride (Cl^-) in the aerosol phase decreased from 136 to 56 pptv. Mixing ratios of CH_3Cl, CH_3Br, and CH_3I

did not show any discernible changes. Light alkanes and C_2H_2 tracked changes in $Hg°$ and O_3 closely. For example, C_2H_6 mixing ratios decreased by ~700 pptv from outside to inside the MDE areas.
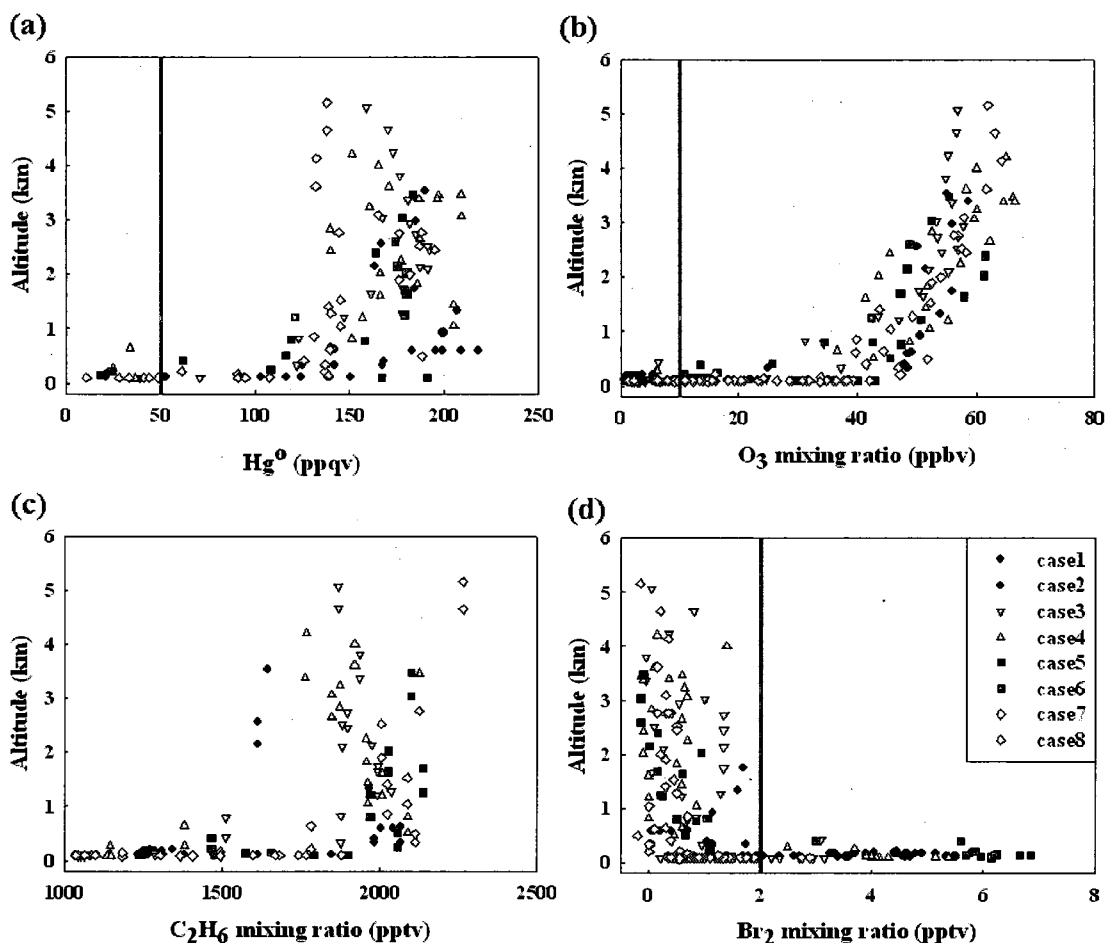
Figure 2.3. Vertical distribution of mixing ratios of $Hg°$(a), O_3(b), C_2H_6 (c), and Br_2 (d) for the outside and inside of all MDEs. Units are ppbv for O_3, ppqv for $Hg°$, and pptv for other species. The vertical red lines of $Hg°$ and O_3 indicate the mixing ratio where values below this represent depletion, while the line of Br_2 indicates the mixing ratio where values greater than this shows mostly corresponding to MDEs.

Backward trajectories for case 1 indicated that the air masses captured in the airborne measurements over the MDE area mostly originated from Nunavut at low altitude traveling off the shore of northern Greenland for 24 hours prior to the

measurements (Figure 2.2). Some air masses during the MDE period traveled at the 850-650 hPa surfaces from southwestern Greenland. In comparison, air masses outside the MDE were transported on 850-500 hPa surfaces from Nunavut or from southwestern Greenland at altitudes ranging from near the surface to 700 hPa.

Case 2 followed case 1 a day later occurring over a similar geographical area around the similar time of the day (~13:00 local time). However, backward trajectories for case 2 suggested that air masses originated from the Baffin Bay area in the mid-troposphere, and were transported to the sampling location through northern Nunavut at near-surface levels. Hg° and O_3 mixing ratios decreased gradually, while Br_2 and aerosol Br^- increased slightly from outside to inside the 34 km MDE region. Variations in light alkanes and C_2H_2 exhibited the same patterns as those in Hg° and O_3. Air masses inside and outside the MDE were sampled at similar altitudes, and the air masses outside the MDE appeared to be transported along the same route as those inside the MDE. Thus, differences in mixing ratios of all trace gases were not as large as those in case 1.

In case 3, the MDE was sampled over a horizontal distance of ~143 km off the coast of northern Alaska. Ozone and Hg° mixing ratios declined steadily, Br_2 varied from 0.2 to 3.2 pptv, and water-soluble bromide was increased up to 19 pptv. Mixing ratios of BrO were ~4 pptv and decreased outside the MDE. Light alkanes and C_2H_2 tracked Hg° and O_3 well. Backward trajectories indicated that air masses traveled near the surface over the northern coast of Alaska and the Beaufort Sea from the Arctic Ocean. Air masses outside the MDE originated from the mid-troposphere. A spike of NO_x levels was observed in this case, which indicated fresh emissions likely coming from the oil

refinery at Prudhoe Bay. The concurrent Hg° mixing ratio was 39 ppqv, possibly reflecting source emissions from the same area.

In case 4, the MDE area spanned 119 km over the Beaufort Sea and the Chukchi Sea. Elemental mercury and O_3 decreased quickly from outside to inside the MDE. Water-soluble bromide varied from 12 - 19 pptv, and Br_2 increased quickly up to 5.5 pptv inside the MDE. The mixing ratio of BrO rose up to 8 pptv followed by a decline outside the MDE. Light alkanes and C_2H_2 followed the same trend in Hg° and O_3. Air masses inside the MDE appeared to be transported near the surface from northern Nunavut, whereas air masses outside the MDE were transported from Europe, Alaska, and the Northwest Territories in the mid–troposphere across the Arctic Ocean.

In cases 5, 6, and 7, mercury depletions spanned horizontal distances of 17, 68, and 56 km respectively, and were observed in the middle of the Arctic Ocean with similar transport pathways and origins of air masses primarily close to surface over the Arctic Ocean. All three cases showed declines in O_3, Hg°, and light alkanes with concomitant increases in Br_2, BrO, and water-soluble bromide.

Case 8 with a ~150 km L-shaped MDE area appeared to be more complicated than all other cases. Hg° mixing ratios exhibited a steep drop from 140 ppqv to the LOD upon entering the MDE area. However, O_3 levels hovered around 30-40 ppbv for the latter part of the MDE sampling, comparable to the levels outside the MDE. Moreover, this MDE was not accompanied by high levels of Br_2, BrO and water-soluble bromide. Air masses inside the MDE had two main origins, the Arctic Ocean and eastern Russia. Air masses outside the MDE were transported at mid- to upper-tropospheric altitudes from the northwestern Pacific and Russia. Very fresh combustion emissions were

observed over the first 36 km of the MDE as indicated by enhanced mixing ratios of NO_x, Hg°, butane, and pentane. Backward trajectories suggested that the air masses came from northern Alaska where high NO_x emissions comparable to the Prudhoe Bay Oil field were indicated by the 2002 EPA NO_x emissions map. Another unique feature in this case was that light alkanes and C_2H_2 tracked O_3 closely, but not Hg°.

General features of the eight MDEs can be summarized as follows. MDEs were found only near the surface over the ocean. Hg° mixing ratios from outside the MDEs varied from 100 ppqv to 250 ppqv, and the corresponding O_3 mixing ratios were usually >30 ppbv. The principal pattern of variation in Hg° from outside to inside the MDE area is characterized by a precipitous fall from >100 ppqv to the LOD, while in comparison O_3 decreased rather gradually from >30 ppbv to <10 ppbv. Four out of the eight cases showed a sudden Br_2 build-up up to 7 pptv inside the MDE areas. Ethyne mixing ratios also decreased during MDEs, and it was correlated with O_3 at $r^2 = 0.72$. Moreover, light alkanes such as C_2H_6, C_3H_8, C_4H_{10} and C_5H_{12} showed the same pattern of variation as that of C_2H_2. Similar findings were reported previously for O_3 depletion events (ODEs) (Mao et al., 2010a; Eneroth et al., 2007). A general feature ascertained from backward trajectories was that air masses outside most MDEs originated from the mid-troposphere, whereas air masses inside MDEs traveled at low altitude over the ocean surface probably entraining halogen-rich chemical compounds. Analysis of variations in chemical compounds and backward trajectories indicated that halogen-rich air could be related to changes in Hg°, O_3, and light alkanes. In addition, fresh combustion emissions were sampled as evidenced by high NO_x levels in cases 3 and 8. The backward trajectories suggested that the high NO_x originated from unknown sources in northern Alaska.

4. Box Model Simulations

4.1. Base Case Results

The results of the base case (S1) are presented in Figures 2.4, 2.5, 2.6, and 2.7 and Table 2.8. We defined depletion as mixing ratios <50 ppqv for Hg°, 10 ppbv for O_3, and 25 pptv for C_2H_2. In the model runs Hg° was depleted in ~22 hours, and about 97% of Hg° was transformed to up to 70 ppqv $HgBr_2$. HgO was the second most abundant RGM species, but its level was about 45-fold less than that of $HgBr_2$. Some studies assumed a radical reaction such as the HgBr + BrO reaction in the Arctic spring (Calvert and Lindberg, 2003; Xie et al., 2008), and BrHgOBr was one of the main RGM products. This radical reaction was not included in our model due to a lack of experimental rate constants. The dominant product, $HgBr_2$, indicated that the reaction of Hg° with Br radical, which is principally produced by photolysis of Br_2, is very important to Hg° depletion. Ozone was depleted in 23 hours, and C_2H_2 was depleted in ~36 hours. Ethyne decreased very rapidly due to the reaction with abundant Br radical after O_3 was reduced to <1 ppbv. Cases 1-6 of the ARCTAS measurements showed comparatively distinct declines of C_2H_2 and light alkanes compared to the simulation results. Ethyne was not depleted in the field observations, but the range of decrement was significant spanning 72-420 pptv from outside to inside the MDEs. In the simulations C_2H_2 was decreased by 340 pptv, which was in the same range as the observations. Light alkanes were also consistently decreased during the 100 hours of simulation. For example, C_2H_6 decreased to ~32 % of its initial concentration and C_4H_{10} declined to about 76% of its initial concentration after 100 hours of simulation. A decline of 205-920 pptv in ethane was observed from outside to inside the MDEs compared to about a decrease of ~600 pptv

after 100 hours of simulation. Thus, our box model simulations appear to be able to reproduce the decreases of various light alkanes and C_2H_2 captured in the ARCTAS measurements as well as depletion of $Hg°$ and O_3. This suggests that the chemistry represented in the box model sufficiently depicts chemical processes conducive to the occurrence of MDEs and O_3 depletion events (ODEs).

Table 2.8. Prominent τ_{dep} values for several sensitivity experiment results

		τ_{dep} (hours)		
		$Hg°$	O_3	C_2H_2
Base		21.9	23.1	35.9
Rate constant of $Hg° + Br$	Khalizov et al. (2003)	28.4	23.1	35.9
	Donohoue et al. (2006)	32	23.1	35.9
Different Br_2 mixing ratio	3 pptv	7.6	15.5	23.4
	5 pptv	3.4	9.3	14.2
Different photolysis constant	High	10	19.9	30.3
	Low	32.7	25.6	41.6
High NO_x regime		5.6	21.2	36.1

Furthermore, we simulated conditions without O_3 chemistry but included O_3 photolysis in our chemical mechanism. It indicated that certain levels of O_3 provided an additional sink of halogen radicals including Br, and hence the time to reach $Hg°$ depletion was longer. The results suggest a close relation between O_3 and $Hg°$, and thus we conducted simulations with O_3 chemistry afterwards to make them more realistic.

4.2 Influence of Rate Constant Values

Applying different rate constants for $Hg°$ reactions with Cl, OH, and Br_2 (S2, S5, and S6) did not affect the time it took to reach depletion (denoted as τ_{dep}) of $Hg°$ (Tables 2.2 and 2.8 and Figure 2.4). However, different rate constants for $Hg°$ reaction with Br (S3 and S4) influenced the final product composition and τ_{dep}. The amounts of HgO, HgCl, $HgCl_2$, and $Hg(OH)_2$ produced were the greatest using the Donohoue et al. (2006) rate constant value (S4) compared to application of other values(S1 and S3). Using the

rate constants of Donohoue et al. (2006) and Khalizov et al. (2003) (S3 and S4) led to a slow decrease in Hg° at first followed by a faster decline compared to the base case. Furthermore, the variation in the rate constant values of Hg° reaction with Br was also important in determining τ_{dep}. Compared to the base case (S1), using the rate constant from Khalizov et al. (2003) and Donohoue et al. (2006) (S3 and S4) increased τ_{dep} (Table 2.8). However, about 97% of the RGM product was HgBr$_2$, the same as in the base run case.
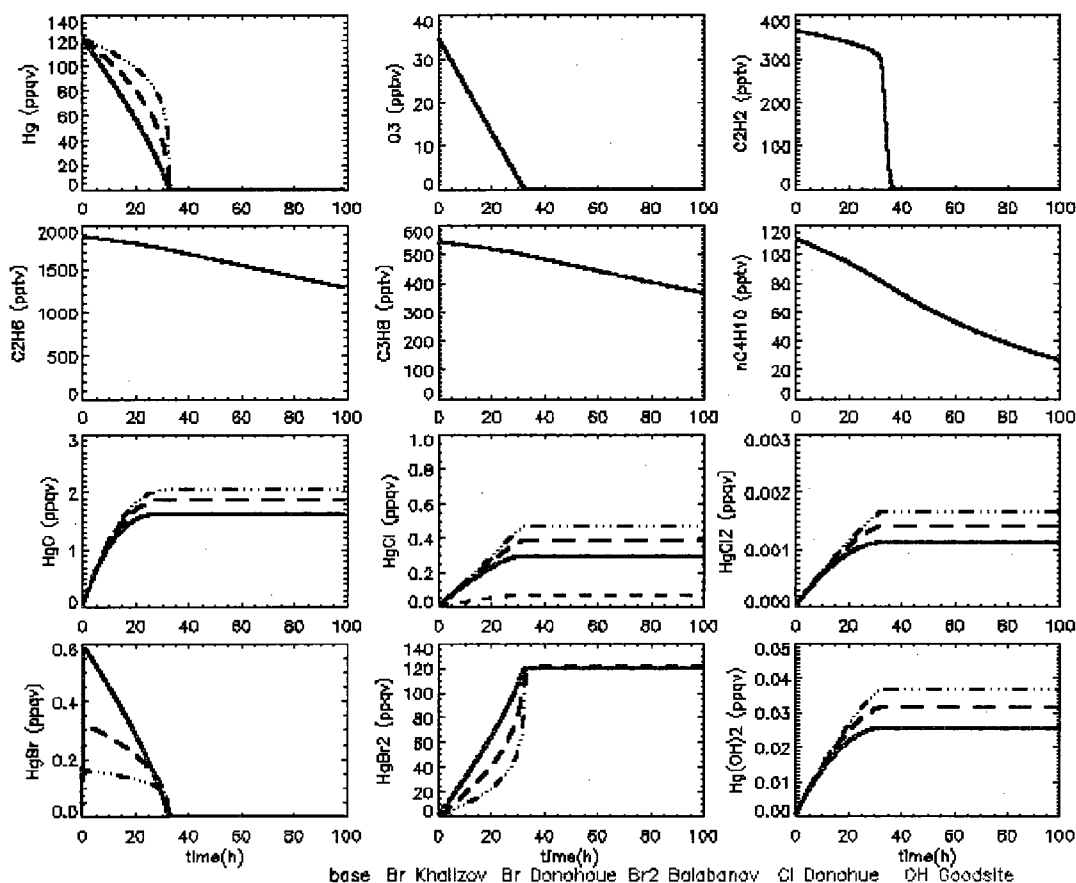
Figure 2.4. 100 hour model simulation using different rate constants. Black is base run, blue is Khalizov et al (2003) and red is Donohoue et al. (2006) for Hg° + Br, green is Balabanov et al. (2005) for Hg° + Br$_2$, purple is Donohoue et al. (2005) for Hg° + Cl, and grey is Goodsite et al. (2004) for Hg° + OH. Unit is ppbv for O$_3$, pptv for C$_2$H$_2$ and light alkanes, and ppqv for mercury species.

The rate constant of Hg° with BrO varies over the range of 1×10^{-15} - 1×10^{-13} cm^3 molecule^{-1} s^{-1} at 298 K (Raofie and Ariya, 2003) and the temperature dependent rate constants were not provided in that study. We ran three simulations using rate constants of 1×10^{-13}, 1×10^{-14}, and 1×10^{-15} cm^3 molecule^{-1} s^{-1} in the base case run to study the influence of the reaction on Hg° depletion. With the lowest rate constant, Hg° reaction with BrO was negligible. With the largest rate constant, the τ_{dep} value for Hg° was reduced by 8 hours and slightly more HgO was produced than HgBr$_2$. When the temperature of 255 K was considered, the reaction of Hg° with BrO did not seem to be important in our simulations, which suggests a negligible effect of Hg° reaction with BrO on the occurrence of MDEs in the Arctic spring.

4.3 Influence of Halogen Radical Concentrations

A simulation was conducted without halogen compounds being re-set to the initial conditions at each time step (S14). It was found that ~11% of Hg° was transformed to RGM and O$_3$ was decreased by ~0.5% after 100 hours of simulation. This suggested that continuous emission of halogen compounds is imperative to the occurrence of MDEs and ODEs in the Arctic springtime.

In addition, simulations were performed using 3 and 5 pptv Br$_2$ and 5 pptv Cl$_2$ (S7, S8, and S9) (Figure 2.5 and Table 2.8). We found that the higher the Br$_2$ concentration was, the faster the Hg°, O$_3$, and C$_2$H$_2$ depletion occurred. The τ_{dep} value decreased almost linearly with increases in Br$_2$. Adding 5 pptv of Cl$_2$ (S9) reduced the τ_{dep} value for each compound by 20 - 30 minutes. The rate constant of Cl and Br with Hg° are of the same order of magnitude, 10^{-12} cm^3 molecule^{-1} s^{-1}, at 255 K. However, the order of magnitude for the rate constant of Cl radical with hydrocarbons and O$_3$ are 10^{-11} cm^3

molecule^{-1} s^{-1} except n-C$_4$H$_{10}$, 10^{-10} cm^3 molecule^{-1} s^{-1}; the reactivity of Br radical with O$_3$ is 10^{-13} cm^3 molecule^{-1} s^{-1} and that of Br radical with C$_2$H$_2$ is 10^{-14} cm^3 molecule^{-1} s^{-1}. Furthermore, there was a lack of bromine reactions with light alkanes in the model due to insufficient kinetic information available in literature. Therefore, the high reactivity of Cl with abundant hydrocarbons and O$_3$ caused τ_{dep} value for Hg$°$ to be much more sensitive
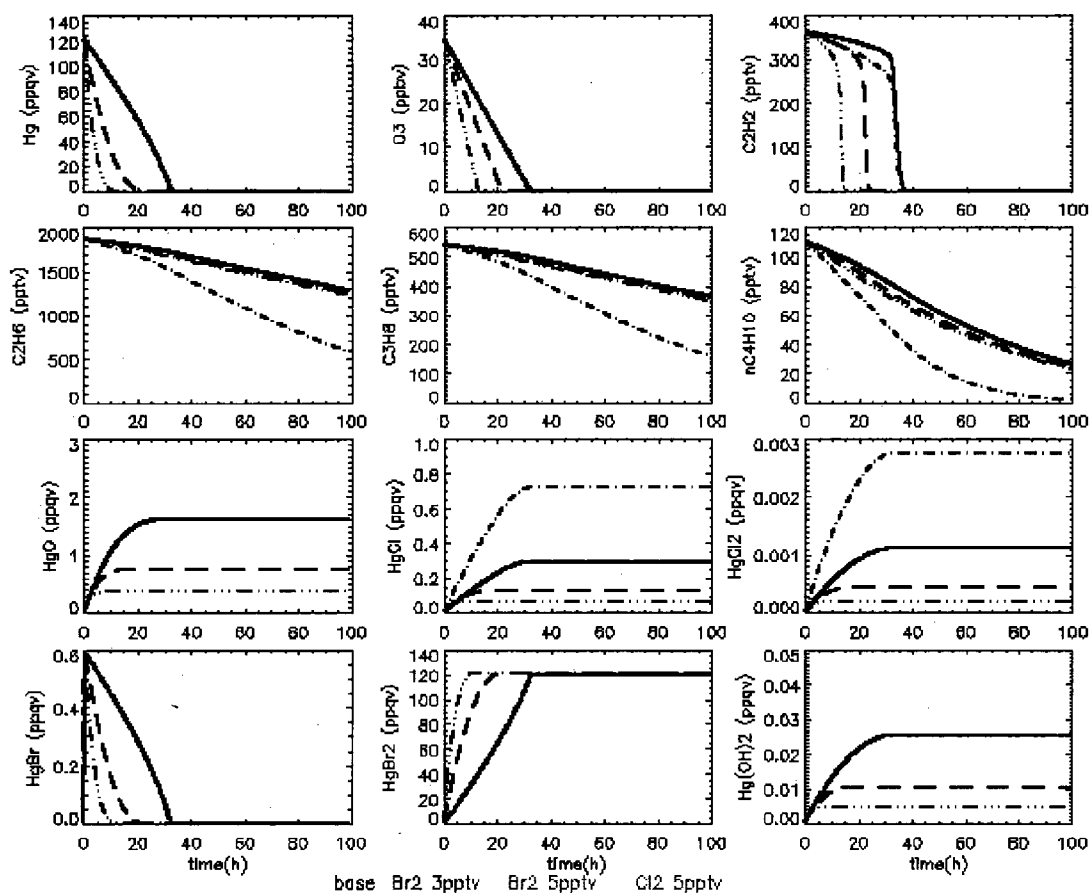
Figure 2.5. 100 hour model simulation using different halogen mixing ratios. Black is base run, blue is 3 pptv Br$_2$, red is 5 pptv Br$_2$, and green is 5 pptv Cl$_2$. Unit is same as Figure 2.4.

to Br$_2$ than Cl$_2$. Approximately 99% of the RGM product was HgBr$_2$, with the higher Br$_2$ cases showing a slight increase in the amount of HgBr$_2$. ARCTAS measurement data

showed that Br_2 mixing ratios varied over 1-7 pptv in most MDEs, and thus it is reasonable to speculate based on our box model simulations that Br_2 (Br) played an important role in the occurrence of MDEs.

At the 5 pptv Cl_2 mixing ratios of light alkanes decreased significantly compared to cases with additional input of Br_2. For instance, we found a 70% decrease in C_2H_6 in 100 hours for 5 pptv Cl_2 compared to a ~35% decrease in other cases.

4.4 Influence of Photolysis Rate Constants

Different photolysis rate constants affected the τ_{dep} value for $Hg°$ (Table 2.6 and 2.8 and
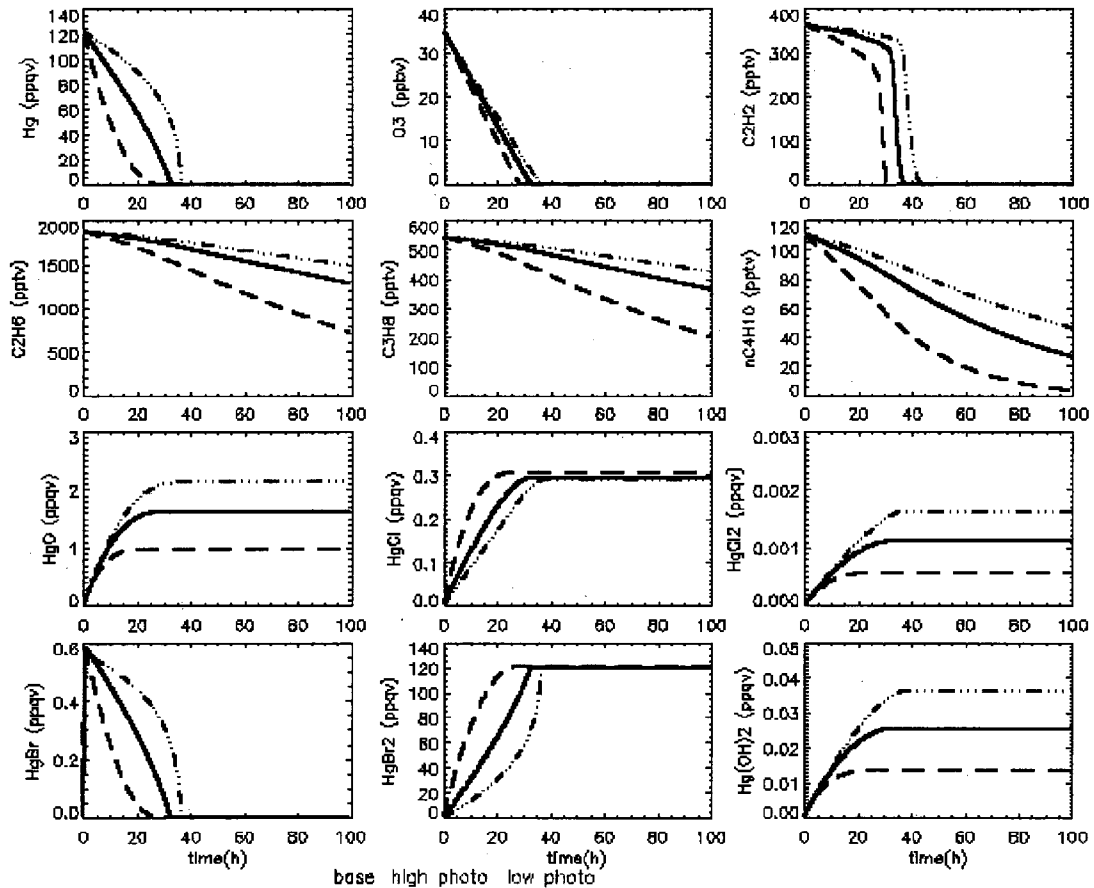
Figure 2.6. 100 hour model simulation for different photolysis rate constants. Black is base run, blue is high photolysis case, and red is low photolysis case. Unit is same as Figure 2.4.

- 60 -

Figure 2.6) and higher photolysis rate constants (S10) drove faster depletion for Hg°. The main RGM product was again $HgBr_2$. However, HgO, the second most abundant RGM product in the high photolysis case (S10) was about 52% of its values in the base case because fast production of Br radicals accelerated the Hg° + Br reaction. Moreover, the higher photolysis case showed a more rapid decrease in C_2H_2 and O_3 compared to the lower photolysis. Light alkanes also showed faster decreases in the high photolysis case (S10) and slower decreases in the low photolysis case (S11) (e.g., C_2H_6 showed a 62 % decrease in the high photolysis case and a 21 % decrease in the low photolysis case after 100 hours of simulation). We examined the ARCTAS measurements for correlation between the Br_2 photolysis rate constant and O_3 mixing ratios inside the MDE regions, but we did not find a strong relationship. This is probably not surprising since the depletion events were sampled at various stages of their lifetime.

4.5 High Versus Low NO_x Regimes

ARCTAS measurements showed that the NO mixing ratio was commonly about 10 pptv and NO_2 was ~0 pptv. However, a couple of cases showed very high mixing ratios of NO and NO_2 for short time periods which indicated an influence of fresh emissions from northern Alaska, including the Prudhoe Bay Oil field. This motivated simulations of high and low NO_x regimes.

The low NO_x regime (S13) was based on case 7 of the eight ARCTAS MDEs. The results for low NO_x were similar to the base case (Figure 2.7). In the high NO_x regime (S12), Cl radical concentration was slightly increased during the 100 hours of simulation due to acceleration of Cl production from the reaction of ClO + NO. Thus

light alkanes decreased slightly more than in the base case after 100 hours of simulation due to reaction of light alkanes with the Cl radical.
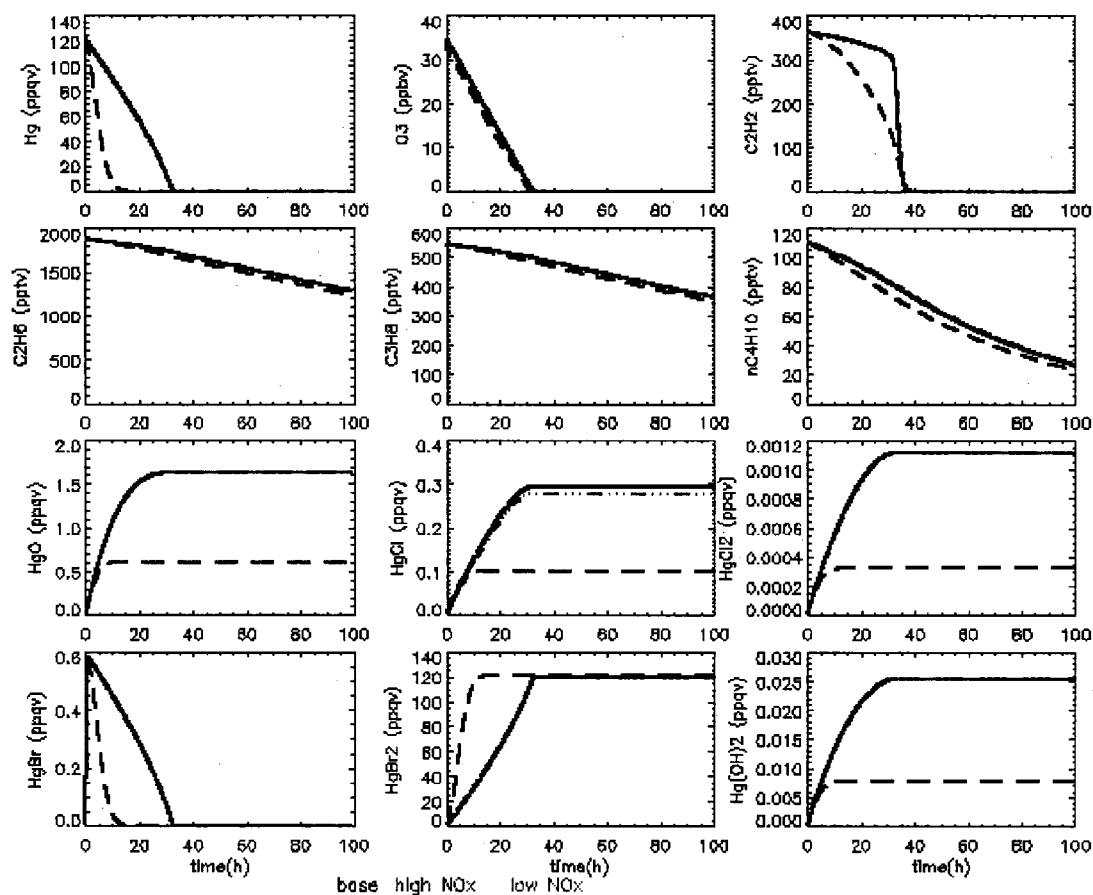
Figure 2.7. 100 hour model simulation for high NO_x and low NO_x regime. Black is base run, blue is high NO_x regime, and red is low NO_x regime. Unit is same as Figure 2.4.

Different from Cl, Br reactions with light alkanes were not implemented in our model, and thus high NO_x concentrations significantly increased the Br radical concentration in comparison to the Cl radical. Fast production of Br radicals in the high NO_x regime (S12) occurred during the first part (33 hours) of simulation, with a decreased BrO amount. Increased Br radical concentrations were presumably due to the

reaction of BrO with NO. Thus, O_3 and Hg° depletion occurred in ~2 hours for O_3 and ~16 hours for Hg° sooner compared to the base case (Table 2.8). Ethyne declined at a faster rate initially in the high NO_x regime (S12) compared to the base case (S1) because of its reaction with Br radical, but overall the depletion time in the high NO_x regime (S12) was similar to that of the base case (S1). Note that these results suggested that the impact of high NO_x regime (S12) on Hg° depletion could be exaggerated slightly due to the lack of rate constants of Br with light alkanes.

Moreover, we simulated the corresponding chemical environments at higher NO_x levels based on ARCTAS measurements. This simulation showed that higher-NO_x induced changes in hydrocarbon concentrations slightly affected the RGM composition and τ_{dep} for Hg° in high NO_x regime. Compared to the high NO_x level alone, τ_{dep} for Hg° was prolonged by 30 minutes, and HgO production was increased by 11%. The τ_{dep} value for O_3 was prolonged by 1.5 hours.

From the ARCTAS measurements we did not find distinguishable characteristics for O_3, C_2H_2, and light alkanes in the high NO_x regimes, but Hg° was 28 – 44 ppqv during these time periods in cases 3 and 8 with a possible contribution from combustion. However, these levels were still low compared to the values outside the MDEs, and indicated the possibility of fast Hg° oxidation in the high NO_x regime as shown in the model simulations. The other interesting simulation result was that O_3 and C_2H_2 were not depleted as fast as Hg° in the high NO_x regime. The data of case 8 showed that the high NO_x area did not exhibit correspondingly high O_3, C_2H_2, C_2H_6, and C_3H_8. However, simulation results could help explain case 8 in which light alkanes, C_2H_2, and O_3 followed a similar pattern but not Hg°. The BrO loss mechanism with NO produced

more NO_2 which is an O_3 precursor; hence O_3 depletion was slower than Hg° depletion. Moreover, the Br radical production pattern, which was higher for the first simulation period and lower for the last simulation period compared to the base run, could explain C_2H_2 depletion in case 8. Furthermore, case 3 also had high NO_x area but O_3 and C_2H_2 resembled with Hg°. Br_2 mixing ratio in case 3 was higher than case 8, and hence we simulated high NO_x regime with a consistent source of 2 pptv Br_2, which was in the range of Br_2 in case 3. The simulation indicated O_3 and C_2H_2 depleted faster than original simulation of high NO_x regime; τ_{dep} was 16.9 hours for O_3 and 27.5 hours for C_2H_2. Therefore, the simulation results indicated that different range of Br_2 mixing ratio drove the different feature of cases 3 and 8.

5. Conclusions

Atmospheric MDEs observed during the ARCTAS field campaign were investigated by analysis of aircraft data and box modeling. MDEs were observed to occur near the surface over the Arctic Ocean with coincident O_3 depletion, high Br_2 levels, and decreases in light alkanes and C_2H_2. Generally, air masses inside the MDEs transported at low levels over the ocean, and thus a distinguishable chemical feature of the air is that it is likely halogen rich.

We developed a gas phase box model including mercury, halogen species, and ozone chemistry with input from the ARCTAS measurements. We simulated several sensitivity experiments to study the influence of variable rate constants of Hg° chemistry, concentrations of halogen compounds, photolysis rate constant values, and NO_x mixing ratios on Hg° depletion. The results suggested that high Br_2 mixing ratios, high photolysis rate constants, and high NO_x regime caused accelerated Hg° depletion. These

three environments accelerated Br radical production and hence increased the rate of Hg° depletion. Moreover, we found that Hg° responded in a more sensitive manner to the variations in the chemical environment compared to O_3. This could possibly explain the moderate decreases in O_3 mixing ratios in MDE regions compared to total depletion of Hg°.

III. Cycling of gaseous elemental mercury: Importance of water vapor

1. Introduction

Mercury, a toxic compound as classififed by the U.S. Environmental Protection Agency, exists in three forms in the atmosphere; gaseous elemental mercury (Hg^o), reactive gaseous mercury (RGM), and particulate mercury (PHg). Measurement data have showed that the concentrations of RGM and PHg are two orders of magnitudes less than the concentration of Hg^o. For example, the mean or median value of Hg^o was reported to be <2.5 ng m^{-3} over the Pacific and at rural regions in North America (Laurier et al., 2003; Radke et al., 2007; Mao et al., 2008; Swartzendruber et al., 2006; Poissant et al., 2005; Lyman and Gustin, 2008), while the mean values were reported as 7–13 pg m^{-3} for RGM and 9-13 pg m^{-3} for PHg in northern Nevada and over the North Pacific (Lyman and Gustin, 2008; Laurier et al., 2003).

Mercury is primarily emitted to the atmosphere in elemental form (Hg^o), and its sources are biomass burning, waste incinerators, coal-fired power plants, volcanos, and automobiles (Brunke et al., 2001; Hall et al., 1990; Pyle and Mather, 2003; Won et al., 2007; Glodek and Pacyna, 2009; Wilson et al., 2006). Moreover, natural mercury emissions include release from vegetation, soil, and the ocean (Bash et al., 2004; Sigler and Lee et al., 2006). In contrast, mercury sinks from the atmosphere are by wet and dry deposition (Mao et al., 2008; Sakata and Asakura, 2007). A regional mercury study over eastern Asia suggested that RGM and PHg were mostly deposited around source regions, while Hg^o was transported over the Pacific and accounted for 39% of total Asian emissions (Pan et al., 2008). Hence, the transformations from Hg^o to RGM and PHg are crucial for the global mercury cycle. Several model studies indicate that the principal transformations of Hg^o to RGM are through oxidation by the Br radical in the marine

boundary layer and O_3 in urban boundary layer (Kim et al., 2010; Holmes et al., 2009, 2010; Xie et al., 2008; Shon et al., 2005).

Box model is useful tool to study mercury chemistry in various environments. Some previous box modeling studies conceptualized possible atmospheric processes in one big box, which were mainly chemical processes, dry deposition, and emissions (Shon et al., 2005; Hedgecock et al. 2004 and 2005). Meanwhile, a box model is also utilized to study complicated chemical processes in the atmosphere while ignoring other atmospheric processes. For example, mercury depletion events (MDEs) in Arctic springtime were studied by utilizing comprehensive chemical reactions in the Arctic springtime atmosphere (Xie et al., 2008; Kim et al., 2010). Here, we focused on chemical transformations of mercury species in the atmosphere including mercury, halogen, ozone, and sulfur chemistries in the gas and aqueous phases. Moreover, we considered one more atmospheric process, dry deposition, in the chemical box model for the last set of sensitivity experiments.

Gaseous elemental mercury has been measured in the northeastern U.S. since 2003 as part of the UNH-NOAA AIRMAP program and speciated mercury has been measured since 2007 (Mao et al., 2008, 2010b; Sigler et al., 2009). The seasonally averaged diurnal variation of Hg^o showed ~20 ppqv decrease at night in summer and fall when the nocturnal inversion layer frequently occured (Talbot et al., 2005; Mao et al., 2008). The nighttime loss of Hg^o appears to be quite variable, ranging from nearly complete removal to no perceiveable loss on a given night. Here, we conducted sensitivity experiments with the chemical box model to interpret mercury chemical

processes affecting the diurnal cycle of Hg° at Thompson Farm, one of the measurement sites of the AIRMAP program.

2. Methods

2.1 Mercury measurements

Speciated atmospheric mercury was measured at Thomson Farm (TF, 43.11N, 70.95W) in southern New Hampshire year round. A detailed description of the TF site can be found in Sigler et al. (2009). At both sites we operate a Tekran system which consists of a model 1130 to measure RGM, a model 1135 to measure PHg, and 2537A cold vapor fluorescence detector. Elemental Hg was quantified with a five minute time resolution. Reactive Hg and PHg were determined using a two hour sampling and one hour flushing and desorption sequences. The instruments were configured and operated identically at both sites according to the U.S. Environmental Protection Agency Standard Operating Procedures for Analysis of Gaseous and Fine Particulate-Bound Mercury (U.S. EPA, 2009), with one modification. Instead of using the Tekran commercial water removal cartridge system, we developed a custom cold finger unit which operates autonomously only producing water as a waste by-product. The system is extremely clean and we believe that it helps keep the blank on the speciated measurements at zero. Thus, blank subtraction is rarely required. Calibration of the 2537A unit was conducted automatically every 24 desorption cycles, and this was verified every six months using a Tekran model 2505 Saturated Mercury Vapor Calibration Unit (*i.e.*, direct injection from the headspace of a thermoelectrically cooled Hg° reservoir) to confirm absolute calibration. A detailed description of the measurements can be found in Talbot et al. (2010).

2.2 Box model development

We developed a gas phase chemical box model that included O_3, halogen, and mercury chemical mechanisms (Kim et al., 2010). We added gas phase sulfur chemistry and aerosol chemistry into our previous model and the detailed chemistries are presented in Tables 3.1 - 3.4.

$$\frac{d[C_g]}{dt} = G_p - G_l - k_{MT}L([C_g] - \frac{1}{HRT}[C_{aq}])$$ (Equation 3.1)

$$\frac{d[C_{aq}]}{dt} = k_{MT}L([C_g] - \frac{1}{HRT}[C_{aq}]) + A_p - A_l$$ (Equation 3.2)

The gas phase concentrations of chemical compounds ($[C_g]$) are determined by gas phase chemical production (G_p), gas phase chemical loss (G_l), and the amount of uptake by aerosols (Equation 3.1). Here, we ignored other atmospheric processes such as horizontal and vertical transport, dry deposition, and emission. We considered the impact of dry deposition in a set of sensitivity expriments. We included mass transfer between gas and aqueous phases (aerosol uptake) and chemical production and loss in the aqueous phase (A_p and A_l) (Equation 3.2). The mass transfer between gaseous-aqueous phases is controlled by the liquid water content (L), the rate of mass transport from the gas to aqueous phases (k_{MT}), and the difference in chemical concentrations between the gas phase and interface of gas-aqueous phases ($C_g - C_{interface}$). Here, our focus is on nighttime loss so we assumed an equilibrium state for gas-aqueous phases to obtain $C_{interface}$, due to high nighttime relative humidity of >70% (Pirrone et al., 2000). Hence the concentration at the interface ($C_{interface}$) is controlled by the Henry's Law constant (H) and concentration in the aqueous phase (C_{aq}). The units of concentrations (e.g. C_g and $C_{interface}$) were cm^{-3}.

The mass transport between gas-aqueous phases consists of molecular diffusion in the gas phase and gas-kinetic collisions at the interface of gas-aqueous phases (Schwartz, 1986), and it was formulated by utilizing the characteristic time. The molecular diffusion to the aerosol surface is controlled by aerosol radius (a) and the diffusion coefficient (D_g) in the first term on the right-hand side of equation 3.3. The gas-kinetic collision at the interface is determined by the accommodation coefficient (α), molecular speed ($\bar{v}$), and aerosol radius (a) in the second term on right-hand side of equation 3.3.

$$k_{MT} = (\frac{a^2}{3D_g} + \frac{4a}{3\bar{v}\alpha})^{-1}$$ (Equation 3.3)

There are two types of chemical reactions in the aqueous phase; reversible and irreversible reactions. For the reversible reactions we assumed that the reaction is controlled by diffusion in the phase. We considered mostly charged species, but the diffusion rate of bimolecular reactions between uncharged species ($\sim 10^{10}$ L mol^{-1} s^{-1}) is utilized in the model due to little impact of ionic strength on the diffusion rate (Finlayson-Pitts and Pitts, 2000). We added 39 gas-aqueous equilibrium reactions, 28 reversible reactions in aqueous phase, and 51 irreversible reactions in the aqueous phase (Table 3.2 - 3.4).

Table 3.1. Selected acidic gas phases reactions.

Reactions	Rate constant/ equilibrium constant	References
OH + SO$_2$ +M$\rightarrow$ HOSO$_2$ + M	4.5×10^{-31} exp $(T/300)^{-3.9}$ [N$_2$]cm^3 molecule^{-1} s^{-1}	Atkinson et al. (2004)
HOSO$_2$ + O$_2$ $\rightarrow$ HO$_2$ + SO$_3$	1.3×10^{-11} /exp (330/T) cm^3 molecule^{-1} s^{-1}	Atkinson et al. (2004)
SO$_3$+ 2H$_2$O $\rightarrow$ H$_2$SO$_4$ + H$_2$O	8.5×10^{-11} exp(6540/T) cm^3 molecule^{-1} s^{-1}	Sander et al. (2006)
N$_2$O$_5$ + H$_2$O $\rightarrow$ 2HNO$_3$	2.5×10^{-22} cm^3 molecule^{-1} s^{-1}	Atkinson et al. (2004)

Table 3.2. Gas-aqueous phases equilibrium reactions.

Reactions	Equilibrium constant (unit: M atm^{-1})	References
$Hg_{(g)} \leftrightarrow Hg_{(aq)}$	0.11-0.14	Sanemasa, 1975/ Schroeder and Munthe, 1998
$HgO_{(g)} \leftrightarrow HgO_{(aq)}$	3.2×10^6	Petersen et al., 1998
$HgCl_{2(g)} \leftrightarrow HgCl_{2(aq)}$	2.75×10^6	Schroeder and Munthe, 1998
$HgBr_{2(g)} \leftrightarrow HgBr_{2(aq)}$	2.75×10^6	Hedgecock and Pirrone, 2004
$Hg(OH)_{2(g)} \leftrightarrow Hg(OH)_{2(aq)}$	1.2×10^4	Lindqvist and Rodhe, 1985
$O_{3(g)} \leftrightarrow O_{3(aq)}$	1.03×10^{-2} (at 298K)	Sander et al. (2006)
$H_{(g)} \leftrightarrow H_{(aq)}$	2.6×10^{-4} (at 298K)	Sander et al. (2006)
$OH_{(g)} \leftrightarrow OH_{(aq)}$	39 (at 298K)	Sander et al. (2006)
$HO_{2(g)} \leftrightarrow HO_{2(aq)}$	690 (at 298)	Sander et al. (2006)
$H_2O_{2(g)} \leftrightarrow H_2O_{2(aq)}$	7.73×10^4 (at 298K)	Sander et al. (2006)
$NO_{3(g)} \leftrightarrow NO_{3(aq)}$	3.8×10^{-2} (at 298K)	Sander et al. (2006)
$CH_3Br_{(g)} \leftrightarrow CH_3Br_{(aq)}$	0.173 (at 298K)	Sander et al. (2006)
$CH_3OOH_{(g)} \leftrightarrow CH_3OOH_{(aq)}$	300 (at 298K)	Sander et al. (2006)
$HCHO_{(g)} \leftrightarrow HCHO_{(aq)}$	3.23×10^3 (at 298K)	Sander et al. (2006)
$CH_3CHO_{(g)} \leftrightarrow CH_3CHO_{(aq)}$	12.9 (at 298K)	Sander et al. (2006)
$Cl_{(g)} \leftrightarrow Cl_{(aq)}$	2.3 (at 298K)	Sander et al. (2006)
$ClO_{(g)} \leftrightarrow ClO_{(aq)}$	0.71 (at 298K)	Sander et al. (2006)
$ClOO_{(g)} \leftrightarrow ClOO_{(aq)}$	17 (at 298K)	Sander et al. (2006)
$OClO_{(g)} \leftrightarrow OClO_{(aq)}$	17 (at 298K)	Sander et al. (2006)
$HOCl_{(g)} \leftrightarrow HOCl_{(aq)}$	660 (at 298K)	Sander et al. (2006)
$Br_{2(g)} \leftrightarrow Br_{2(aq)}$	0.725 (at 298K)	Sander et al. (2006)
$BrCl_{(g)} \leftrightarrow BrCl_{(aq)}$	0.98 (at 298K)	Sander et al. (2006)
$HOBr_{(g)} \leftrightarrow HOBr_{(aq)}$	130 (at 298K)	Sander et al. (2006)
$HNO_{3(g)} \leftrightarrow HNO_{3(aq)}$	2.1×10^5 (at 298K)	Schwartz and White (1981)
$HONO_{(g)} \leftrightarrow HONO_{(aq)}$	49 (at 298K)	Schwartz and White (1981)
$HCl_{(g)} \leftrightarrow HCl_{(aq)}$	727 (at 298K)	Seinfeld and Pandis (1998)
$SO_{2(g)} \leftrightarrow SO_{2(aq)}$	$\ln H = -39.72 + 4250/T + 4.525 \times \ln(T)$	Sander et al. (2006)
$O_{2(g)} \leftrightarrow O_{2(aq)}$	$\ln H = -161.6 + 8160/T + 22.39 \times \ln(T)$	Sander et al. (2006)
$NO_{(g)} \leftrightarrow NO_{(aq)}$	$\ln H = -157.1 + 7950/T + 21.298 \times \ln(T)$	Sander et al. (2006)
$CO_{(g)} \leftrightarrow CO_{(aq)}$	$\ln H = -178 + 8750/T + 24.875 \times \ln(T)$	Sander et al. (2006)
$CO_{2(g)} \leftrightarrow CO_{2(aq)}$	$\ln H = -145.1 + 8350/T + 19.96 \times \ln(T)$	Sander et al. (2006)
$CH_{4(g)} \leftrightarrow CH_{4(aq)}$	$\ln H = -194.7 + 9750/T + 27.274 \times \ln(T)$	Sander et al. (2006)
$C_2H_{6(g)} \leftrightarrow C_2H_{6(aq)}$	$\ln H = -240.2 + 12420/T + 33.744 \times \ln(T)$	Sander et al. (2006)
$C_3H_{8(g)} \leftrightarrow C_3H_{8(aq)}$	$\ln H = -281.1 + 14510/T + 39.652 \times \ln(T)$	Sander et al. (2006)
$n-C_4H_{10(g)} \leftrightarrow n-C_4H_{10(aq)}$	$\ln H = -269.9 + 14330/T + 37.734 \times \ln(T)$	Sander et al. (2006)
$C_2H_{2(g)} \leftrightarrow C_2H_{2(aq)}$	$\ln H = -145.8 + 7880/T + 20.384 \times \ln(T)$	Sander et al. (2006)
$Cl_{2(g)} \leftrightarrow Cl_{2(aq)}$	$\ln H = -134.4 + 7590/T + 18.702 \times \ln(T)$	Sander et al. (2006)
$HBr_{(g)} \leftrightarrow HBr_{(aq)}$	$\ln H = 7.6 + 7117/T - 0.035 \times T$	Brimblecombe and Clegg (1989)
$NH_{3(g)} \leftrightarrow NH_{3(aq)}$	$\ln H = -9.84 + 4160/T$	Sander et al. (2006)

Table 3.3. Aqueous equilibrium reactions.

Reactions	Equilibrium constant	Refrences
$Hg^{2+} + SO_3^{2-} \leftrightarrow HgSO_3$	2×10^{13} M^{-1}	van Loon et al., 2001
$HgSO_3 + SO_3^{2-} \leftrightarrow Hg(SO_3)_2^{2-}$	1×10^{10} M^{-1}	van Loon et al., 2001
$Hg^{2+} + OH^- \leftrightarrow Hg(OH)^+$	3.98×10^{10} M^{-1}	Smith and Martell, 2004
$Hg(OH)^+ + OH^- \leftrightarrow Hg(OH)_2$	1.58×10^{11} M^{-1}	Smith and Martell, 2004

$Hg(OH)^+ + Cl^- \leftrightarrow Hg(OH)Cl$	$2.7 \times 10^7 \, M^{-1}$	Xiao, 1994
$Hg^{2+} + Cl^- \leftrightarrow HgCl^+$	$2 \times 10^7 \, M^{-1}$	Smith and Martell, 2004
$HgCl^+ + Cl^- \leftrightarrow HgCl_2$	$5.0 \times 10^6 \, M^{-1}$	Smith and Martell, 2004
$HgCl_2 + Cl^- \leftrightarrow HgCl_3^-$	$6.7 \times 10^0 \, M^{-1}$	Clever et al., 1985
$HgCl_3^- + Cl^- \leftrightarrow HgCl_4^{2-}$	$1.3 \times 10^1 \, M^{-1}$	Clever et al., 1985
$Hg^{2+} + Br^- \leftrightarrow HgBr^+$	$1.1 \times 10^9 \, M^{-1}$	Clever et al., 1985
$HgBr^+ + Br^- \leftrightarrow HgBr_2$	$2.5 \times 10^8 \, M^{-1}$	Clever et al., 1985
$HgBr_2 + Br^- \leftrightarrow HgBr_3^-$	$1.5 \times 10^2 \, M^{-1}$	Clever et al., 1985
$HgBr_3^- + Br^- \leftrightarrow HgBr_4^{2-}$	$2.3 \times 10^1 \, M^{-1}$	Clever et al., 1985
$BrCl + Cl^- \leftrightarrow BrCl_2$	$6.0 \, M$	Wang et al. (1994)
$SO_2H_2O \leftrightarrow HSO_3^- + H^+$	$1.3 \times 10^{-2} \exp(1960 \times (1/T-1/298)) \, M$	Smith and Martell (1976)
$HSO_3^- \leftrightarrow SO_3^{2-} + H^+$	$6.6 \times 10^{-8} \exp(1500 \times (1/T-1/298)) \, M$	Smith and Martell (1976)
$H_2SO_4 \leftrightarrow HSO_4^- + H^+$	$1000 \, M$ (at 298K)	Perrin (1982)
$HSO_4^- \leftrightarrow SO_4^{2-} + H^+$	$1.02 \times 10^{-2} \exp(2720 \times (1/T-1/298)) \, M$	Smith and Martell (1976)
$H_2O_2 \leftrightarrow HO_2^- + H^+$	$2.2 \times 10^{-12} \exp(-3730 \times (1/T-1/298)) \, M$	Smith and Martell (1976)
$HNO_3 \leftrightarrow NO_3^- + H^+$	$15.4 \exp(8700 \times (1/T-1/298)) \, M$	Schwartz (1984)
$HONO \leftrightarrow NO_2^- + H^+$	$5.1 \times 10^{-4} \exp(-1260 \times (1/T-1/298)) \, M$	Schwartz and White (1981)
$CO_2H_2O \leftrightarrow HCO_3^- + H^+$	$4.3 \times 10^{-7} \exp(-1000 \times (1/T-1/298)) \, M$	Smith and Martell (1976)
$HCO_3^- \leftrightarrow CO_3^{2-} + H^+$	$4.68 \times 10^{-11} \exp(-1760 \times (1/T-1/298)) \, M$	Smith and Martell (1976)
$HCl \leftrightarrow H^+ + Cl^-$	$1.74 \times 10^6 \exp(6900 \times (1/T-1/298)) \, M$	Marsh and McElroy (1985)
$HO_2 \leftrightarrow H^+ + O_2^-$	$3.5 \times 10^{-5} \, M$	Perrin (1982)
$Br_2Cl^- \leftrightarrow Br_2 + Cl^-$	$1.3 \, M$	Wang et al. (1994)
$HBr \leftrightarrow H^+ + Br^-$	$1. \times 10^9 \, M$ (at 298K)	Lax (1969)
$NH_4^+ \leftrightarrow NH_3 + H^+$	$5.88 \times 10^{-10} \, M$	Chameides (1984)

Table 3.4 Aqueous reactions.

Aqueous reactions	Rate constant	References
$Hg + OH \rightarrow \cdot HgOH$	$2.4 \times 10^9 \, M^{-1}s^{-1}$	Gårdfeldt et al. (2001)
$HgOH + O_2 + H_2O \rightarrow Hg(OH)_2 + H^+ + O_2^-$	$10^9 \, M^{-1}s^{-1}$	Gårdfeldt et al. (2001)
$Hg + OH \rightarrow Hg^+ + OH^-$	$2.0 \times 10^9 \, M^{-1}s^{-1}$	Lin and Pehkonen (1997)
$HgO + H^+ \rightarrow Hg^{2+} + OH^-$	$1 \times 10^{10} \, M^{-1}s^{-1}$	Pleijel and Munthe (1995)
$HOCl + Hg \rightarrow Hg^{2+} + Cl^- + OH^-$	$2.09 \times 10^6 \, M^{-1}s^{-1}$	Lin and Pehkonen (1998)
$OCl^- + Hg (+H^+) \rightarrow Hg^{2+} + Cl^- + OH^-$	$1.99 \times 10^6 \, M^{-1}s^{-1}$	Lin and Pehkonen (1998)
$HgSO_3 \rightarrow Hg^0 + product$	$0.6 \, s^{-1}$	Pleijel and Munthe (1995)
$Hg(OH)_2 \rightarrow Hg^0 + product$	$3 \times 10^{-7} \, s^{-1}$	Pleijel and Munthe (1995)
$Hg^{2+} + HO_2 \rightarrow Hg^+ + O_2 + H^+$	$1.7 \times 10^4 \, M^{-1} \, s^{-1}$	Pehkonen and Lin (1998)
$Hg^+ + HO_2 \rightarrow Hg + O_2 + H^+$	$1 \times 10^{10} \, M^{-1} \, s^{-1}$	Xie et al. (2008)
$SO_3^{2-} + OH \, (+O_2) \rightarrow SO_5^- + OH^-$	$5.2 \times 10^9 \, M^{-1}s^{-1}$	Huie and Neta (1987)
$SO_3^{2-} + Cl_2^- \, (+O_2) \rightarrow SO_5^- + 2Cl^-$	$3.4 \times 10^8 \, M^{-1}s^{-1}$	Huie and Neta (1987)
$HSO_3^- + OH \, (+O_2) \rightarrow SO_5^- + H_2O$	$4.5 \times 10^9 \, M^{-1}s^{-1}$	Huie and Neta (1987)
$HSO_3^- + Cl_2^- \, (+O_2) \rightarrow SO_5^- + 2Cl^- + H^+$	$3.4 \times 10^8 \, M^{-1}s^{-1}$	Huie and Neta (1987)
$HSO_3^- + NO_3 \, (+O_2) \rightarrow SO_3^- + NO_3^- + H^+$	$1.0 \times 10^8 \, M^{-1}s^{-1}$	Chameides (1984)
$SO_5^- + O_2^- \, (+H_2O) \rightarrow HSO_5^- + O_2 + OH^-$	$1.0 \times 10^8 \, M^{-1}s^{-1}$	Jacob (1986)
$2 \, SO_5^- \rightarrow 2 \, SO_4^- + O_2$	$6.0 \times 10^8 \, M^{-1}s^{-1}$	Huie and Neta (1987)
$SO_4^- + HSO_3^- \, (+O_2) \rightarrow SO_4^{2-} + H^+ + SO_5^-$	$1.3 \times 10^9 \, M^{-1}s^{-1}$	Jacob (1986)
$SO_4^- + HO_2 \rightarrow SO_4^{2-} + H^+ + O_2$	$5.0 \times 10^9 \, M^{-1}s^{-1}$	Jacob (1986)
$SO_4^- + O_2^- \rightarrow SO_4^{2-} + O_2$	$5.0 \times 10^9 \, M^{-1}s^{-1}$	Jacob (1986)
$NO + OH \rightarrow NO_2^- + H^+$	$2.0 \times 10^{10} \, M^{-1}s^{-1}$	Strehlow and Wagner (1982)
$NO_2^- + OH \rightarrow NO_2 + OH^-$	$1.0 \times 10^{10} \, M^{-1}s^{-1}$	Treinin and Hayon (1970)
$NO_2^- + NO_3 \rightarrow NO_2 + NO_3^-$	$1.2 \times 10^9 \, M^{-1}s^{-1}$	Ross and Neta (1979)
$NO_3 + HO_2 \rightarrow NO_3^- + H^+ + O_2$	$4.5 \times 10^9 \, M^{-1}s^{-1}$	Jacob (1986)
$NO_3 + O_2^- \rightarrow NO_3^- + O_2$	$1.0 \times 10^9 \, M^{-1}s^{-1}$	Jacob (1986)
$CO_3^{2-} + OH \rightarrow OH^- + CO_3^-$	$3.9 \times 10^8 \, M^{-1}s^{-1}$	Buxton et al. (1988)
$CO_3^- + O_2^- \rightarrow CO_3^{2-} + O_2$	$6.5 \times 10^8 \, M^{-1}s^{-1}$	Eriksen et al. (1985)
$OH + HO_2 \rightarrow H_2O + O_2$	$1.0 \times 10^{10} \, M^{-1}s^{-1}$	Elliott and Buxton (1992)
$OH + O_2^- \rightarrow OH^- + O_2$	$1.0 \times 10^{10} \, M^{-1}s^{-1}$	Elliott and Buxton (1992)

$OH + OH^- \rightarrow H_2O + O^-$	$1.3 \times 10^{10} M^{-1}s^{-1}$	Buxton et al. (1988)
$O_2^- + O_3 \rightarrow O_2 + O_3^-$	$1.5 \times 10^9 M^{-1}s^{-1}$	Sehested et al. (1983)
$O_3^- + H^+ \rightarrow O_2 + OH$	$9.0 \times 10^{10} M^{-1}s^{-1}$	Neta et al. (1988)
$O^- + HO_2^- \rightarrow O_2^- + OH^-$	$4.0 \times 10^8 M^{-1}s^{-1}$	Buxton et al. (1988)
$HO_2^- + O_3 \rightarrow OH + O_2^- + O_2$	$5.5 \times 10^6 M^{-1}s^{-1}$	Neta et al. (1988)
$H + HO_2 \rightarrow H_2O_2$	$1.0 \times 10^{10} M^{-1}s^{-1}$	Buxton et al. (1988)
$H + O_2 \rightarrow HO_2$	$2.1 \times 10^{10} M^{-1}s^{-1}$	Buxton et al. (1988)
$H + O_3 \rightarrow OH + O_2$	$3.7 \times 10^{10} M^{-1}s^{-1}$	Neta et al. (1988)
$Cl^- + OH \rightarrow HOCl^-$	$4.3 \times 10^9 M^{-1}s^{-1}$	Jayson et al. (1973)
$HOCl^- \rightarrow Cl^- + OH$	$6.1 \times 10^9 M^{-1}s^{-1}$	Jayson et al. (1973)
$HOCl^- + H^+ \rightarrow H_2O + Cl$	$1.45 \times 10^{10} M^{-1}s^{-1}$	Neta et al. (1988)
$2Cl_2^- \rightarrow Cl_2 + 2Cl^-$	$2.0 \times 10^9 M^{-1}s^{-1}$	Neta et al. (1988)
$Cl_2^- + HO_2 \rightarrow 2Cl^- + O_2 + H^+$	$(1-4.5) \times 10^9 M^{-1}s^{-1}$	Neta et al. (1988)
$Cl_2^- + OH \rightarrow HOCl + Cl^-$	$1.0 \times 10^9 M^{-1}s^{-1}$	Wagner et al. (1986)
$Cl_2^- + H \rightarrow H^+ + 2Cl^-$	$7.0 \times 10^9 M^{-1}s^{-1}$	Buxton et al. (1988)
$Cl_2 + HO_2 \rightarrow H^+ + Cl_2^- + O_2$	$1.0 \times 10^9 M^{-1}s^{-1}$	Bjergbakke et al. (1981)
$Cl + Cl^- \rightarrow Cl_2^-$	$8.5 \times 10^9 M^{-1}s^{-1}$	Buxton et al. (1998)
$HOCl + SO_3^{2-} \rightarrow HSO_4^- + Cl^-$	$7.6 \times 10^8 M^{-1}s^{-1}$	Fogelman et al. (1989)
$Br + Br^- \rightarrow Br_2^-$	$1.6 \times 10^{10} M^{-1}s^{-1}$	Scaiano et al. (1992)
$HOBr + SO_3^{2-} (+ H_2O) \rightarrow SO_4^{2-} + Br^- + 2H^+$	$5 \times 10^9 M^{-1}s^{-1}$	Troy and Margerum, (1991)
$Br^- + OH \rightarrow HOBr^-$	$1.1 \times 10^{10} M^{-1}s^{-1}$	Kläning and Wolff (1985)
$HOBr^- + H^+ \rightarrow H_2O + Br$	$1.1 \times 10^{10} M^{-1}s^{-1}$	Kläning and Wolff (1985)
$2Br_2^- \rightarrow Br_2 + 2Br^-$	$2 \times 10^9 M^{-1}s^{-1}$	D'Angelantonio et al. (1988)

2.3. Box model simulations

We studied $Hg°$ loss from the gas phase associated with gas-aqueous mass transfer during the nighttime in summer at the TF site. For the study, we did not consider photo-dissociation chemical mechanisms from the gas phase reactions. Thus, radical reactions did not occur due to the lack of radical production by photo-dissociation. Several different measurement data sets were utilized to set the initial conditions of gas phase chemical compounds (Table 3.5). The majority of the data was provided by the AIRMAP program (NO, CH_3OH, CH_3Br, $Hg°$, CO, CO_2, SO_2, and hydrocarbons), and we obtained representative values (<0.5 km altitude) for initial conditions of OH, HO_2, CH_4, NO_2, H_2O_2, HCHO, H_2O, and CH_3CHO from the DC-8 measurements over the TF area during the 2004 ICARTT study. These mixing ratios were calculated to concentrations (cm^{-3}) at 294 K and 0.94 atm.

The process of preparing initial conditions utilizing TF data was as follows. We used the following criteria to select well-defined cases, and 15 nights out of 153 nights were selected. First, we considered the time period only from May – September, 2009, and excluded days with precipitation. In order to consider an isolated environment in the horizontal dimension, we obtained 10 minute averaged wind speed data at nighttime (20:00 – 06:00 EDT), and then selected the days where the mean value for 10 hours was <1 m/s. The last consideration was the presence of a well established nocturnal boundary layer during nighttime, which was identified by a nighttime decrease in O_3 and $Hg°$, and corresponding increase in CO_2 (Talbot et al., 2005). The median summertime mixing ratio was utilized as the initial conditions for NO, CH_3OH, CH_3Br, $Hg°$, CO, CO_2, and SO_2. The monthly mean values of hydrocarbons at TF were documented by Russo et al. (2010), and we utilized the average values during summertime for C_2H_6, C_3H_8, C_2H_2, and n-C_4H_{10}. Moreover, the initial conditions were 1 pptv for Cl_2, Br_2, and I_2 (Stutz et al., 2007).

Aerosol input is also an important feature for realistic model simulations. A couple of studies have shown that the dominant aerosol composition at TF is sulfate (Ziemba et al., 2007; Cottrell et al., 2008). The median values for the summertime were 41.3 nmol m^{-3} for NH_4^+ and 23.7 nmol m^{-3} for SO_4^{2-} (Ziemba et al., 2007), and we utilized these values for the initial conditions. Our group conducted an intensive study of PHg at Thompson Farm in summer 2009. Sampling with a cascade impactor showed the presence of sea salt, and the greatest amount of Hg was associated with it on coarse aerosols (Feddersen et al., 2010). In fact, the largest amount of Hg was found on aerosol with 3 μm aerodynamic diameter. For simplicity, we assumed all of the PHg was on 3

μm size aerosols. We did not consider the aerosol lifetime in the atmosphere due to the short simulation time (100 hours) compared to a typical aerosol lifetime of ~7 days (Hedgecock et al., 2004).

Table 3.5. Initial conditions for the simulation.

Chemical compounds	Mixing ratios
NO	50 pptv
NO_2	0 pptv
H_2O_2	2086 pptv
HCHO	2305 pptv
OH	0.11 pptv
CH_3OH	1620 pptv
CH_3CHO	480 pptv
C_2H_6	1085 pptv
C_2H_2	226 pptv
C_3H_8	522 pptv
$n-C_4H_{10}$	103 pptv
CH_4	1800 ppbv
HO_2	11.17 pptv
CH_3Br	8 pptv
O_3	39 ppbv
$Hg°$	138 ppqv
CO	150 ppbv
H_2O	16400 ppmv
CO_2	373 ppmv
SO_2	350 pptv

3. Results

3.1. The water solubility of Hg°

Henry's law constant of Hg° is 0.11 - 0.14 M atm^{-1} at 298K (Schroeder and Munthe, 1998; Sanemasa, 1975), and the constant has a much higher value compared to the constants of CO_2 (0.034 M atm^{-1}) and O_3 (0.01 M atm^{-1}). Gaseous elemental mercury is typically not thought of as a soluble compound, but its Henry's law constant indicates enough water solubility that it must be considered in chemical cycling of Hg°. We

converted the constant to dimensionless units for application in our chemical box model by multiplying by the temperature and gas constant (R: 82.05 (cm^3 atm K^{-1} mol^{-1})), producing values of 2.69 – 3.42. The constant indicates that Hg$_{(aq)}$ should be about a factor of 3 greater than Hg$^{\circ}$ in the gas phase.
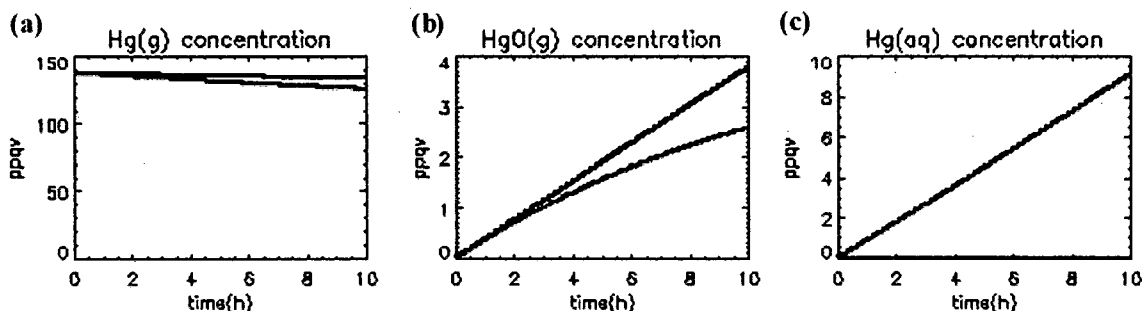
Figure 3.1. Results of Hg$^{\circ}$ (a), HgO$_{(g)}$ (b), and Hg$_{(aq)}$ (c) from a 10 hour simulation. Black line is without consideration of aerosol chemistry and blue line is with aerosol chemistry included.

We conducted simulations using sensitivity experiments with and without aerosol chemistry to check the impact of water solubility on Hg$^{\circ}$ in the gas phase (Figure 3.1). The liquid water content (LWC) was set to 2×10^{-12} (m^3(water)/m^3(air)) for the case considering aerosol chemistry (Dickerson et al., 1999). After 10 hours of simulation without aerosol chemistry the results showed that ~3.8 ppqv of Hg$^{\circ}$ was transformed to RGM, mostly HgO$_{(g)}$. In comparison, the simulation with aerosol chemistry indicated that ~11.5 ppqv of Hg$^{\circ}$ was transformed to RGM and PHg, mainly HgO$_{(g)}$ and Hg$_{(aq)}$. Moreover, Hg$_{(aq)}$ was increased to ~9 ppqv after 10 hours, and Hg$_{(aq)}$ was mainly converted by mass transport of Hg$^{\circ}$ between the gaseous and aqueous phases. Hence, about a factor of 2 greater amount of Hg$^{\circ}$ was converted to aerosol forms compared to

without aerosol present. Therefore, the slight water solubility of Hg° affects considerably the interconversion of mercury species.

3.2. Aerosol uptake as a function of liquid water content

The liquid water content (LWC) of aerosols is the most important factor controlling Hg° gaseous-aqueous mass transport. We conducted several sensitivity experiments to define the uptake as a function of LWC. Previous model studies utilized different LWC values for discrete aerosol types. For example, the LWC value of sea salt aerosol is commonly in the range of $3\times10^{-11} - 6\times10^{-11}$ (m^3(water)/m^3(air)), while the value for sulfate aerosol varied from $1.07\times10^{-12} - 2.14\times10^{-12}$ (Dickerson et al., 1999; Hedgecock, et al., 2004). Moreover, an upper limit of LWC was 2×10^{-11} for mixed ambient aerosol (Stanier et al., 2004).

The aerosol composition at TF showed that sulfate and organic matter are the dominant components (Ziemba et al., 2007; Cottrell et al., 2008). Thus, we assumed that the aerosol LWC was 2×10^{-12} for the lower limit. Moreover, LWC in the atmosphere could be increased at night because of aerosol uptake and also thermodynamic occurrence of dew or radiation fog. Therefore, we conducted five sensitivity experiments utilizing different aerosol LWCs covering the range of $2\times10^{-12} - 2\times10^{-10}$ (Figure 3.2).

The 10 hour simulation showed that the dominant RGM and PHg were $HgO_{(g)}$ and $Hg_{(aq)}$. More $HgO_{(g)}$ was produced with less LWC and more $Hg_{(aq)}$ was generated with higher LWC. $HgO_{(g)}$ was about a factor of 4 lower than $Hg_{(aq)}$ for the case of 2×10^{-12}, and $HgO_{(g)}$ was 4 orders of magnitudes lower than $Hg_{(aq)}$ in the case of 2×10^{-10}. We extended the simulation time to check when the equilibrium between Hg° and $Hg_{(aq)}$ was reached, and we assumed that the equilibrium between both states was reached at 46

ppqv Hg°, which was one third of the value of the initial condition. The time to reach equilibrium by different LWC was as follows; 2.6 hours for 2×10^{-10}, 8.6 hours for 6×10^{-11}, 24.9 hours for 2×10^{-11}, 72.9 hours for 6×10^{-12}. Moreover, the equilibrium was not reached for a 100 hour simulastion with a 2×10^{-12} LWC.
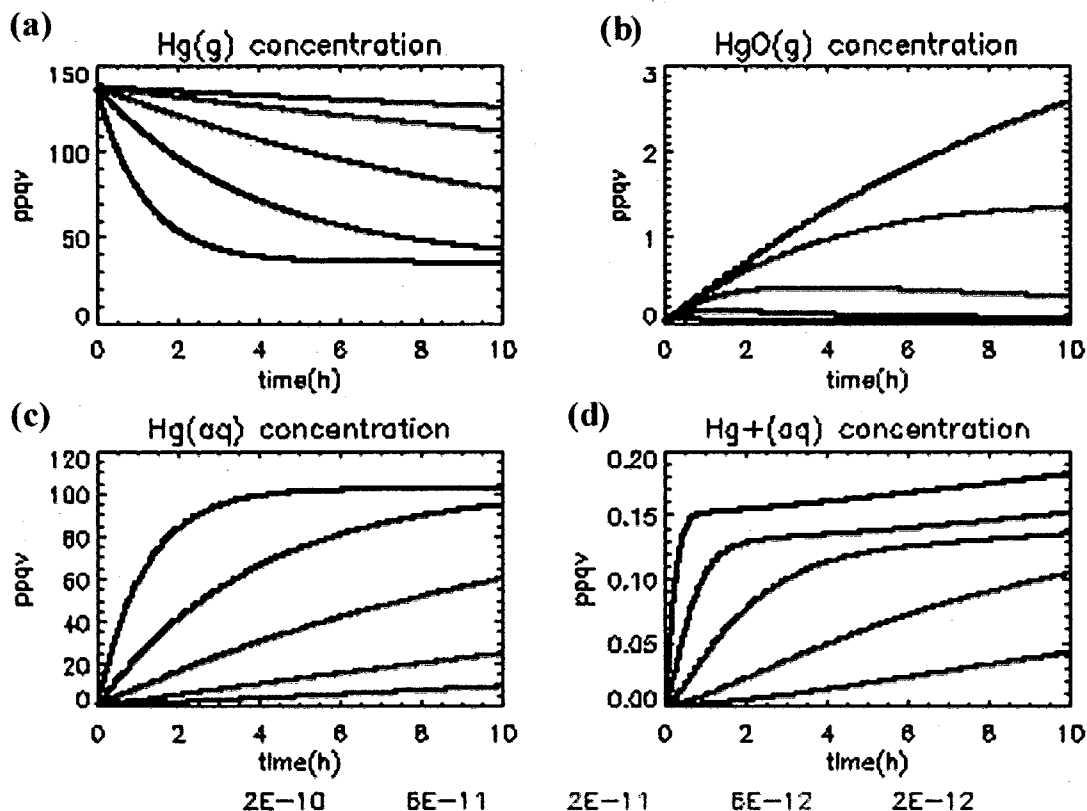
Figure 3.2. Results of Hg° (a), $HgO_{(g)}$ (b), $Hg_{(aq)}$ (c), $Hg^+_{(aq)}$ (d) for a 10 hour simulation with different LWC (unit: m^3(water)/m^3(air)). The lines represent as follows: black for 2×10^{-10}, blue for 6×10^{-11}, red for 2×10^{-11}, green for 6×10^{-12}, and purple for 2×10^{-12}

3.3 Results considering dry deposition

Previous ideal simulations (i.e. theoretical simulations) showed that the loss of Hg° transferred exactly to the amount of RGM and PHg formed by mass conservation due to omission of other atmospheric processes in the model. The dry deposition of Hg°

is an important factor determining the amout of speciated mercury in the atmosphere (Mao et al., 2008), and thus we added the dry deposition process into the chemical box model, which is formulated as $\frac{d[C]}{dt} = -\frac{v_d}{H}[C]$. Here, we utilized 125 m for the nocturnal inversion layer height (H) (Talbot et al., 2005), and a LWC of 2×10^{-11}. We simulated several sensitity experiments with different dry deposition velocities (v_d) for speciated mercury (Table 3.6) (Shon et al., 2005; Mao et al., 2008; Seinfeld and Pandis, 1998). S13 is the experiment without consideration of dry deposition for all three speicated mercury chemical forms; Hg°, PHg, and RGM.

Table 3.6. Sensitivity experiments with dry deposition added.

| | $v_d = 5$ cm s^{-1} | | | $v_d = 0.5$ cm s^{-1} | | | dry deposition of Hg° | |
	RGM	PHg	Both	RGM	PHg	Both	$v_d = 0.2$cm s^{-1}	$v_d = 0$ cm s^{-1}
S1	×						×	
S2	×							×
S3		×					×	
S4		×						×
S5			×				×	
S6			×					×
S7				×			×	
S8				×				×
S9					×		×	
S10					×			×
S11						×	×	
S12						×		×
S13								×

First, we examined the impact of v_d = 5 cm s^{-1} on speciated mercury without considering dry deposition of Hg° (S2, S4, and S6) (Shon et al., 2005) (Table 3.7. and Figure 3.3 (a)-(c)). The mixing ratio of Hg° was decreased by ~60 ppqv and it was decreased slightly more for S4 and S6 compared to S13 and S2 for a 10 hour simulation. The simulation showed that HgO$_{(g)}$, the dominant form of RGM, was of the order of 0.1

ppqv, and it was a factor of 2-3 less for S2 and S6 than S4 and S13. $Hg_{(aq)}$ value for the S13 and S2 was increased to 60 ppqv after 10 hours of simulation, while the value for the S4 and S6 cases was ~3 ppqv.

Table 3.7. Mixing ratios of speciated mercury after 10 hours of simulation.

		$Hg°$ (ppqv)	$HgO_{(g)}$ (ppqv)	$Hg_{(aq)}$ (ppqv)
No deposition (S13)		77	0.3	60
$v_d = 5$ cm s^{-1} without Hg° deposition	RGM (S2)	77	0.09	59
	PHg (S4)	72	0.3	3.4
	Both (S6)	72	0.08	3.3
$v_d = 5$ cm s^{-1} with Hg° deposition	RGM (S1)	44	0.05	45
	PHg (S3)	41	0.2	2.0
	Both (S5)	41	0.05	1.9
$v_d = 0.5$ cm s^{-1} without Hg° deposition	RGM (S8)	77	0.2	60
	PHg (S10)	75	0.3	30
	Both (S12)	75	0.2	30
$v_d = 0.5$ cm s^{-1} with Hg° deposition	RGM (S7)	44	0.2	42
	PHg (S9)	43	0.2	22
	Both (S11)	43	0.1	22

Second, we considered dry deposition of Hg° with $v_d = 5$ cm s^{-1} (Table 3.7. and Figure 3.3 (d)-(f)). The dry deposition velocity of Hg° (0.2 cm s^{-1}) was derived without consideration of aerosol uptake during summer nighttime at TF (Mao et al., 2008). Hg° was decreased ~32 ppqv more after 10 hours, and $HgO_{(g)}$ and $Hg_{(aq)}$ were increased slightly less for S1, S3, and S5 compared to S2, S4, and S6. Third, we utilized a dry deposition velocity of RGM and PHg = 0.5 cm s^{-1} based on the typical dry deposition velocity of a 3 μm diameter aerosol (Seinfeld and Pandis, 1998) (Table 3.7. and Figure 3.3. (g)-(l)). The loss amount of Hg° was similar to in the cases with $v_d = 5$ cm s^{-1}. Moreover, $HgO_{(g)}$ was increased more for cases S7, S8, S11, and S12 compared to S1, S2, S5, and S6. $Hg_{(aq)}$ was increased to ~20 ppqv for S9 and S11, and 30 ppqv for S10 and
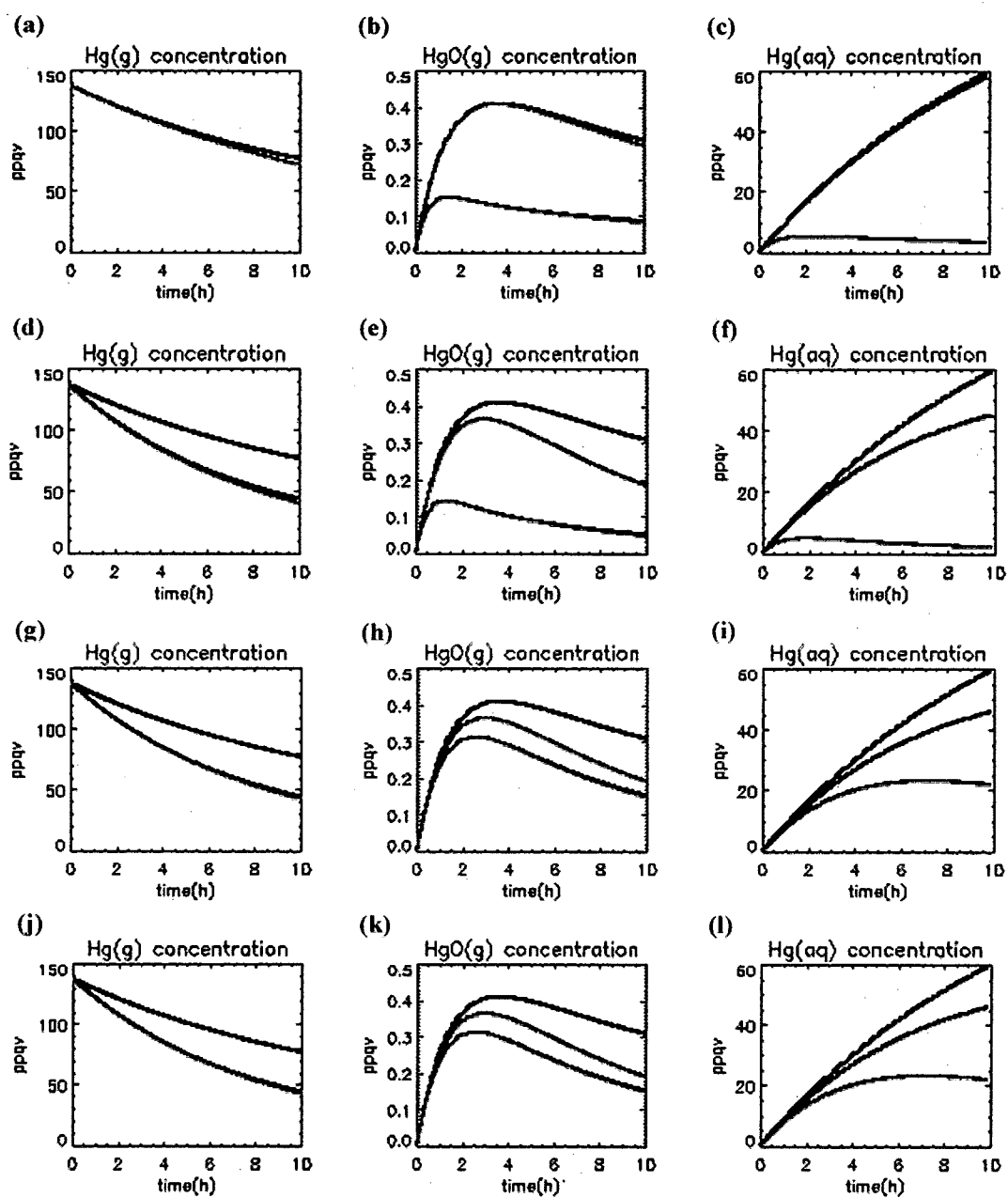
Figure 3.3. Results of 10 hour simulation for sensitivity experiments with changing values of the dry deposition velocity. The first column is Hg°, the second column is $HgO_{(g)}$, and the third column in $Hg_{(aq)}$. (a)–(c) for 5 cm s^{-1} of RGM or PHg without Hg° deposition, (d)-(f) for 5 cm s^{-1} of RGM or PHg with Hg° deposition, (g)-(i) for 0.5 cm s^{-1} of RGM or PHg without Hg° deposition, and (j)-(l) for 0.5 cm s^{-1} of RGM or PHg with Hg° deposition. The line colors are as follows; black line for no deposition of PHg or RGM, blue line for only deposition of RGM, red line for only deposition of PHg, and green line for deposition of RGM and PHg.

S12 after 10 hours. The mixing ratios were one order of magnitude greater than in the cases of S3, S4, S5, and S6.

The 10 hour simulations showed that the loss of Hg° was ~60 ppqv for mass transfer between the gaseous-aqueous phases and ~32 ppqv for dry deposition utilizing v_d = 0.2 cm s^{-1}. The amount of Hg° lost indicated that aerosol uptake into its liquid water could be very important to mercury cycling compared to loss by dry deposition of Hg° alone. The results of sensitivity experiments conducted with different dry deposition velocities for PHg suggested that dry deposition loss of PHg is an extremely important process controlling ambient levels of PHg.

4. Conclusions

We included mass transfer between gaseous-aqueous phases and mercury aqueous reactions into our gas phase mercury chemical box model in order to better understand loss of Hg° during the night. The mass transfer between the gaseous-aqueous phases was significantly influenced by water solubility of Hg° and the amount of LWC. The impact of water solubility of Hg° was examined through two sensitivity experiments; with and without aerosol chemistry. Ten hours of simulation showed that ~3.8 ppqv and ~11.5 ppqv of Hg° were depleted without and with aerosol chemistry respectively. The sensitivity experiments showed that Hg$_{(aq)}$ was increased to 9–102 ppqv with variable LWC ranging from 2×10^{-12}-2×10^{-10} after 10 hours of simulation.

Finally, we conducted sensitivity experiments with consideration of dry deposition of speciated mercury. The sensitivity experiments indicated that dry deposition of PHg is critical to generate typical ambient levels of PHg compared to Hg°

and RGM. The loss of Hg° by aerosol uptake and dry deposition suggested that aerosol uptake of Hg° could play an important role in mercury cycling in the atmosphere.

IV. Implications of my study

The first study of my Ph.D. work was long-range transport of pollutants. My study showed the importance of WCB and convection to long-range transport with fast westerly flow in upper troposphere. Climate change should influence these dynamical phenomena. For example, recent weather analysis in summer 2010 showed jet blocking, which is associated with climate change. It drove extremly hot weather in many global regions including Russia and northeastern Asia and terrible flooding in Pakistan and China. These stagnant meteorology patterns, presumably involved with climate change, should occur more frequently with associated intensive convection or WCBs transport. Therefore, it will be interesting to study long-range transport patterns of pollutants in the future with ongoing climate change.

The characteristics of mercury chemistries were studied in various environments; Arctic springtime and rural areas in the northeastern U.S. There are a few implications associated with my study. The first is related to my mercury study in Arctic springtime. Thinking about how climate change in the Arctic might affect MDEs produced the following possible scenarios. Climate change has driven a decreasing amount of ice surface area over the Arctic Ocean, and thus should promote increasing amounts of halogen compounds released into boundary layer air. This implies the possibility of more frequent and widespread occurrence of springtime MDEs. On the other hand, a larger open ocean would foster more turbulence in the atmosphere above, and perhaps cause reduced occurrence of pronounced MDEs. Since the ocean is a large natural source of Hg° (Andersson et al., 2008), this might also serve to reduce MDEs. It will be interesting

to observe in the future the impact of reduced Arctic pack ice on chemical cycling of trace gases like Hg° that are sensitive to such processes.

The second implication is related to the enrivonment in rural areas of the northeastern U.S. Uptake of Hg° in the water layer of aerosol within the nocturnal inversion layer should occur readily based on our model results. During nighttime the air within the inversion layer exhibits a relative humidity near 100%. At daybreak when the sun rises the inversion starts to dissipate as vertical mixing commences. As the air warms and begins to mix with drier air, the aerosol LWC should decrease releasing Hg° back into the gas phase. This diurnal cycling represents dynamic exchange of Hg° between the gas and aerosol phases. Therefore, I proposed that the diurnal cycle of Hg° was strongly influenced by uptake onto aerosols with high liquid water content at night and then re-volatilized back to the gas phase from the aerosol after sunrise.

LIST OF REFERENCES

Andersson, M. E., Sommar, J., Gårdfeldt, K., Lindqvist, O.: Enhanced concentrations of dissolved gaseous mercury in the surface waters of the Arctic Ocean, Mar. Chem., 110, 190-194, 2008.

Ariya, P. A., Khalizov, A., and Gidas, A.: Reactions of Gaseous Mercury with Atomic and Molecular Halogens : Kinetics, Product Studies, and Atmospheric Implications, J. Phys. Chem. A, 106, 7310-7320, 2002.

Ariya, P. A., Dastoor, A. P., Amyot, M., Schroeder, W. H., Barrie, L., Anlauf, K., Raofie, F., Ryzhkov, A., Davignon, D., Lalonde, J., and Steffen, A. : The Arctic : a sink for mercury, Tellus, 56B, 397-403, 2004.

Arnold, S. R., et al.: Statistical inference of OH concentrations and air mass dilution rates from successive observations of nonmethane hydrocarbons in single air masses, J. Geophys. Res., 112, D10S40, doi:10.1029/2006JD007594, 2007.

Atkinson, R., Baulch, D. L., Cox, R. A., Crowley, J. N., Hampson, R. F., Hynes, R. G., Jenkin, M. E., Rossi, M. J., and Troe, J. : Evaluated kinetic and photochemical data for atmospheric chemistry : Volume I – gas phase reactions of O_x, HO_x, NO_x, and SO_x species, Atmos. Chem. Phys., 4, 1461-1738, 2004.

Atkinson, R., Baulch, D. L., Cox, R. A., Crowley, J. N., Hampson, R. F., Hynes, R. G., Jenkin, M. E., Rossi, M. J., and Troe, J.: Evaluated kinetic and photochemical data for atmospheric chemistry : Volume II – gas phase reactions of organic species, Atmos. Chem. Phys., 6, 3625-4055, 2006.

Atkinson, R., Baulch, D. L., Cox, R. A., Crowley, J. N., Hampson, R. F., Hynes, R. G., Jenkin, M. E., Rossi, M. J., and Troe, J.: Evaluated kinetic and photochemical data for atmospheric chemistry: Volume III – gas phase reactions of inorganic halogens, Atmos. Chem. Phys., 7, 981-1191, 2007.

Aucott, M. L., McCulloch, A., Graedel, T. E., Kleiman, G., Midgley, P., and Li, Y.-F.: Anthropogenic emissions of trichloromethane (chloroform, $CHCl_3$) and chlorodifluoromethane (HCFC-22): Reactive Chlorine Emissions Inventory, J. Geophys. Res., 104(D7), 8405-8415, 1999.

Baker, A. K., Beyersdorf, A. J., Doezema, L. A., Katzenstein, A., Meinardi, S., Simpson, I. J., Blake, D. R., and Rowland, F. S.: Measurements of Nonmethane Hydrocarbons in 28 United States Cities, Atmos. Environ., 42, 170-182, 2008.

Balabanov, N. B., Shepler, B. C., and Peterson, K. A.: Accurate Global Potential Energy Surface and Reaction Dynamics for the Ground State of $HgBr_2$, J. Phys. Chem. A, 109, 8765-8773, 2005.

Barletta, B., Meinardi, S., Simpson, I. J., Rowland, F. S., Chan, C.-Y., Wang, X., Zou, S., Chan, L. Y., and Blake, D. R.: Ambient halocarbon mixing ratios in 45 Chinese cities, Atmos. Environ., 40, 7706-7719, 2006.

Bartlett, K. B., Sachse, G. W., Collins Jr., J.E., and Harriss, R. C.: Methane in the tropical South Atlantic: Sources and distribution during the late dry season, J. Geophys. Res., 101(D19), 24,139-24,150, 1996.

Bartlett, K. B., Sachse, G. W., Slate, T., Harward, C., and Blake, D. R.: Large-scale distribution of CH_4 in the western North Pacific: Sources and transport from the Asian continent, J. Geophys. Res., 108(D20), 8807, doi:10.1029/2002JD003076, 2003.

Bash, J. O., Miller, D. R., Meyer, T. H., and Bresnahan, P. A.: Northeast Unites States and Southeast Canada natural mercury emissions estimated with a surface emission model, Atmos. Environ., 38, 5683-5692, 2004.

Bjergbakke, E., Navartnam, S., Parsons, B. J., and Swallow, A. J.: Reaction between HO2·and chlorine in aqueous solution, J. Am. Chem. Soc., 103, 5926−5928, 1981.

Blake, N. J., Blake, D. R., Simpson, I. J., et al.: NMHCs and halocarbons in Asian continental outflow during the Transport and Chemical Evolution over the Pacific (TRACE-P) Field Campaign: Comparison with PEM-West B., J. Geophys. Res., 108(D20), 8806, doi:10.1029/2002JD003367, 2003.

Branfireun, B. A., Krabbenhoft, D. P., Hintelmann, H., Hunt, R. J., Hurley, J. P., and Rudd, J. W. M. : Speciation and transport of newly deposited mercury in a boreal forest wetland : A stable mercury isotope approach, Water Resour. Res., 41, W06016, doi :10.1029/2004WR003219, 2005.

Brasseur, G. P., Orlando, J. J., and Tyndall, G. S.: Atmospheric Chemistry and Global Change, 654pp., Oxford University Press, New York, 1999.

Brimblecombe, P. and Clegg, S. L.: Erratum, J. Atmos. Chem., 8, 95, 1989.

Brunke, E.-G., Labuschagne, C., and Slemr, F.: Gaseous Mercury Emissions from a Fire in the Cape Peninsula, South Africa, during January 2000, Geophys. Res. Lett., 28(8), 1483-1486, 2001.

Buxton, G. V., Greenstock, C. L., Helman, W. P., and Ross, A. B.: Critical review of rate constants for reactions of hydrated electrons, hydrogen atoms and hydroxyl radicals (·OH/·O −) in aqueous solution, J. Phys. Chem. Ref. Data, 17, 513−886, 1988.

Calvert, J. G., and Lindberg, S. E.: A modeling study of the mechanism of the halogen-ozone-mercury homogeneous reactions in the troposphere during the polar spring, Atmos. Environ., 37, 4467-4481, 2003.

Castro, L., Dommergue, A., Ferrari, C., and Maron, L. : A DFT study of the reactions of O_3 with $Hg°$ or Br^-, Atmos. Environ., 43, 5708-5711, 2009.

Chameides, W. L.: The photochemistry of a remote marine stratiform cloud, J. Geophys. Res., 89D, 4739−4755, 1984.

Chan, L.-Y., Chu, K.-W., Zou, S.-C., Chan, C.-Y., Wang, X.-M., Barletta, B., Blake, D. R., Guo, H., and Tsai, W.-Y.: Characteristics of nonmethane hydrocarbons (NMHCs) in industrial, industrial-urban, and industrial-suburban atmospheres of the Pearl River Delta (PRD) region of south China, J. Geophys. Res., 111, D11304, doi:10.1029/2005JD006481, 2006.

Chin, M. and Davis, D. D.: Global sources and sinks of OCS and CS_2 and their distributions, Global Biogeochemical Cycles, 7(2), 321-337, 1993.

Clever, H.L., Johnson, S.A., and Derrick, M.E.: The solubility of mercury and some sparingly soluble mercury salts in water and aqueous electrolyte solutions. Journal of Physical Chemistry Reference Data 14 (3), 631−680, 1985.

Cobbett, F. D., Steffen, A., Lawson, G., and Van Heyst, B. J. : GEM fluxes and atmospheric mercury concentrations (GEM, RGM, and Hg^p) in the Canadian Arctic at Alert, Nunavut, Canada (February-June 2005), Atmos. Environ., 41, 6527-6543, 2007.

Colman, J. J., Swanson, A. L., Meinardi, S., Sive, B. C., Blake, D. R., and Rowland, F. S.: Description of the analysis of a wide range of volatile organic compounds in whole air samples collected during PEM-Tropics A and B, Anal. Chem., 73, 3723-3731, 2001.

Cooper, O. R., Moody, J. L., Parrish, D. D., Trainer, M., Ryerson, T. B., Holloway, J. S., Hübler, G., Fehsenfeld, F. C., Oltmans, S. J., and Evans, M. J.: Trace gas signatures of the airstreams within North Atlantic cyclones: Case studies from the North Atlantic Regional Experiment (NARE '97) aircraft intensive, J. Geophys. Res., 106(D6), 5437-5456, 2001.

Cooper, O. R., et al.: Large upper tropospheric ozone enhancements above midlatitude North America during summer: In situ evidence from the IONS and MOZAIC ozone measurement network, J. Geophys. Res., 111, D24S05, doi:10.1029/2006JD007306, 2006.

Cottrell, L. D., Griffin, R. J., Jimenez, J. L., Zhang, Q., Ulbrich, I., Ziemba, L. D., Beckman, P. J., Sive, B. C., and Talbot, R. W.: Submicron particles at Thompson

Farm during ICARTT measured using aerosol mass spectrometry, J. Geophys. Res., 113, D08212, doi:10.1029/2007JD009192, 2008.

Crawford, J., Olson, J., Davis D., et al.: Clouds and trace gas distributions during TRACE-P, J. Geophys. Res., 108(D21), 8818, doi:10.1029/2002JD003177, 2003.

D'Angelantonio, M., Ventury, M., and Mulazzani, Q. G: A re-examination of the decay kinetics of pulse radiolytically generated Br_2^- radicals in aqueous solution, Int. J. Radiat. Applic. Instr., 32, 319-324, 1988.

DeBell, L. J., Vozzella, M., Talbot, R. W., and Dibb, J. E.: Asian dust storm events of spring 2001 and associated pollutants observed in New England by the Atmospheric Investigation, Regional Modeling, Analysis and Prediction (AIRMAP) monitoring network, J. Geophys. Res., 109, D01304, doi:10.1029/2003JD003733, 2004.

Dibb, J. E., Talbot, R. W., Scheuer, E. M., Seid, G., Avery, M. A., and Singh, H. B.: Aerosol chemical composition in Asian continental outflow during the TRACE-P campaign: Comparison with PEM-West B, J. Geophys. Res., 108, 8815, doi:10.1029/2002JD003111, 2003.

Dickerson, R. R., Doddridge, B. G., Kelley, P., and Rhoads, K. P.: Large-scale pollution of the atmosphere over the remote Atlantic Ocean: Evidence from Bermuda, J. Geophys. Res., 100(D5), 8945-8952, 1995.

Dickerson, R. R., Rhoads, K. P., Carsey, T. P., Oltmans, S. J., Burrows, J. P., and Crutzen, P. J.: Ozone in the remote marine boundary layer: A possible role for halogens, J. Geophys. Res., 104, 21385-21395, 1999.

Donohoue, D. L., Bauer, D., and Hynes, A. J.: Temperature and Pressure Dependant Rate Coefficients for the Reaction of Hg with Cl and the Reaction of Cl with Cl : A Pulsed Laser Photolysis-Pulsed Laser Induced Fluorescence Study, J. Phys. Chem. A, 109(34), 7732-7741, doi :10.1021/jp0513541, 2005.

Donohoue, D. L., Bauer, D., Cossairt, B., and Hynes, A. J.: Temperature and Pressure Dependant Rate Coefficients for the Reaction of Hg with Br and the Reaction of Br with Br : A Pulsed Laser Photolysis-Pulsed Laser Induced Fluorescence Study, J. Phys. Chem. A, 110(21), 6623-6632, doi :10.1021/jp054688j, 2006.

Elliot, A.J. and Buxton, G.V.: Temperature dependence of the reactions $OH+O_2^-$ and $OH+HO_2$ in water up to 200°C. J. Chem. Soc. Faraday Trans. 88 (17), 2465–2470, 1992.

Eneroth, K., Holmén, K., Berg, T., Schmidbauer, N., and Solberg, S. : Springtime depletion of tropospheric ozone, gaseous elemental mercury and non-methane

hydrocarbons in the European Arctic, and its relation to atmospheric transport, Atmos. Environ., 41, 8511-8526, 2007.

Eriksen, T. E., Lind, J., and Merenyi, G.: On the acid-base equilibrium of the carbonate radical, Radiat. Phys. Chem., 26, 197-199, 1985.

Fain, X., Ferrari, C. P., Gauchard, P.-A., Magand, O., and Boutron, C. : Fast depletion of gaseous elemental mercury in the Kongsvegen Glacier snowpack in Svalbard, Geophys. Res. Lett., 33, L06826, doi :10.1029/2005GL025223, 2006.

Feddersen, D., Talbot, R., Mao, H., Smith, M., Sive, B.: Size distribution of atmospheric mercury in marine and continental atmospheres, Atmosphere, 2010, in preparation.

Fehsenfeld, F. C., Ancellet, G., Bates, T. S., et al.: International Consortium for Atmospheric Research on Transport and Transformation (ICARTT): North America to Europe – Overview of the 2004 summer field study, J. Geophys. Res., 111, D23S01, doi:10.1029/2006JD007829, 2006.

Finlayson-Pitts, B. J., and Pitts, J. N. Jr.: Chemistry of the upper and lower atmosphere, Academic Press, 969 pp., 2000.

Fiore, A. M., Horowitz, L. W., Purves, D. W., Levy II, H., Evans, M. J., Wang, Y., Li, Q., and Yantosca, R. M.: Evaluating the contribution of changes in isoprene emissions to surface ozone trends over the eastern United States, J. Geophys. Res., 110, D12303, doi:10.1029/2004JD005485, 2005.

Fogelman, K. D., Walker, D. M., and Margerum, D. W.: Non-metal redox kinetics: Hypochlorite and hypochlorous acid reactions with sulfite, Inorg. Chem., 28, 986–993, 1989.

Fuelberg, H., Loring, Jr., R., Watson, M., Sinha, M., Pickering, K., Thompson, A., Sachse, G., Blake, D., and Schoeber, M.: TRACE-A trajectory intercomparison 2. Isentropic and kinematic methods, J. Geophys. Res., 101, 23927–23939, 1996.

Fuelberg, H. E., Hannan, J. R., van Velthoven, P. F. J., Browell, E. V., Bieberbach Jr., G., Knabb, R. D., Gregory, G. L., Pickering, K. E., and Selkirk, H. B.: A meteorological overview of the Subsonic Assessment Ozone and Nitrogen Oxide Experiment (SONEX) period, J. Geophys. Res., 105(D3), 3633-3651, 2000.

Gårdfeldt, K., Sommar, J., Strömberg, D., and Feng, X: Oxidataion of atomic mercury by hydroxyl radicals and photoinduced decomposition of methymercury in the aqueous phase, Atmos. Environ., 35, 3039-3047, 2001.

Glodek, A. and Pacyna, J. M.: Mercury emission from coal-fired power plants in Poland, Atmos. Environ., 43, 5668-5673, 2009.

Goodsite, M. E., Plane, J. M. C., and Skov, H. : A Theoretical Study of the Oxidation of Hg^0 to $HgBr_2$ in the Troposphere, Environ. Sci. Technol., 38, 1772-1776, 2004.

Hall, B., Lindqvist, O., and Ljungström, E.: Mercury Chemistry in Simulated Flue Gases Related to Waste Incineration Conditions, Environ. Sci. Technol., 24, 108-111, 1990.

Hall, B.: The Gas Phase Oxidation of Elemental Mercury by Ozone, Water, Air, and Soil Poll., 80, 301-315, 1995.

Harriss, R. C., Sachse, G. W., Collins Jr., J. E., Wade, L., Bartlett, K. B., Talbot, R. W., Browell, E. V., Barrie, L. A., Hill, G. F., and Burney, L. G.: Carbon monoxide and methane over Canada: July-August 1990, J. Geophys. Res., 99(D1), 1659-1669, 1994.

Hedgecock, I. M., and Pirrone, N.: Chasing quicksilver: modeling the atmospheric lifetime of $Hg^°_{(g)}$ in the marine boundary layer at various latitudes, Environ. Sci. Technol., 38, 69-76, 2004.

Hedgecock, I. M., Trunfio, G. A., Pirrone, N., and Sprovieri, F. : Mercury chemistry in the MBL : Mediterranean case and sensitivity studies using the AMCOTS (Atmospheric Mercury Chemistry over the Sea) model, Atmos. Environ., 39, 7217-7230, 2005.

Holmes, C. D., Jacob, D. J., Mason, R. P., and Jaffe, D. A.: Sources and deposition of reactive gaseous mercury in the marine atmosphere, Atmos. Environ., 43, 2278-2285, 2009.

Holmes, C. D., Jacob, D. J., Corbitt, E. S., Mao, J., Yang, X., Talbot, R., Slemr, F., and Han, Y.-J.: Global atmospheric model for mercury including oxidation by bromine atoms, Atmos.Chem. Phys., in preparation, 2010.

Holton, J. R.: An introduction to dynamic meteorology, 511pp., Academic Press, San Diego, 1992.

Huie, R. E. and Neta, P.: Rate constants for some oxidations of S(IV) by radicals in aqueous solutions, Atmos. Environ., 21, 1743−1747, 1987.

Huntrieser, H., Heland, J., Schlager, H., et al.: Intercontinental air pollution transport from North America to Europe: Experimental evidence from airborne measurements and surface observations, J. Geophys. Res., 110, D01305, doi:10.1029/2004JD005045, 2005.

Jacob, D. J.: Chemistry of OH in remote clouds and its role in the production of formic acid and peroxymonosulfate, J. Geophys. Res., 91D, 9807−9826, 1986.

Jacob, D. J., Crawford, J. H., Maring, H., Clarke, A. D., Dibb, J. E., Emmons, L. K., Ferrare, R. A., Hostetler, C. A., Russell, P. B., Singh, H. B., Thompson, A. M., Shaw, G. E., McCauley, E., Pederson, J. R., and Fisher, J. A.: The arctic research of the composition of the troposphere from aircraft and satellites (ARCTAS) mission: design, execution, and first results, Atmos. Chem. Phys., 10, 5191-5212, 2010.

Jaffe, D., Anderson, T., Covert, D., Kotchenruther, R., Trost, B., Danielson, J., Simpson, W., Berntsen, T., Karlsdottir, S., Blake, D., Harris, J., Carmichael, G., and Uno, I.: Transport of Asian Air Pollution to North America, Geophys. Res. Lett., 26(6), 711-714, 1999.

Jaffe, D., McKendry, I., Anderson, T., and Price, H.: Six 'new' episodes of trans-Pacific transport of air pollutants, Atmos. Environ., 37, 391– 404, 2003.

Jayson, G. G., Parsons, B. J., and Swallow, A. J.: Some simple, highly reactive, inorganic chlorine derivatives in aqueous solution, J. Chem. Soc. Faraday Trans. 1, 69, 1597–1607, 1973.

Khalizov, A. F., Viswanathan, B., Larregaray, P., and Ariya, P. A. : A Theoretical Study on the Reactions of Hg with Halogens : Atmospheric Implications, J. Phys. Chem. A, 107, 6360-6365, 2003.

Kiley, C. M., Fuelbert, H. E.: An examination of summertime cyclone transport processes during Intercontinental Chemical Transport Experiment (INTEX-A), J. Geophys. Res., 111, D24S06, doi:10.1029/2006JD007115, 2006.

Kim, S. Y., Talbot, R. Mao, H., Blake, D. R., Huey, G., and Weinheimer, A. J.: Chemical transformations of $Hg°$ during Arctic mercury depletion events sampled from the NASA DC-8, Atmos. Chem. Phys. Diss., 10, 10077-10112, 2010.

Kläning, U. K., and Wolff, T.: Laser flash photolysis of HClO, ClO^-, HBrO, and BrO^- in aqueous solution. Reactions of Cl^- and Br^- atoms, Ber. Bunsenges. Phys. Chem., 89, 243-245, 1985.

Laurier, F. J. G., Mason, R. P., Whalin, L., and Kato, S.: Reactive gaseous mercury formation in the North Pacific Ocean's marine boundary layer: A potential role of halogen chemistry, J. Geophys. Res., 108(D17), 4529, doi:10.1029/2003JD003625, 2003.

Lax, E.: Taschenbuch für Chemiker und Physiker, Springer Verlag, Berlin, 1969.

Lehrer, E., Hönninger, G., and Platt, U. : A one dimensional model study of the mechanism of halogen liberation and vertical transport in the polar troposphere, Atmos. Chem. Phys., 4, 2427-2440, 2004.

Lewis, A. C., et al.: Chemical composition observed over the mid-Atlantic and the detection of pollution signatures far from source regions, J. Geophys., Res, 112, D10S39, doi:10.1029/2006JD007584, 2007.

Li, Q., Jacob, D. J., Park, R., Wang, Y., Heald, C. L., Hudman, R., Yantosca, R. M., Martin, R. V., and Evans, M.: North American pollution outflow and the trapping of convectively lifted pollution by upper-level anticyclone, J. Geophys. Res., 110, D10301, doi:10.1029/2004JD005039, 2005.

Liang, Q., Jaeglé, L., Hudman, R. C., et al.: Summertime influence of Asian pollution in the free troposphere over North America, J. Geophys. Res., 112, D12S11, doi:10.1029/2006JD007919, 2007.

Lin, C.-J., and Pehkonen, S. O.: Aqueous free radical chemistry of mercury in the presence of iron oxides and ambient aerosol, Atmos. Environ., 31, 4125-4137, 1997.

Lin, C.-J., and Pehkonen, S. O.: Oxidation of elemental mercury by aqueous chlorine (HOCl/OCl⁻) : Implications for troposperic mercury chemistry, J. Geophys. Res., 103, 28093-28102, 1998.

Lin, C.-J., and Pehkonen, S. O.: The chemistry of atmospheric mercury : a review, Atmos. Environ., 33, 2067-2079, 1999.

Lindberg, S. E., Brooks, S., Lin, C.-J., Scott, K. J., Landis, M. S., Stevens, R. K., Goodsite, M., and Richter, A.: Dynamic Oxidation of Gaseous Mercury in the Arctic Troposphere at Polar Sunrise, Environ. Sci. Technol., 36, 1245–1256, 2002.

Lindqvist, O. and Rhode, H.: Atmospheric mercury – a review, Tellus, 37B, 136-157, 1985.

Lu, J. Y., Schroeder, W. H., Barrie, L. A., Steffen, A., Welch, H. E., Martin, K., Lockhart, L., Hunt, R. V., Boila, G., and Richter, A. : Magnification of atmospheric mercury deposition to polar regions in springtime : the link to tropospheric ozone depletion chemistry, Geophys. Res., Lett., 28(17), 3219-3222, 2001.

Lyman, S. N. and Gustin, M. S.: Speciation of atmospheric mercury at two sites in northern Nevada, USA, Atmos. Environ., 42, 927-939, 2008.

Magarelli, G., and Fostire, A. H. : Influence of deforestation on the mercury air/soil exchange in the Negro River Basin, Amazon, Atmos. Environ., 39, 7518-7528, 2005.

Mak, J. E. and Southon, J. R.: Assessment of tropical OH seasonality using atmospheric ^{14}CO measurements from Barbados, Geophys. Res. Lett., 25(D15), 2801-2804, 1998.

Malcolm, E. G., Keeler, G. J., and Landis, M. S.: The effects of the coastal environment on the atmospheric mercury cycle, J. Geophys. Res., 108(D12), 4357, doi:10.1029/2002JD003084, 2003.

Mao, H., Talbot, R., Troop, D., Johnson, R., Businger, S., and Thompson, A. M.: Smart Balloon observations over the North Atlantic: O_3 data analysis and modeling, J. Geophys. Res., 111, D23S56, doi:10.1029/2005JD006507, 2006.

Mao, H., Talbot, R. W., Sigler, J. M., Sive, B. C., and Hegarty, J. D.: Seasonal and diurnal variations of Hg° over New England, Atmos. Chem. Phys., 8, 1403-1421, 2008.

Mao, H., Talbot, R., Sive, B., Kim, S. Y., Blake, D. R., and Weinheimer, A. J., Arctic mercury depletion and its quantitative link with halogens, J. Atmos. Chem., submitted, 2010a.

Mao, H., Talbot, R., et al. Long-term variation in speciated mercury at marine, coastal and inland sites in New England. Atmosphere, in preparation, 2010b.

Marsh, A. R. W. and McElroy, W. J.: The dissociation constant and Henry's law constant of HCl in aqueous solution, Atmos. Environ., 19, 1075–1080, 1985.

Martin, B. D., Fuelberg, H. E., Blake, N. J., Crawford, J. H., Logan, J. A., Blake, D. R., and Sachse, G. W.: Long range transport of Asian outflow to the equatorial Pacific, J. Geophys. Res., 108(D2), 8322, doi:10.1029/2001JD001418, 2003.

McKeen, S. A. and Liu, S. C.: Hydrocarbon ratios and photochemical history of air masses, Geophys. Res. Lett., 20(21), 2363-2366, 1993.

McKendry, I. G., Strawbridge, K. B., O'Neill, N. T., Macdonald, A. M., Liu, P. S. K., Leaitch, W. R., Anlauf, K. G., Jaegle, L., Fairlie, T. D., and Westphal, D. L.: Trans-Pacific transport of Saharan dust to western North America: A case study, J. Geophys. Res., 112, D01103, doi:10.1029/2006JD007129, 2007.

Methven, J., et al.: Establishing Lagrangian connections between observations within air masses crossing the Atlantic during the International Consortium for Atmospheric Research on Transport and Transformation experiment, J. Geophys. Res., 111, D23S62, doi:10.1029/2006JD007540, 2006.

Millet, D. B., Goldstein, A. H., Holzinger, R., et al.: Chemical characteristics of North American surface layer outflow: Insights from Chebogue Point, Nova Scotia, J. Geophys. Res., 111, D23S53, doi:10.1029/2006JD007287, 2006.

Montzka, S. A., Calvert, P., Hall, B. D., Elkins, J. W., Conway, T. J., Tans, P. P., and Sweeney, C.: On the global distribution, seasonality, and budget of atmospheric

carbonyl sulfide (COS) and some similarities to CO_2, J. Geophys. Res., 112, D09302, doi:10.1029/2006JD007665, 2007.

Na, K., Kim, Y. P., Moon, K.-C., Moon, I., and Fung, K.: Concentrations of volatile organic compounds in an industrial area of Korea, Atmos. Environ., 35, 2747-2756, 2001.

Neta, P., Huie, R., E., and Ross, A. B.: Rate constants for reactions of inorganic radicals in aqueous solution, J. Phys. Chem. Ref. Data, 17, 1027-1284, 1988.

Neuman, J. A., Nowak, J. B., Huey, L. G., Burkholder, J. B., Dibb, J. E., Holloway, J. S., Liao, J., Peischl, J., Roberts, J. M., Ryerson, T. B., Scheuer, E., Stark, H., Stickel, R. E., Tanner, D. J., and Weinheimer, A.: Bromine measurements in ozone depleted air over the Arctic Ocean, Atmos. Chem. Phys. Discuss., 10, 3827–3860, 2010.

Pal, B., and Ariya, P. A.: Gas-Phase HO·-Initiated Reactions of Elemental Mercury: Kinetics, Product Studies, and Atmospheric Implications, Environ. Sci. Technol., 38, 5555-5566, 2004a.

Pal. B., and Ariya, P. A.: Studies of ozone initiated reactions of gaseous mercury: kinetics, product studies, and atmospheric implications, Phys. Chem. Chem. Phys., 6, 572-579, 2004b.

Pan, L., and Carmichael, G. R.: A Two-Phase Box Model to Study Mercury Atmospheric Mechanism, Environ. Chem., 2, 205-214, doi:10.1071/EN05026, 2005.

Pan, L., Carmichael, G. L., Adhikary, B., Tang, Y., Streets,D., Woo, J.-H., Friedli, H. R., and Radke, L. F.: A regional analysis of the fate and transport of mercury in East Asia and an assessment of major uncertainties, Atmos. Environ., 42, 1144-1159, 2008.

Parrish, D. D., Holloway, J. S., Trainer, M., Murphy, P. C., Forbes, G. L., and Fehsenfeld, F. C.: Export of North American Ozone Pollution to the North Atlantic Ocean, Science, 259(5100), 1436-1439, 1993.

Parrish, D. D., Dunlea, E. J., Atlas, E. L., et al: Changes in the photochemical environment of the temperate North Pacific troposphere in response to increased Asian emissions, J. Geophys. Res., 109, D23S18, doi10.1029/2004JD004978, 2004.

Pehkonen, S. O. and Lin, C.-J.: Aqueous photochemistry of mercury with organic acids, J. Air Waste Manag. Assoc., 48, 144-150, 1998.

Perrin, D. D.: Ionization constants of inorganic acids and bases in aqueous solution, second edition, Pregamon Press, Inc., Elmsford, NY, 1982.

Petersen, G., Munthe, J., Pleijel, K., Bloxam, R., and Vinod Kumar, A.: A comprehensive eulerian modeling framework for airborne mercury species: development and testing of the tropospheric chemisty module (TCM), Atmos. Environ., 32, 829-843, 1998.

Pickering, K. E., Thompson, A. M., Wang, Y., Tao, W.-K., McNamara, D. P., Kirchhoff, V. W. J. H., Heikes, B. G., Sachse, G. W., Bradshaw, J. D., Gregory, G. L., and Blake, D. R.: Convective transport of biomass burning emissions over Brazil during TRACE A, J. Geophys. Res., 101(D19), 23,993-24,012, 1996.

Pirrone, N., Hedgecock, I. M., and Forlano, L.: Role of the ambient aerosol in the atmospheric processing of semivolatile contaminants: A parameterized numerical model (Gas-Particle Partitioning (GASPAR)), J. Geophy. Res., 105(D8), 9773-9790, 2000.

Pleijel, K., and Munthe, J.: Modelling the atmospheric mercury cycle-chemistry in fog droplets, Atmos. Environ., 29, 1441-1457, 1995.

Poissant, L., Pilote, M., Beauvais, C., Constant, P., and Zhang, H. H.: A year of continuous measurements of three atmospheric mercury species (GEM, RGM, and Hg$_p$) in southern Québec, Canada, Atmos. Environ., 39, 1275-1287, 2005.

Purvis, R. M., et al.: Rapid uplift of nonmethane hydrocarbons in a cold front over central Europe, J. Geophys. Res., 108(D7), 4224, doi:10.1029/2002JD002521, 2003.

Pyle, D. M. and Mather, T. A. Mather: The importance of volcanic emissions for the global atmospheric mercury cycle, Atmos. Environ., 37, 5115-5124, 2003.

Radke, L. F., Friedli, H. R., and Heikes, B. G.: Atmospheric mercury over the NE Pacific during spring 2002: Gradients, residence time, upper troposphere lower stratosphere loss, and long-range transport, J. Geophys. Res., 112, D19305, doi:10.1029/2005JD005828, 2007.

Raofie, F. and Ariya, P. A.: Kinetics and products study of the reaction of BrO radicals with gaseous mercury, J. Phys. IV France, 107, 1119–1121, 2003.

Reeves, C. E., et al.: Alkyl nitrates in outflow from North America over the North Atlantic during Intercontinental Transport of Ozone and Precursors 2004, J. Geophys. Res., 112, D10S27, doi:10.1029/2006JD007567, 2007.

Ridley, B. A., Grahek, F. E., and Walega, J. G.: A small high-sensitivity, medium-response ozone detector suitable for measurements from light aircraft, J. Atmos. Oceanic Technol., 9, 142-148, 1992.

Ross, A. B., and Neta, P.: Rate constants for reactions of inorganic radicals in aqueous solution, Natl. Stand. Ref. Data Ser., Natl. Bur. Stand., Report, No. 65, 1979.

Russo, R. S., Zhou, Y., White, M. L., Mao, H., Talbot, R., and Sive, B. C.: Multi-year (2004-2008) record of nonmethane hydrocarbons and halocarbons in New England: seasonal variations and regional sources, Atmos. Chem. Phys. Discuss., 10, 1083-1134, 2010.

Saiz-Lopez, A., Saunders, R. W., Joseph, D. M., Ashworth, S. H., and Plane, J. M. C.: Absolute absorption cross-section and photolysis rate of I_2, Atmos. Chem. Phys., 4, 1443-1450, 2004.

Sakata, M. and Asakura, K.: Estimating contribution of precipitation scavenging of atmospheric particulate mercury to mercury wet deposition in Japan, Atmos. Environ., 41, 1669-1680, 2007.

Sander, S. P., Finlayson-Pitts, B. J., Friedl, R. R., Golden, D. M., Huie, R. E., Kolb, C. E., Kurylo, M. J., Molina, M. J., Moortgat, G. K., Orkin, V. L., and Ravishankara, A. R.: Chemical Kinetics and Photochemical Data for Use in Atmospheric Studies, Evaluation Number 14, JPL Publication 02-25, Jet Propulsion Laboratory, Pasadena, CA., 2003.

Sander, S. P., Finlayson-Pitts, B. J., Friedl, R. R., Golden, D. M., Huie, R. E., Kolb, C. E., Kurylo, M. J., Molina, M. J., Moortgat, G. K., Wine, P. H., Keller-Rudek, H., Orkin, V. L., and Ravishankara, A. R.: Chemical Kinetics and Photochemical Data for Use in Atmospheric Studies, Evaluation Number 15, JPL Publication 06-2, Jet Propulsion Laboratory, Pasadena, CA, 2006.

Sandoval-Soto, L., Stanimirov, M., von Hobe, M., Schmitt, V., Valdes, J., Wild, A., and Kesselmeier, J.: Global uptake of carbonyl sulfide (COS) by terrestrial vegetation: Estimates corrected by deposition velocities normalized to the uptake of carbon dioxide (CO_2), Biogeosciences, 2, 125-132, 2005.

Sandu, A., and Sander, R.: Technical note: Simulating chemical systems in Fortran90 and Metlab with the Kinetic PreProcessor KPP-2.1, Atmos. Chem. Phys., 6, 187-195, 2006.

Sanemasa, I.: The solubility of elemental mercury vapor in water, B. Chem. Soc. Jpn., 48, 1795-1798, 1975.

Scaiano, J. C., Barra, M., Calabrese, G., and Sinta, R.: Photochemistry of 1,2-dibromoethane in solution. A model for the generation of hydrogen bromide, J. Chem. Soc., Chem. Commun., 1418, 1992.

Scheuer, E., Talbot, R. W., Dibb, J. E., Seid, G. K., DeBell, L., and Lefer, B.: Seasonal distributions of fine aerosol sulfate in the North American Arctic basin during TOPSE, J. Geophys. Res., 108, 8370, doi:10.1029/2001JD001364, 2003.

Schroeder, W. H. and Munthe, J.: Atmospheric Mercury-An Overview, Atmos. Environ., 32, 809-822, 1998.

Schroeder, W. H., Anlauf, K. G., Barrie, L. A., Lu, J. Y., Steffen, A., Schneeberger, D. R., and Berg, T. : Arctic springtime depletion of mercury, Nature, 394, 331-332, 1998.

Schwartz, S. E. and White, W. H.: Solubility equilibria of the nitrogen oxides and oxyacids in dilute aqueous solution, in: Advances in Environmental Science and Engineering, edited by Pfafflin, J. R. and Ziegler, E. N., vol. 4, pp. 1−45, Gordon and Breach Science Publishers, NY, 1981.

Schwartz S. E.: Gas-aqueous reactions of sulfur and nitrogen oxides in liquid water clouds. In *Acid Precipitations Series* (edited by Teasley J. I.), Vol. 3, Chapter 4, pp. 173-208. Butterworth Publisliers, Ann Arbor, 1984.

Schwartz, S. E.: Mass transport considerations pertinent to aqueous phase reactions of gases in liquid-water clouds, Chemistry of Multiphase Atmospheric Systems, NATO ASI Series, Vol. G6, Springer-Verlag Berlin Heidelberg, 415-471, 1986.

Sehested, K., Holcman, J., and Hart, E. J.: Rate constants and products of the reactions of e^-aq, O^-2 and H with ozone in aqueous solutions, J. Phys. Chem., 87, 1951−1954, 1983.

Seinfeld, J. H. and Pandis, S. N.: Atmospheric Chemistry and Physics – From Air Pollution to Climate Change, John Wiley & Sons, New York, USA, 1998.

Shon, Z.-H., Kim, K.-H., Kim, M.-Y., and Lee, M.: Modeling study of reactive gaseous mercury in the urban air, Atmos. Environ., 39, 749-761, 2005.

Sigler, J. M. and Lee, X.: Recent trends in anthropogenic mercury emission in the northeast United States, J. Geophys,. Res., 111, D14316, doi:10.1029/2005JD006814, 2006.

Sigler, J. M., Mao, H., and Talbot, R.: Gaseous elemental and reactive mercury in Southern New Hampshire, Atmos. Chem. Phys., 9, 1928-1942, 2009.

Simmonds, P. G., Manning, A. J., Cunnold, D. M., et al. : Global trends, seasonal cycles, and European emissions of dichloromethane, trichloroethene, and tetrachloroethene from the AGAGE observations at Mace Head, Ireland, and Cape Grim, Tasmania, J. Geophys. Res., 111, D18304, doi:10.1029/2006JD007082, 2006.

Simpson, W. R., von Glasow, R., Riedel, K., Anderson, P., Ariya, P., Bottenheim, J., Burrows, J., Carpenter, L. J., Frieβ, U., Goodsite, M. E., Heard, D., Hutterli, M., Jacobi, H.-W., Kaleschke. L., Neff, B., Plane, J., Platt, U., Richter, A., Roscoe, H., Sander, R., Shepson, P., Sodeau, J., Steffen, A., Wagner, T., and Wolff, E.:

Halogens and their role in polar boundary-layer ozone depletion, Atmos. Chem. Phys., 7, 4375-4418, 2007.

Singh, H. B., Brune, W. H., Crawford, J. H., Jacob, D. J., and Russell, P. B.: Overview of the summer 2004 Intercontinental Chemical Transport Experiment – North America (INTEX-A), J. Geophys. Res., 111, D24S01, doi:10.1029/2006JD007905, 2006.

Sive, B. C., Zhou, Y., Troop, D., Wang, Y., Little, W. C., Wingenter, O. W., Russo, R. S., Varner, R. K., and Talbot, R.: Development of a cryogen-free concentration system for measurements of volatile organic compounds, Anal. Chem., *77*(21), 6989-6998, 10.1021/ac0506231, 2005.

Smith, R.M. and Martell, A.E.: Critical stability constants Inorganic Complexes, vol. 4, Plenum, New York, 1976.

Smith, R.M. and Martell, A.E.: NIST critically selected stability constants of metal complexes database/data collected and selected by R. M. Smith and A. E. Martell; program developed by R. J. Motekaitis, NIST. Gaithersburg, MD, USA., 2004.

Snow, J. A., Heikes, B. G., Shen, H., O'Sullivan, D. W., Fried, A., and Walega, J.: Hydrogen peroxide, methyl hydroperoxide, and formaldehyde over North America and the North Atlantic, J. Geophys. Res., 112, D12S07, doi:10.1029/2006JD007746, 2007.

Sommar, J., Gårdfeldt, K., Strömberg, D., and Feng, X., A kinetic study of the gas-phase reaction between the hydroxyl radical and atomic mercury, Atmos. Environ., 35, 3049-3054, 2001.

Stanier, C. O., Khlystov, A. Y., Chan, W. R., Mandiro, M., and Pandis, S. N.: A method for the in situ measurement of fine aerosol water content of ambient aerosol: the dry-ambient aerosol size spectrometer (DAASS), Aerosol Sci. Tech., 38(S1), 215-228, 2004.

Stohl, A., Forster, C., Eckhardt, S., Spichtinger, N., Huntrieser, H., Heland, J., Schlager, H., Wilhelm, S., Arnold, F., and Cooper, O.: A backward modeling study of intercontinental pollution transport using aircraft measurements, J. Geophys. Res., 108(D12), 4370, doi:10.1029/2002JD002862, 2003.

Strehlow, H. and Wagner, I.: Flash photolysis in aqueous nitrite solutions. Z. Phys. Chem., 132, 151-160, 1982.

Strode, S. A., Jaeglé, L., Selin, N. E., Jacob, D. J., Park, R. J., Yantosca, R. M., Mason, R. P., and Slemr, F.: Air-sea exchange in the global mercury cycle, Global Biogeochem. Cycles, 21, GB1017, doi:10.1029/2006GB002766, 2007.

Stutz, J., Pikelnaya, O., Hurlock, S. C., Trick, S., Pechtl, S., and von Glasow, R.: Daytime OIO in the Gulf of Maine, Geophys. Res. Lett., 34, L22816, doi:10.1029/2007GL031332, 2007.

Swartzendruber, P. C., Jaffe, D. A., Prestbo, E. M., Weiss-Penzias, P., Selin, N. E., Park, R., Jacob, D. J., Strode, S., and Jaeglé, L.: Observations of reactive gaseous mercury in the free troposphere at the Mount Bachelor Observatory, J. Geophys. Res., 111, D24301, doi:10.1029/2006JD007415, 2006.

Talbot, R. W., Dibb, J. E., Klemm, K. I., Bradshaw, J. D., Sandholm, S. T., Blake, D. R., Sachse, G. W., Collins, J., Heikes, B. G., Gregory, G. L., Anderson, B. E., Singh, H. B., Thornton, D. C., and Merrill, J. T.: Chemical characteristics of continental outflow from Asia to the troposphere over the western Pacific Ocean during September-October 1991: Results from PEM-West A, J. Geophys. Res., 101(D1), 1713-1725 1996a.

Talbot, R. W., Bradshaw, J. D., Sandholm, S. T., Smyth, S., Blake, D. R., Blake, N. R., Sachse, G. W., Collins, J. E., Heikes, B. G., Anderson, B. E., Gregory, G. L., Singh, H. B., Lefer, B. L., and Bachmeier, A. S.: Chemical characteristics of continental outflow over the tropical South Atlantic Ocean from Brazil and Africa, J. Geophys. Res., 101(D19), 24,187-24,202, 1996b.

Talbot, R. W., Dibb, J. E., Lefer, B. L., Bradshaw, J. D., Sandholm, S. T., Blake, D. R., Blake, N. J., Sachse, G. W., Collins Jr., J. E., Heikes, B. G., Merrill, J. T., Gregory, G. L., Anderson, B. E., Singh, H. B., Thornton, D. C., Bandy, A. R., and Pueschel, R. F.: Chemical characteristics of continental outflow from Asia to the troposphere over the western Pacific Ocean during February – March 1994: Results from PEM-West B, J. Geophys. Res., 102(D23), 28,255-28,274, 1997.

Talbot, R., Mao, H., and Sive, B.: Diurnal characteristics of surface level O_3 and other important trace gases in New England, J. Geophys. Res., 110, D09307, doi:10.1029/2004JD005449, 2005.

Talbot, R., Mao, H., Scheuer, E., Dibb, J., Avery, M., Browell, E., Sachse, G., Vay, S., Blake, D., Huey, G., and Fuelberg, H.: Factors influencing the large-scale distribution of Hg° in the Mexico City area and over the north Pacific, Atmos. Chem. Phys., 8, 2103-2114, 2008.

Talbot, R., Mao, H., Feddersen, D, Smith, M., Kim, S.Y., Sive, B., Ambrose, J., Zhou, Y., and Russo, R., Assessment of particulate mercury measured with the Tekran system, Atmosphere, submitted, 2010.

Tokos, J. J. S., Hall, B., Calhoun, J. A., and Prestbo, E. M.: Homogeneous gas-phase reaction of Hg° with H_2O_2, O_3, CH_3I, and $(CH_3)_2S$: implications for atmospheric Hg cycling, Atmos. Environ., 32, 823-827, 1998.

Treinin, A. and Hayon, E.: Absorption spectra and reaction kinetics of NO_2, N_2O_3, and N_2O_4 in aqueous solution, J. Am. Chem. Soc., 92, 5821-5828, 1970.

Troy, R. C. and Margerum, D. W.: Non-metal redox kinetics: Hypobromite and hypobromous acid reactions with iodide and with sulfite and the hydrolysis of bromosulfate, Inorg. Chem., 30, 3538−3543, 1991.

Twohy, C. H., Clement, C. F., Gandrud, B. W., et al.: Deep convection as a source of new particles in the midlatitude upper troposphere. J. Geophys. Res., 107(D21), 4560, doi:10.1029/2001JD000323, 2002.

U.S. EPA, NADP, and Tekran. Standard Operating Procedures for Analysis of Gaseous and Fine Particulate-Bound Mercury, 2009, 74 pp.

Van Loon, L.L., Mader, E.A., Scott, S.L.: Sulfite stabilization and reduction of the aqueous mercuric ion: kinetic determination of sequential formation constants, Journal of Physical Chemistry A 105, 3190−3195, 2001.

Vay, S. A., Anderson, B. E., Conway, T. J., Sachse, G. W., Collins Jr., J. E., Blake, D. R., and Westberg, D. J.: Airborne observations of the tropospheric CO_2 distribution and its controlling factors over the South Pacific Basin, J. Geophys. Res., 104(D5), 5663−5676, 1999.

Verwer, J., Spee, E., Blom, J. G., and Hunsdorfer, W.: A second order Rosenbrock method applied to photochemical dispersion problems, SIAM Journal on Scientific Computing, 20, 1456-1480, 1999.

Wagner, I., Karthäuser, J., and Strehlow, H.: On the decay of the dichloride anion Cl2- in aqueous solution, Ber. Bunsenges. Phys. Chem., 90, 861-867, 1986.

Wang, T. X., Kelley, M. D., Cooper, J. N., Beckwith, R. C., and Margerum, D. W.: Equilibrium, kinetic, and UV-spectral characteristics of aqueous bromine chloride, bromine, and chlorine species, Inorg. Chem., 33, 5872−5878, 1994.

Wang, C. J.-L., Blake, D. R., and Rowland, F. S.: Seasonal variations in the atmospheric distribution of a reactive chlorine compound, tetrachloroethene (CCl_2=CCl_2), Geophys. Res. Lett., 22(9), 1097-1100, 1995 .

Wang, Y., Liu, S. C., Anderson, B. E., Kondo, Y., Gregory, G. L., Sachse, G. W., Vay, S. A., Blake, D. R., Singh, H. B., and Thompson, A. M.: Evidence of convection as a major source of condensation nuclei in the northern midlatitude upper troposphere, Geophys. Res. Lett., 27(3), 369-372, 2000.

Wilson, S. J., Steenhuisen, F., Pachna, J. M., and Pacyna, E. G.: Mapping the spatial distribution of global anthropogenic mercury atmospheric emission inventories, Atmos. Environ., 40, 4621-4632, 2006.

Won, J. H., Park, J. Y., and Lee, T. G.: Mercury emissions from automobiles using gasoline, diesel, and LPG, Atmos. Environ., 41, 7547-7552, 2007.

Xiao, Z.F., Munthe, J., Stromberg, D., Lindqvist, O.: Photochemical behavior of inorganic mercury compounds in aqueous solution. In: Watras, C.J., Huckabee, J.W. (Eds.), Mercuryas a Global Pollutant-toward Integration and Synthesis. Lewis Publishers, London, pp. 581−592, 1994.

Xiao, Y., Jacob, D. J., Wang, J. S., Logan, J. A., Palmer, P. I., Suntharalingam, P., Yantosca, R. M., Sachse, G. W., Blake, D. R., and Streets, D. G.: Constraints on Asian and European sources of methane from CH_4-C_2H_6-CO correlations in Asian outflow, J. Geophys. Res., 109, D15S16, doi:10.1029/2003JD004475, 2004.

Xie, Z.-Q., Sander, R., Pöschl, U., and Slemr, F.: Simulation of atmospheric mercury depletion events (AMDEs) during polar springtime using the MECCA box model, Atmos. Chem. Phys., 8, 7165-7180, 2008.

Zhou, Y., Varner, R. K., Russo, R. S., Wingenter, O. W., Haase, K. B., Talbot, R. W., and Sive, B. C.: Coastal water source of short-lived halocarbons in New England, J. Geophys. Res., *110*, D21302, doi:10.1029/2004JD005603, 2005.

Ziemba, L. D., Fischer, E., Griffin, R. J., and Talbot, R. W.: Aerosol acidity in rural New England: Temporal trends and source region analysis, J. Geophys. Res., 112, D10S22, doi:10.1029/2006JD007605, 2007.